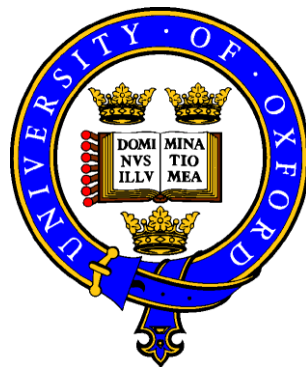


Neutron Scattering studies of Heavy Electron behaviour in $\text{YbNi}_2\text{B}_2\text{C}$

Julian P. Barratt
Exeter College



A thesis submitted for the degree of Doctor of Philosophy
at the University of Oxford

Clarendon Laboratory and the Institut Laue Langevin
Michaelmas Term, 2000

INTRODUCTION

Solid state physics is concerned with the study of the electrons and nuclei of materials in the solid phase. In its modern form, the subject began in 1897, with the discovery of the electron by J.J. Thomson. In 1911, Rutherford developed his theory of the atom in which negatively charged electrons orbit a dense positive nucleus. Two years later, Niels Bohr explained the electromagnetic stability of the atom by combining Rutherford's model with Max Planck's theory of quantisation [1]. In 1912, a paper was presented to the Bavarian Academy of Sciences in Munich. This paper contained a general theory of diffraction, formulated by Max von Laue, and the first experimental observation of the diffraction of X-rays by a periodic lattice of atoms by Friedrich and Knipping. In 1913, W.L. Bragg published a simpler explanation of the diffracted beams from crystalline materials [2] and proceeded to perform the first structure determinations [3]. The majority of the progress in solid state physics has been made investigating crystalline materials, although recently considerable attention has been paid to more disordered materials [4] [5] [6].

A complete description of the behaviour of the electrons and nuclei in a material would involve the inclusion of all the electrostatic, magnetic and quantum mechanical exchange interactions between all the constituent elements. Although the relative magnitudes of these interactions varies, enabling some to be neglected, the huge number of atoms present in a macroscopic sample makes such a calculation impossible. In order to proceed, mathematical techniques have been developed that reduce this complexity, such as replacing the individual effect of many particles with an average or using a phenomenological approach that neglects the details of the interactions completely. At first sight, these simplifications may seem rather drastic, but both the qualitative and quantitative predictions of the calculations are often strikingly accurate as is shown by the huge success of the electronics industry. Traditionally, the electrons in solid materials have been placed in one of two distinct categories: localised electrons which are constrained to move only around their respective nucleus, and itinerant electrons that are free to move throughout the whole material.

The interactions between the electrons in solid state materials are responsible for a wide range of interesting co-operative phenomena, such as superconductivity and long range magnetic order. Heavy fermion and valence fluctuation behaviour are other co-operative effects in which the traditional distinction between localised and itinerant electronic behaviour breaks down. In many compounds, different types of co-operative phenomena are displayed simultaneously and a large amount of research has been dedicated to understanding the interplay between them, particularly where one suppresses another.

The rare earth nickel borocarbides ($\text{RNi}_2\text{B}_2\text{C}$) are the subject of this thesis. In several of the compounds, [$\text{R} = \text{Dy}, \text{Ho}, \text{Er}$ and Tm], superconductivity and long range magnetic order coexist [7]. In $\text{YbNi}_2\text{B}_2\text{C}$, neither superconductivity nor long range magnetic order have been observed although it does exhibit heavy fermion behaviour [8]. The majority of this thesis is dedicated to the examination of the heavy fermion state in the ytterbium compound using the technique of neutron scattering and investigating its role in the suppression of the other types of correlated electron behaviour. The neutron scattering experiments in this thesis have been conducted at the Institut Laue Langevin (I.L.L.) in Grenoble, France, and at the ISIS facility of the Rutherford Appleton Laboratory in Didcot, U.K.

Chapter 1 begins with an outline of the history of the study of correlated electron behaviour in compounds containing rare earth ions. This is followed by a discussion of the known properties of the rare earth nickel borocarbide series.

In Chapter 2, the different types of rare earth correlated electron behaviour are discussed in detail. The chapter is divided into two parts. The first deals with the rare earth standard model that provides an accurate description of many rare earth compounds. The second part describes heavy fermion and valence fluctuation behaviour in compounds that have dilute and concentrated distributions of Kondo ions. In both parts, the interplay between long range magnetic order, heavy fermion or valence fluctuation behaviour and superconductivity is stressed.

The theory of neutron scattering is described in Chapter 3. The first part introduces the basic concepts and experimental procedures. This is followed by detailed descriptions of the specific experimental techniques used in this thesis.

Chapter 4 outlines the data analysis techniques used in this thesis. It describes how Bayesian probability theory provides a unifying mathematical framework for deriving the procedures of least squares refinement and maximum entropy image construction.

The experiments to determine the magnetisation density in $\text{YbNi}_2\text{B}_2^{11}\text{C}$, $\text{ErNi}_2\text{B}_2^{11}\text{C}$, $\text{HoNi}_2\text{B}_2^{11}\text{C}$ and $\text{LuNi}_2\text{B}_2^{11}\text{C}$ are described in Chapter 5. These experiments were performed on the D9 and D3 diffractometers at the I.L.L. This chapter also contains a description of an experiment performed using the D10 diffractometer at the I.L.L. that was designed to search for long range magnetic order in the $\text{YbNi}_2\text{B}_2^{11}\text{C}$ compound at low temperatures. An elastic scattering experiment using the D1B diffractometer at the I.L.L. is also included in this chapter. This experiment was used to determine the amount of Yb_2O_3 impurity present in the $\text{YbNi}_2\text{B}_2^{11}\text{C}$ polycrystalline sample that was used in some of the inelastic scattering experiments.

Chapter 6 contains the inelastic scattering experiments conducted on the $\text{YbNi}_2\text{B}_2^{11}\text{C}$ compound. Two experiments, performed using the H.E.T. spectrometer at ISIS and the IN20 spectrometer at the I.L.L., were designed to look for and study the Crystalline Electric Field (C.E.F.) transitions in the compound. Three experiments, performed using the IN5, IN14 and IN6 spectrometers at the I.L.L., were designed to study the low energy transfer scattering. The H.E.T. and IN5 experiments were performed on a polycrystalline sample of $\text{YbNi}_2\text{B}_2^{11}\text{C}$. The IN20, IN14 and IN6 experiments were performed on a single crystal mosaic sample.

The final chapter provides a summary of the main conclusions of the experiments. Suggestions for further work needed to obtain better images of the magnetisation density in the $\text{RNi}_2\text{B}_2^{11}\text{C}$ series and gain a clearer understanding of the excitation scheme of $\text{YbNi}_2\text{B}_2^{11}\text{C}$ are included in this chapter. A brief appendix gives the dates at which all the experiments, mentioned above, were performed.

References.

- [1] S. Gasiorowicz, *Quantum Physics*, Wiley (1974).
- [2] W.L. Bragg, *Cambridge Phil. Soc.*, **17**, 43 (1913).
- [3] W.L. Bragg, *Proc. R. Soc. A*, **89**, 248 (1914).
- [4] N.W. Ashcroft and N.D. Mermin, *Solid State Physics*, Holt-Saunders (1975).
- [5] C. Kittel, *Introduction to Solid State Physics*, Wiley (1976).
- [6] J.R. Hook and H.E. Hall, *Solid State Physics*, Wiley (1991).
- [7] R.J. Cava *et al.*, *Nature*, **367**, 252 (1994).
- [8] A. Yatskar *et al.*, *Phys. Rev. B*, **54**, 3772 (1996).

CHAPTER 1

THE RARE EARTH NICKEL BOROCARBIDES

This chapter begins with an outline of the history of the study of correlated electron behaviour in compounds containing rare earth ions. This is followed by a discussion of the known properties of the rare earth nickel borocarbide series.

1.1 A brief history of the study of the coexistence of superconductivity and magnetism.

In 1957, Bardeen, Cooper and Schrieffer published their famous microscopic theory of superconductivity [1]. The first investigation into the coexistence of superconductivity and magnetism was made shortly afterwards when Ginzburg predicted that the coexistence of long range ferromagnetic order and superconductivity was almost impossible [2]. In the following year, the first experimental studies were performed [3].

The history of this subject falls into several periods, each associated with the study of a different class of compounds. From 1958 until around 1975, experiments were performed on superconducting binary compounds containing small amounts of magnetic rare earth impurities. These experiments were largely inconclusive, as the magnetic order seen was often short range and difficult to characterise. However, the experiments provided a basis for a theoretical understanding of the effect of adding paramagnetic impurities into a superconducting matrix. The most important theory on this subject was provided by Abrikosov and Gor'kov [4].

From 1975 until around 1986, rare earth ternary compounds such as RRh_4B_4 , RMo_6S_8 and RMo_6Se_8 were studied. In these compounds, magnetic ordering of the rare earth electrons can coexist with superconductivity of the conduction electrons as exchange interactions between the two are weak. In most of the compounds studied,

superconductivity coexists with antiferromagnetic order. However, in a few compounds, superconductivity and ferromagnetic order coexist over a small temperature range close to the magnetic ordering temperature. If the temperature is lowered much below the ordering temperature, the superconductivity is destroyed. In the region where ferromagnetic order and superconductivity coexist, the interaction between the two leads to the formation of a sinusoidally modulated magnetic structure.

The high T_C cuprate superconductors were discovered by Bednorz and Müller in 1986 [5]. The parent compounds have formulas such as R_2CuO_4 and $RBa_2Cu_3O_7$, and display long range three dimensional antiferromagnetic order of the copper ions. As the oxygen content is reduced, in order to precipitate superconductivity, this magnetic order is suppressed. However, strong antiferromagnetic correlations between the copper ions still exist. Several theories postulate that fluctuations between the copper spins are responsible for the electron pairing in high T_C superconductors. The rare earth ions in these compounds enter a long range magnetically ordered state, but at temperatures typically two orders of magnitude lower than T_C .

In 1994, superconductivity coexisting with long range magnetic order was discovered in a new type of quaternary intermetallic compound, the rare earth nickel borocarbides (RNi_2B_2C) [6]. These compounds are the subject of this thesis and are described in detail in the following section.

A separate, but highly related, study began in 1930, with the discovery of a resistivity minima in metals containing dilute concentrations of magnetic ions. It was not until 1964 that Kondo provided an initial understanding of this phenomenon [7]. He described a ground state in which strong antiferromagnetic correlations exist between the magnetic moments of the impurity ions and the conduction electrons, substantially increasing the scattering of the conduction electrons at low temperatures. This effect gives rise to heavy fermion and valence fluctuation behaviour which is described in detail in § 2.2.

Some of the most important theories, mentioned above, concerning the coexistence of superconductivity and magnetism are outlined in § 2.1.4.

1.2 The properties of the rare earth nickel borocarbides.

Since the discovery of superconductivity in the rare earth nickel borocarbides they have attracted a great deal of attention. Superconductivity and long range magnetic order coexist in four of the compounds in the series, [R = Dy, Ho, Er and Tm]. However, unlike the ternary rare earth superconductors and the high T_C superconductors, mentioned above, the critical temperatures for the two types of order are the same order of magnitude [$T_N = 1.5$ K (Tm) to 10.6 K (Dy) and $T_C = 6$ K (Dy) to 11 K (Tm)]. This means that the interplay between superconductivity and magnetism is much stronger than in the two previous compound classes. The borocarbides containing rare earth atoms that are lighter than dysprosium (Dy) are not superconducting but RNi_2B_2C [R = Pr, Nd, Gd and Tb] display long range magnetic order [8]. $YbNi_2B_2C$ is anomalous in being neither superconducting nor magnetically ordered at any temperature investigated ($T \geq 0.3$ K) [9]. Its properties will be discussed in more detail below.

The borocarbides have a body centred tetragonal crystal structure, space group $I4/mmm$, and consist of alternating layers of rare earth / carbon and nickel / boron ions. The lattice parameters are approximately $a \sim b \sim 3.5$ Å and $c \sim 10.5$ Å across the whole series [8].

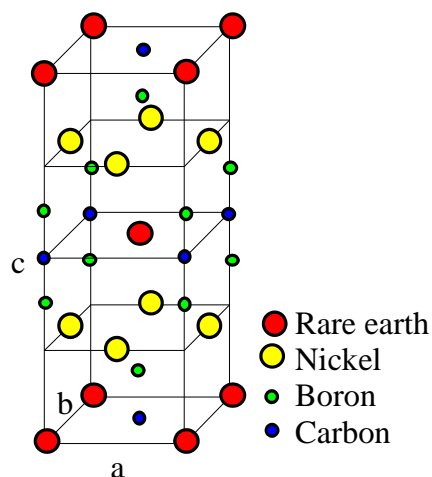


Fig 1.1 : Structure of the rare earth nickel borocarbides.

The superconducting transition temperatures in the heavy rare earth borocarbides are relatively high and there is still some debate over the pairing mechanism. The borocarbides were initially thought to be similar to the high T_C superconductors despite the three dimensional character of the superconductivity. There is some evidence from neutron scattering measurements that the nickel ion possess a small magnetic moment [10]. Some muon spin rotation experiments suggest that an exotic pairing mechanism such as fluctuations amongst the nickel magnetic moments may have a role in the borocarbide superconductivity [11]. However, the large isotope effect [12] and the behaviour of the lattice dynamics [13] strongly suggest that the borocarbides are conventional electron-phonon coupled superconductors. The high transition temperatures are thought to arise because of the high electronic density of states at the Fermi level, the strong electron-phonon coupling, and the high average phonon frequency seen in the superconducting state [14]. The high electronic density of states at the Fermi level was initially predicted from band structure calculations [15] and was later confirmed by experiment [16]. The position of the maximum in the density of states is a function of the ratio of the lattice parameters c/a . In the light rare earth borocarbides, this maximum is shifted away from the Fermi level as compared with the heavy rare earth compounds. This partially explains the lack of superconductivity in these compounds [17]. Evidence for the strong electron-phonon coupling comes from the heavy damping of phonons seen in inelastic neutron scattering experiments [18]. The strength of the coupling depends on the rare

earth atom present and it is larger for the heavy rare earth compounds. This is another factor in the removal of superconductivity in the light rare earth borocarbides [17].

The borocarbides display a wide variety of structures in the magnetically ordered state. The magnetic structures seen in the ternary rare earth superconductors are heavily influenced by the dipolar interaction between the rare earth ions [19]. In the borocarbides, the magnetic transition temperatures are too high for the dipolar interaction to be important. The magnetic structures are predominately determined by a competition between the indirect exchange interaction between the rare earth ions, the R.K.K.Y. interaction, and the crystalline electric field (C.E.F.) at each rare earth site. The R.K.K.Y. interaction usually favours the formation of a magnetically ordered structure that is incommensurate with the crystal lattice. This is because the wavevector associated with R.K.K.Y. ordering depends on the geometry of the Fermi surface, which may be entirely independent of the crystal periodicity (see § 2.1.2.2). The C.E.F. interaction breaks the directional degeneracy of the rare earth magnetic moment and introduces a preferred direction, the ‘easy’ axis, along which it is energetically favourable for the magnetic moment to align. As this effect is identical at each rare earth site, the C.E.F. interaction favours the formation of commensurate magnetic order (see § 2.1.2.1).

Below $T_N = 10.6$ K, the $\text{DyNi}_2\text{B}_2\text{C}$ compound has a commensurate antiferromagnetic structure. The moments in the a - b plane are ferromagnetically aligned with an easy axis of [110]. The structure is antiferromagnetically aligned along the c axis with wavevector $(0, 0, 1)$. The ordered moment has a magnitude of $8.47 \mu_B$ and superconductivity coexists with this structure below a temperature of $T_C = 6$ K [8].

The $\text{ErNi}_2\text{B}_2\text{C}$ compound is superconducting below $T_C = 11$ K and orders antiferromagnetically below $T_N = 6.8$ K. The structure is a transversely polarised spin density wave with a modulation wave vector of $(0.5526, 0, 0)$ or $(0, 0.5526, 0)$ with the moments pointing along the b or a axes respectively. As the temperature is lowered, higher order harmonics develop, indicating that the sinusoidal magnetic structure is squaring up. The magnitude of the low temperature magnetic moment is

$7.19 \mu_B$. A commensurate magnetic structure is not observed at low temperatures and superconductivity coexists with the magnetic order at all temperatures below T_N [10].

The $\text{HoNi}_2\text{B}_2\text{C}$ is the most interesting compound in which superconductivity and magnetism coexist. It becomes superconducting at a temperature of $T_C = 8$ K. At all temperatures below $T_N = 8.5$ K, the magnetic structure contains a component that is identical to that of $\text{DyNi}_2\text{B}_2\text{C}$. At the Neel temperature, another structure, in which the ferromagnetic sheets in adjacent layers along the c axis have a relative orientation of $\sim 163.4^\circ$ (instead of 180° seen in the commensurate structure) develops. These two magnetic structures grow in intensity at the same rate as the temperature is lowered. At a temperature of ~ 6.25 K, a third structure with a modulation wave vector of $(0.55, 0, 0)$ begins to develop. Just below the onset of the a axis modulation, at around 5 K, the superconductivity is suppressed, as is indicated by a minimum in the upper critical field H_C . On further cooling, both the incommensurate structures disappear and only the commensurate structure remains. This coincides with an increase in H_C . At low temperatures, the magnetic moment has a magnitude of $8.62 \mu_B$ [20].

The $\text{TmNi}_2\text{B}_2\text{C}$ compound becomes superconducting below $T_C = 11$ K and orders magnetically at $T_N = 1.5$ K. The structure is very different from those seen in the other borocarbides. The structure is a transversely polarised spin density wave with a modulation wave vector of $(0.093, 0.093, 0)$ and moments pointing along the c axis. As the temperature is lowered, higher order harmonics develop as the magnetic structure squares up. The low temperature magnetic moment is $3.78 \mu_B$. The magnetic ordering coexists with the superconductivity at all temperatures [21]. Lutetium does not possess a magnetic moment as it has a full $4f$ shell ($n = 14$). Therefore, the $\text{LuNi}_2\text{B}_2\text{C}$ compound shows no magnetic order. It is superconducting below $T_C = 17$ K [8].

The $\text{YbNi}_2\text{B}_2\text{C}$ compound is particularly interesting. De Gennes scaling predicts it will become superconducting below ~ 13 K, which is not observed experimentally, and no long range magnetic order has been observed to date. Substitutional studies with $\text{Yb}_x\text{Lu}_{1-x}\text{Ni}_2\text{B}_2\text{C}$ show that superconductivity is completely destroyed by

$x = 0.15$ [22]. The large linear contribution to the specific heat, with a Sommerfield coefficient of $\gamma \sim 530 \text{ mJ/mol K}^2$, classes $\text{YbNi}_2\text{B}_2\text{C}$ as a heavy fermion compound [9].

A broad peak in the specific heat (fig. 1.2) is seen at $\sim 8 \text{ K}$ which is often a characteristic of spin fluctuations in heavy fermion compounds. Crystal field calculations suggest that the $J = 7/2$ Yb^{+3} ground state multiplet, predicted by Hund's rules, should be split into four doublets. Above the peak, there are additional contributions to the specific heat, perhaps due to excitations between these crystal field split doublets.

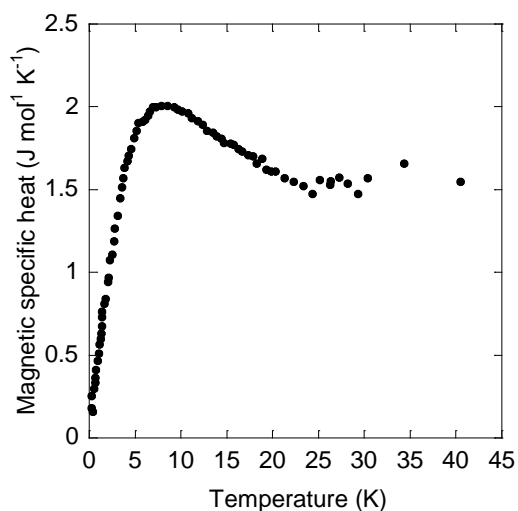


Fig 1.2 : Magnetic specific heat versus temperature for $\text{YbNi}_2\text{B}_2\text{C}$. This plot was obtained by subtracting the specific heat measured for $\text{LuNi}_2\text{B}_2\text{C}$ to remove the lattice contribution [23].

The static magnetic susceptibility (figs. 1.3 and 1.4) of $\text{YbNi}_2\text{B}_2\text{C}$ is larger when the applied field is aligned parallel to the c axis. This is similar to the $\text{TmNi}_2\text{B}_2\text{C}$ compound. The susceptibility measurements show Curie-Weiss behaviour above $\sim 125 \text{ K}$, with an effective magnetic moment that is similar to that predicted for the ground state of the ytterbium $+3$ ion. At temperatures below $\sim 125 \text{ K}$, the susceptibility deviates from this behaviour indicating that a paramagnetic local moment model is insufficient to describe the properties of this compound. However, at low temperatures, the susceptibility continues to rise as the temperature is lowered. This is in contrast to the 'typical' temperature independent Pauli-like behaviour of many other heavy fermion and valence fluctuation compounds (see § 2.2.3.2) and indicates that

the $4f$ electrons still possess a substantial localised character. Separate evidence for this is provided by X-ray absorption spectroscopy from which it was deduced that the Yb ions are still in a stable +3 ionisation state at low temperatures [9].

For other members of the borocarbide series, [R = Dy, Ho, Er and Tm], the susceptibility shows a Curie-Weiss temperature dependence above temperatures comparable with the antiferromagnetic ordering temperatures. The Weiss temperatures also agree with the Neel temperatures in these compounds.

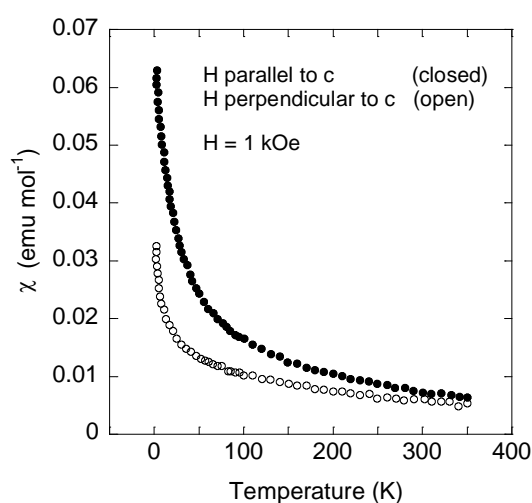


Fig 1.3 : Magnetic susceptibility, normalised per mole Yb, versus temperature for $\text{YbNi}_2\text{B}_2\text{C}$. Data shown for 1 kOe applied field parallel (closed) and perpendicular (open) to crystallographic c axis [23].

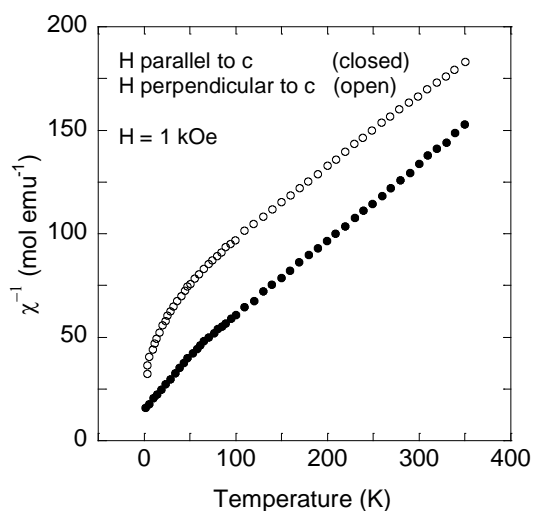


Fig 1.4 : Inverse magnetic susceptibility versus temperature for $\text{YbNi}_2\text{B}_2\text{C}$. Data shown for 1 kOe applied field parallel (closed) and perpendicular (open) to crystallographic c axis [23].

Measurements of the nuclear magnetic resonance of ^{11}B in $\text{YbNi}_2\text{B}_2\text{C}$ (fig. 1.5) also indicate a gradual crossover between local moment behaviour for $T > 50$ K, to itinerant correlated electron behaviour for $T < 5$ K.

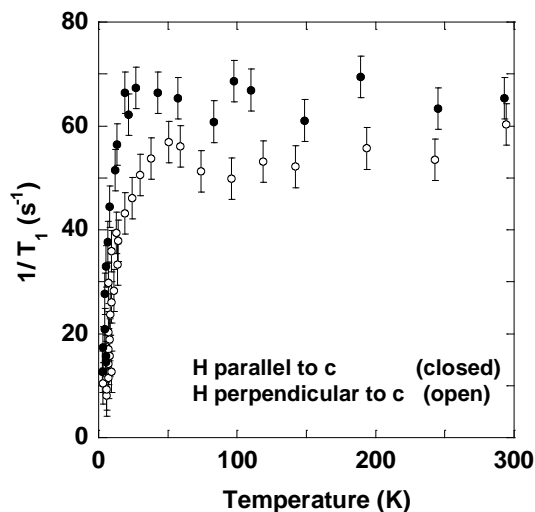


Fig 1.5 : Nuclear spin-lattice relaxation rate of ^{11}B in a single crystal of $\text{YbNi}_2\text{B}_2\text{C}$. Data shown for field parallel (closed) and perpendicular (open) to crystallographic c axis [24].

Above $T \sim 100$ K, the electrical resistivity (figs. 1.6 and 1.7) is approximately linear, and increases with temperature. Below this temperature, $d\rho/dT$ begins to increase with decreasing temperature. Below $T \sim 40$ K, the decrease in resistivity with decreasing temperature is substantially more rapid as compared with the high temperature behaviour. This rapid decrease in resistivity is often seen in concentrated heavy fermion compounds and is usually associated with the onset of coherence between individual Kondo scattering sites. In concentrated heavy fermion compounds, a peak is often seen in the resistivity, associated with a maximum in the Kondo scattering of the conduction electrons before the coherent state is entered (see § 2.2.4.1). However, such a peak is not seen in the resistivity of $\text{YbNi}_2\text{B}_2\text{C}$. At temperatures below $T \sim 1.5$ K, the resistivity displays a quadratic temperature dependence which is often associated with the formation of an enhanced Fermi-liquid ground state.

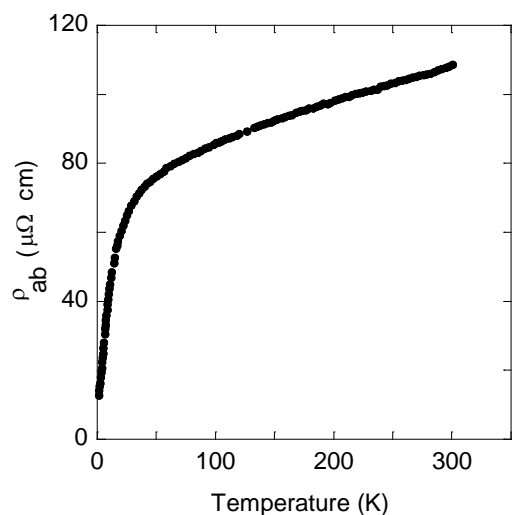


Fig 1.6 : Resistivity in the *a-b* plane versus temperature for $\text{YbNi}_2\text{B}_2\text{C}$ [23].

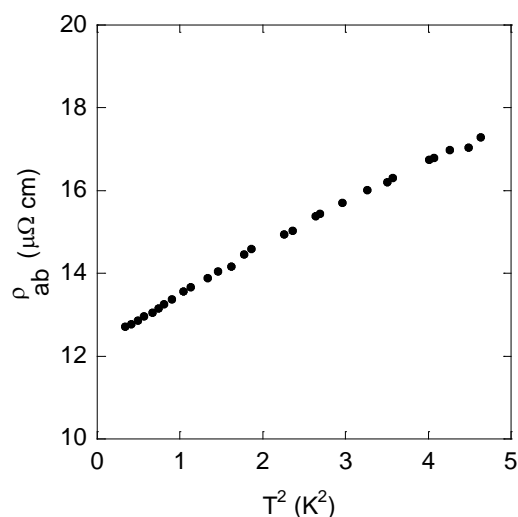


Fig 1.7 : Resistivity in the *a-b* plane versus the square of temperature at low temperatures for $\text{YbNi}_2\text{B}_2\text{C}$ [23].

References.

- [1] J. Bardeen, L.N. Cooper and J.R.Schrieffer, *Phys. Rev.*, **108**, 1175 (1957).
- [2] V.L. Ginzburg, *Sov. Phys. JETP*, **4**, 153 (1957).
- [3] B.T. Matthias *et al.*, *Phys. Rev. Lett.*, **1**, 92 (1958).
- [4] A.A. Abrikosov and L.P. Gor'kov, *Sov. Phys. JETP*, **12**, 1243 (1961).
- [5] G. Bednorz and K.A. Müller, *Z. Phys.*, **B64**, 189 (1986).
- [6] R.J. Cava *et al.*, *Nature*, **367**, 252 (1994).
- [7] J. Kondo. *Progr. Theoret. Phys.*, **32**, 37 (1964).
- [8] J.W. Lynn. *et al.*, *Phys. Rev. B*, **55**, 6584 (1997).

- [9] S.K. Dhar. *et al.*, *Solid State Commun.*, **98**, 985 (1996).
- [10] S.K. Sinha *et al.*, *Phys. Rev. B*, **51**, 681 (1995).
- [11] A.D. Hillier *et al.*, *Applied Magnetic Resonance*, **13**, 95 (1997).
- [12] T. Siegrist *et al.*, *Nature*, **367**, 252 (1994).
- [13] H. Kawano *et al.*, *Phys. Rev. Lett.*, **77**, 4628 (1996).
- [14] J.P. Carbotte, *Rev. Mod. Phys.*, **62**, 1027 (1990).
- [15] L.F. Mattheiss *et al.*, *Solid State Communications*, **91**, 587 (1994).
- [16] A.K. Gangopadhyay *et al.*, *Physica C*, **264**, 281 (1996).
- [17] M. Divis *et al.*, (Unpublished).
- [18] P. Dervenagas *et al.*, *Phys. Rev. B*, **52**, 9839 (1995).
- [19] M.B. Maple, *Topics in Current Physics*, Vol. 32, Springer Verlag (1983)
- [20] T.E. Grigereit *et al.*, *Phys. Rev. Lett.*, **73**, 2756 (1994).
- [21] L.J. Chang *et al.*, *Phys. Rev B*, **54**, 9031 (1996).
- [22] S.L. Bud'ko *et al.*, *Physica B*, **230-232**, 859 (1997).
- [23] A. Yatskar *et al.*, *Phys. Rev. B*, **54**, 3772 (1996).
- [24] R. Sala *et al.*, *Phys. Rev. B*, **56**, 6195 (1997).

CHAPTER 2

RARE EARTH CORRELATED ELECTRON BEHAVIOUR

In this chapter, the different types of rare earth correlated electron behaviour are discussed. The first part describes the rare earth standard model that provides an accurate description of many rare earth compounds. The second part describes heavy fermion and valence fluctuation behaviour in compounds that have dilute and concentrated distributions of Kondo ions. In both parts, the interplay between long range magnetic order, heavy fermion or valence fluctuation behaviour and superconductivity is stressed.

2.1 The rare earth standard model.

The rare earth or lanthanide series is made up of the fifteen elements from lanthanum to lutetium. The electronic structure consists of a xenon core with a partially filled $4f$ shell surrounded by a singularly occupied $5d$ shell and a full $6s$ shell.

Rare earth electronic configuration = xenon + $4f^n [5d^1 6s^2]$,

(lanthanum has $n = 0$, lutetium has $n = 14$).

The series is further divided into the light and heavy rare earths, depending on whether the $4f$ shell is less or more than half filled [1].

2.1.1 The free atom.

2.1.1.1 Solution of the non-relativistic Hamiltonian.

The non-relativistic Hamiltonian for a free rare earth atom is

$$\mathcal{H} = -\frac{\hbar^2}{2m} \sum_i \nabla_i^2 + \sum_i V_{\text{nuc}}(\underline{r}_i) + \frac{1}{2} \frac{1}{4\pi\epsilon_0} \sum_{ij} \frac{e^2}{|\underline{r}_i - \underline{r}_j|}. \quad \text{Eq 2.1}$$

The first two terms correspond to the kinetic energy of the electrons and their coulomb interaction with the nucleus respectively. The last term represents the coulomb interaction of the electrons with one another. In the Hamiltonian's present form, the calculation of the eigenstates of the atom is impossible due to the complexity of the intra-atomic coulomb interaction. In order to determine the eigenstates, the problem can be reformulated as a series of single electron Hamiltonians where the coulomb interaction of an electron with all the other charges in the atom is replaced with an effective potential $V_{\text{eff}}(\underline{r})$,

$$\mathcal{H} = -\frac{\hbar^2}{2m} \nabla^2 + V_{\text{eff}}(\underline{r}). \quad \text{Eq 2.2}$$

If this is done, the resulting single electron wavefunctions can be calculated. The solutions can be written as a product of a radial function, a spherical harmonic and a spin function

$$\psi_{n l m_l m_s}(\underline{r}, \sigma) = i^l R_{n l}(r) Y_{l m_l}(\hat{r}) \chi_{m_s}. \quad \text{Eq 2.3}$$

One of the most important features arising from the above analysis is that the $4f$ radial function lies within the $5d$ and $6s$ radial functions which is extremely important in explaining the properties of rare earth ions in compounds. The increasing nuclear charge and incomplete screening results in a decrease in the radii of the ion as n increases which is referred to as the lanthanide contraction. The angular dependence of the $4f$ wavefunctions leads to highly anisotropic charge distributions with pronounced multipoles [2].

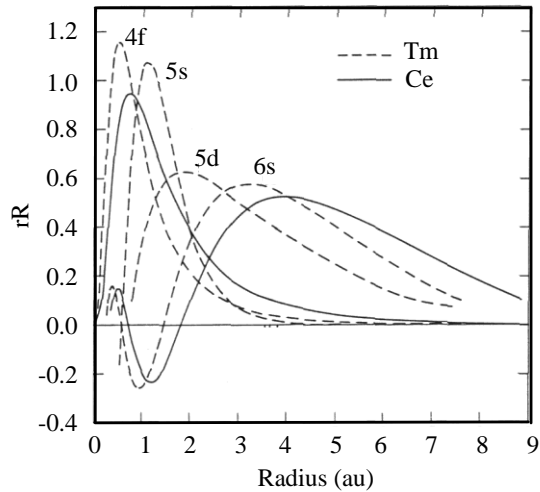


Fig 2.1 : The radial functions of the single electron atomic wavefunctions [2].

Cerium ($n = 1$) and Thulium ($n = 13$) are shown.

The electronic wavefunction for the whole atom is constructed from a sum of the single electron wavefunctions. The exchange interaction between the electrons couples their spins \underline{s}_i to give the total spin \underline{S} , and the coulomb interaction couples the orbital angular momenta \underline{l}_i to give the total orbital angular momentum \underline{L} . The state with lowest energy is that which has the maximum values of S and L [3].

2.1.1.2 The spin-orbit interaction.

Relativistic effects are important in the rare earths due to their large atomic masses and may be added as perturbations to the non-relativistic Hamiltonian. The most important relativistic effect is the coupling of the total orbital angular momentum \underline{L} and the total spin \underline{S} to give the total angular momentum $\underline{J} = \underline{L} + \underline{S}$ [2]. This is called the spin-orbit interaction and the magnitude of the total angular momentum J in the ground state is given by

$$J = \begin{cases} |L + S| & (4f \text{ subshell is more than half full}) \\ |L - S| & (4f \text{ subshell is less than half full}) \end{cases} \quad \text{Eq 2.4}$$

The degeneracy of this ground state g is given by

$$g = 2J + 1 \quad \text{as } M_J = -J, \dots, 0, \dots, J, \quad \text{Eq 2.5}$$

and the effective magnetic moment associated with it is

$$\underline{\mu} = \left[\frac{3}{2} + \frac{S(S+1) - L(L+1)}{2J(J+1)} \right] \mu_B \underline{J} = g_J \mu_B \underline{J}. \quad \text{Eq 2.6}$$

2.1.2 Interactions with other ions.

When rare earth atoms are placed in a metallic compound, the $5d$ and $6s$ electrons leave the atom and contribute to the itinerant conduction band. In the majority of compounds, the $4f$ electrons remain localised to the nucleus, resulting in a rare earth valence of $+3$. The localised nature of the $4f$ electrons means that the wavefunctions, derived above, may be used as a basis for calculating the rare earth ground state in rare earth compounds. However, inter-ionic interactions are important and must be included in order to calculate the properties of the compound.

2.1.2.1 The crystalline electric field (C.E.F.) interaction.

The rare earth $4f$ electrons experience a coulomb interaction with all the electronic and nuclear charges on the neighbouring ions. As the $4f$ electrons are shielded by the $5d$ and $6s$ electrons, the C.E.F. interaction is weaker than the spin-orbit interaction, but it may still have a significant effect on the magnetic properties of the rare earth ions. The potential between the $4f$ electrons of a single rare earth ion and the surrounding charge distributions can be expanded in spherical harmonics,

$$V(\underline{r}) = \int \frac{e\rho(\underline{R})}{|\underline{r} - \underline{R}|} d\underline{R} = \sum_{lm} A_l^m r^l Y_l^m(\theta, \phi), \quad \text{Eq 2.7}$$

where

$$A_l^m = (-1)^m \frac{2\pi}{(2l+1)} \int \frac{\rho(\underline{R})}{R^{l+1}} Y_l^{-m}(\theta, \phi) d\underline{R}, \quad \text{Eq 2.8}$$

and $\rho(\underline{R})$ is the charge density of the external electrons and nuclei. The number of terms in the expansion depends on the nature of the wavefunction in the crystal field. For the $4f$ wavefunction, terms with $l > 6$ are not included and $|m|$ is less than or equal to l always. The number of terms may be reduced further depending on the symmetry of the rare earth site. For example, in the rare earth nickel borocarbides, the tetragonal symmetry of the unit cell allows only the terms A_2^0 , A_4^0 , A_4^4 , A_6^0 and A_6^4 . Calculations of the transition matrix elements of equation 2.7 are greatly simplified by first expressing the spherical harmonics in terms of Cartesian coordinates. The Wigner-Eckart theorem then allows the crystal field Hamiltonian to be written in terms of the operator equivalents, which are functions of the projection of the total angular momentum operator \underline{J} onto the Cartesian axes (J_x, J_y, J_z). If this is done, and a sum over the lattice sites performed, the crystal field Hamiltonian can be written as

$$\mathcal{H}_{\text{cf}} = \sum_i \sum_{lm} A_l^m \alpha_l \langle r^l \rangle O_l^m(\underline{J}_i) = \sum_i \sum_{lm} B_l^m O_l^m(\underline{J}_i), \quad \text{Eq 2.9}$$

where the α_l are the Stevens factors which are functions of L , S and J , the $\langle r^l \rangle$ are the expectation values of the $4f$ electron radii, and the $O_l^m(\underline{J}_i)$ are the Stevens operator equivalents which are tabulated. In principle, the crystal field parameters B_l^m can be calculated. In practice, this is usually not attempted due to the difficulty in determining $\rho(\underline{R})$, and their values are measured experimentally. The effect of the C.E.F. interaction is to break the directional degeneracy of the $4f$ magnetic moment. A preferred direction, or 'easy' axis, is introduced along which it is energetically favourable for the magnetic moment to align. As this effect is identical at each rare earth site, in compounds that magnetically order, the C.E.F. interaction favours the formation of commensurate structures [4].

2.1.2.2 The exchange interaction.

As the rare earth $4f$ electrons are highly localised and lie within the $5s$ and $5p$ electrons, there is virtually no overlap of their wavefunctions and therefore the direct exchange interaction is negligible. However, an indirect exchange interaction, the Ruderman, Kittel, Kasuya, Yosida (R.K.K.Y.) interaction, does occur via direct exchange with the conduction electrons. The Heisenberg direct exchange Hamiltonian for the interaction between a rare earth ion at position \underline{R} , with total angular momentum \underline{J} , and a conduction electron spin density $\underline{s}(\underline{r})$ can be written as

$$\mathcal{H}_{fs} = -(g_J - 1) \int j(\underline{r} - \underline{R}) \underline{J} \cdot \underline{s}(\underline{r}) d\underline{r} = -g \mu_B \int \underline{H}(\underline{r}) \cdot \underline{s}(\underline{r}) d\underline{r}, \quad \text{Eq 2.10}$$

where $j(\underline{r} - \underline{R})$ is the exchange parameter. Therefore, the effective magnetic field experienced by the conduction electrons due to the rare earth ion is given by

$$\underline{H}(\underline{r}) = \frac{(g_J - 1)}{g \mu_B} j(\underline{r} - \underline{R}) \underline{J}. \quad \text{Eq 2.11}$$

Using equations 2.11 and 3.13, the spin density induced in the conduction electrons at position \underline{r} by a rare earth ion at position \underline{R}_k , with total angular momentum \underline{J}_k , is

$$\underline{s}_k(\underline{r}) = \frac{1}{g \mu_B V} \int \chi(\underline{r} - \underline{r}') \underline{H}_k(\underline{r}') d\underline{r}' = \frac{(g_J - 1)}{g^2 \mu_B^2 V} \int \chi(\underline{r} - \underline{r}') j(\underline{r} - \underline{R}_k) \underline{J}_k d\underline{r}', \quad \text{Eq 2.12}$$

where $\chi(\underline{r} - \underline{r}')$ is the non local susceptibility which can be written as a scalar if the crystal is unmagnetised and the spin-orbit coupling of the conduction electrons is ignored. The indirect exchange Hamiltonian for the interaction between a rare earth ion at position \underline{R}_i , with total angular momentum \underline{J}_i , and this spin density is therefore

$$\begin{aligned} \mathcal{H}_{ik} &= -g \mu_B \int \underline{H}_i(\underline{r}) \cdot \underline{s}_k(\underline{r}) d\underline{r} \\ &= -\frac{(g_J - 1)^2}{g^2 \mu_B^2 V} \iint j(\underline{r} - \underline{R}_i) \underline{J}_i \chi(\underline{r} - \underline{r}') j(\underline{r} - \underline{R}_k) \underline{J}_k d\underline{r}' d\underline{r}. \end{aligned} \quad \text{Eq 2.13}$$

If the Fourier transform of the above equation is taken, and a sum over rare earth lattice sites performed, it becomes

$$\mathcal{H}_{\text{RKKY}} = -\frac{1}{2} \sum_{ik} \left[\frac{V}{N^2} \frac{(g_J - 1)^2}{g^2 \mu_B^2} \sum_{\underline{q}} |j(\underline{q})|^2 \chi(\underline{q}) \exp(i \underline{q} \cdot (\underline{R}_i - \underline{R}_k)) \right] \underline{J}_i \cdot \underline{J}_k, \quad \text{Eq 2.14}$$

which is the Hamiltonian for the R.K.K.Y. interaction. The expression in square brackets is the indirect exchange parameter between the rare earth ions and is a function of the direct exchange parameter and the conduction electron susceptibility. It can be seen from equation 2.14 that the R.K.K.Y. interaction will favour an arrangement of the rare earth magnetic moments that is modulated by a wavevector that corresponds to a maxima in the product $|j(\underline{q})|^2 \chi(\underline{q})$. Assuming the above approximations, the conduction electron susceptibility can be written as

$$\chi(\underline{q}) = \frac{2 \mu_B^2}{V} \sum_{\underline{k}} \frac{f_{\underline{k}} - f_{\underline{k}+\underline{q}}}{E_{\underline{k}+\underline{q}} - E_{\underline{k}}}. \quad \text{Eq 2.15}$$

Evaluation of this expression for a real rare earth compound requires a detailed knowledge of the Fermi surface. However, it is clear that a large contribution to the sum over \underline{k} is made by pairs of electronic states with similar energies, separated by a wavevector \underline{q} . Therefore, the conduction electron susceptibility will have a large value at $\underline{q} = \underline{Q}$, if the Fermi surface has large parallel regions separated by a wavevector \underline{Q} . This is called ‘nesting’ of the Fermi surface, and the peaks it gives rise to in the conduction electron susceptibility are called Kohn anomalies. These are often extremely important in determining the modulation wavevectors of the rare earth

magnetic moments in the magnetically ordered state. As the modulation wavevectors do not depend on the periodicity of the crystal lattice, the R.K.K.Y. interaction usually favours the formation of incommensurate magnetic order [4].

2.1.2.3 The dipolar interaction.

In addition to the R.K.K.Y. interaction, the rare earth magnetic moments interact via the classical dipolar interaction. The Hamiltonian for the dipolar interaction between two rare earth ions with magnetic moments \underline{J}_i and \underline{J}_j , at positions \underline{R}_i and \underline{R}_j , is given by

$$\mathcal{H}_{\text{dp}} = -(g_J \mu_B)^2 \frac{\underline{J}_i \cdot \underline{J}_j - 3(\underline{J}_i \cdot \hat{r})(\underline{J}_j \cdot \hat{r})}{r^3}, \quad \text{Eq 2.16}$$

where $r = |\underline{R}_i - \underline{R}_j|$. This interaction extends over a long distance and is highly anisotropic. In many rare earth compounds, it is considerably weaker than the R.K.K.Y. interaction. In the heavy rare earth nickel borocarbides, it plays no role in determining the magnetically ordered structure. The above Hamiltonian can be expressed in a similar form to equation 2.14, and the combined anisotropic Hamiltonian for the indirect exchange and dipolar interactions can be written as

$$\mathcal{H}_{(\text{RKKY}/\text{dp})} = -\frac{1}{2} \sum_{\alpha\beta} \sum_{ik} \left[j_{(\text{RKKY})ik} \delta_{\alpha\beta} + j_{(\text{dp})ik} \alpha\beta \right] J_{i\alpha} J_{k\beta}, \quad \text{Eq 2.17}$$

where α and β represent the Cartesian coordinate axes [2].

2.1.3 Magnetic structures and the mean field approximation.

From equations 2.9 and 2.17, the total Hamiltonian for the lattice of rare earth ions in a compound can be written as

$$\mathcal{H}_{\text{REL}} = \mathcal{H}_{\text{CF}} + \mathcal{H}_{\text{(RKKY/dp)}} \quad \text{Eq 2.18}$$

The second term in this Hamiltonian contains two ion operators of the form $\underline{J}_i \cdot \underline{J}_k$. If the magnetic structure of the rare earth lattice is to be calculated, these two ion operators must be decomposed into terms containing only single ion operators. The two ion operator may be expanded as

$$\underline{J}_i \cdot \underline{J}_k = \left(\underline{J}_i - \langle \underline{J}_i \rangle \right) \cdot \left(\underline{J}_k - \langle \underline{J}_k \rangle \right) + \underline{J}_i \cdot \langle \underline{J}_k \rangle + \underline{J}_k \cdot \langle \underline{J}_i \rangle - \langle \underline{J}_i \rangle \cdot \langle \underline{J}_k \rangle. \quad \text{Eq 2.19}$$

The first term on the right hand side is associated with two site fluctuations, and can be neglected in the mean field approximation as only the static magnetic structure is being considered. Therefore, the above expansion allows the R.K.K.Y./ dipolar Hamiltonian to be written in the form

$$\mathcal{H}_{\text{(RKKY/dp)}} = -\frac{1}{2} \sum_{\alpha\beta} \sum_i \left(J_{i\alpha} - \frac{1}{2} \langle J_{i\alpha} \rangle \right) \cdot \sum_k j_{ik\alpha\beta} \langle J_{k\beta} \rangle, \quad \text{Eq 2.20}$$

where the right hand side of the dot-product is the $\alpha\beta^{\text{th}}$ component of the mean field at the i^{th} site. The above equation can be combined with the crystal field Hamiltonian to give the mean field approximation to \mathcal{H}_{REL} . Provided that there are no other significant contributions to the rare earth lattice Hamiltonian, \mathcal{H}_{REL} can be used to calculate the magnetic structure of the rare earth lattice in the magnetically ordered state. The magnetic structure is determined by a competition between the R.K.K.Y./ dipolar interaction, tending to produce incommensurate structures, and the C.E.F. interaction, which favours the formation of commensurate magnetic order [2].

2.1.4 Coexistence of magnetism and superconductivity.

In most compounds, consisting of rare earth ions embedded in a metallic environment, superconductivity does not occur. This is because the exchange interaction between

the rare earth $4f$ magnetic moment and the conduction electrons prevents the formation of the superconducting electron pairs. This occurs as the exchange interaction has the effect of raising the energy of one of the electrons in the pair and reducing the energy of the other. This is called magnetic pair breaking. However, in some compounds, where the rare earth ions are well isolated from the conduction electrons, the interaction between the two is weak and superconductivity can occur. Magnetic pair breaking still exists, but now it results in a suppression of T_C rather than a complete removal of superconductivity [5].

2.1.4.1 Abrikosov-Gor'kov theory and the de Gennes factor.

The Abrikosov-Gor'kov theory predicts the T_C of an alloy produced by dissolving rare earth ions in a superconducting matrix [6]. The theory holds for positive values of the exchange parameter between the conduction electrons and the rare earth ions j . The drop in the superconducting transition temperature from the undoped value with increasing concentration of the rare earth ions n is given by

$$\left. \frac{dT_C}{dn} \right|_{n=0} = - \left(\frac{\pi^2}{2} \right) k_B^{-1} g_c(0) j^2 (g_J - 1)^2 J(J+1), \quad \text{Eq 2.21}$$

where $g_c(0)$ is the conduction electron density of states, and J is the total angular momentum of the rare earth ion. The factor $(g_J - 1)^2 J(J+1)$ is called the de Gennes factor.

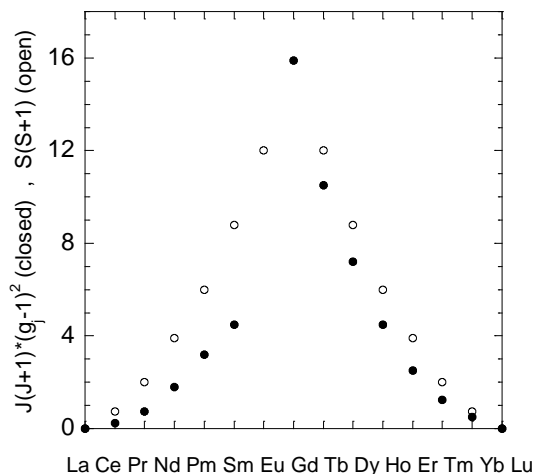


Fig 2.2 : The de Gennes factor (closed) and the value of $S(S+1)$ (open) for the rare earth ions.

The de Gennes factor scales roughly with the value of $S(S+1)$ and reaches a maximum for Gadolinium where the $4f$ shell is exactly half full ($S = 7/2$, $L = 0$ and $J = 7/2$).

2.1.4.2 The suppression of superconductivity by the Kondo effect.

A rare earth or actinide ion that has a negative exchange parameter with the conduction electrons of the a host compound is called a Kondo ion. If such an ion is placed in a superconducting compound, there is a competition between the formation of a superconducting ground state with energy $E_S = k_B T_{C0}$, and the formation of a Kondo singlet with energy $E_K = k_B T_K$ due to local antiferromagnetic correlations between the Kondo ion $4f$ electrons and the conduction electrons. Here, T_{C0} is the superconducting transition temperature of the undoped compound. For $T_K \leq T_{C0}$, the value of T_C is depressed by an amount larger than that predicted by the Abrikosov-Gor'kov theory. This depression reaches a maximum at $T_K = T_{C0}$ when superconductivity is completely removed. For $T_K \ll T_{C0}$, there can be re-entrant superconducting behaviour: on cooling, at temperatures below the onset of superconductivity at an upper critical temperature T_{C1} , the increase in the scattering due to the Kondo effect causes the compound to re-enter the normal state at T_{C2} [7].

2.1.4.3 Coexistence of long range magnetic order and superconductivity.

The onset of long range magnetic order in a superconductor establishes a static exchange field at the superconducting electron sites. If this field exceeds the paramagnetic limiting field given by

$$H_P = \left[\frac{g_c(0)}{\chi_n - \chi_s} \right]^{1/2} \Delta, \quad \text{Eq 2.22}$$

where $g_c(0)$ is the superconducting electron density of states, Δ is the energy gap, and χ_n and χ_s are the normal and superconducting electron magnetic susceptibilities, the superconductivity will be destroyed [8]. If χ_s can be increased, H_P will also increase, and the coexistence of superconductivity and a static exchange field will be more favourable.

The paramagnetic limiting field is considered in several theories describing the coexistence of superconductivity and ferromagnetic order. The Gor'kov and Rusinov theory provides a simple explanation of the re-entrant superconductivity seen in some of the ferromagnetic rare earth ternary compounds [9]. Below the superconducting transition temperature, in the presence of spin orbit or exchange scattering, χ_s will have a finite value, and R.K.K.Y. ordering of the magnetic ions can occur. The raised value of the superconducting electron susceptibility also allows the superconducting order to persist in the presence of the static exchange field. However, as the temperature is lowered, the exchange field increases, eventually exceeding H_P , and the compound re-enters the normal state. The above theory neglects the q dependence of the superconducting electron susceptibility. The Anderson and Suhl theory suggests that the ferromagnetic order will contain an oscillatory modulation corresponding to the q value for which $\chi_s(q)$ attains a maximum [10]. A sinusoidally modulated state coexisting with superconductivity has been observed in ErRh_4B_4 [11]. However, the formation of this state has been attributed to effects other than the exchange interaction considered by Anderson and Suhl, such as the formation of spontaneous vortex lattices [12] or the electromagnetic interaction between the rare earth magnetic moments and the persistent current [13].

The first theory describing the coexistence of superconductivity and commensurate long range antiferromagnetic order was provided by Baltensperger and Strässler [14]. They concluded that superconductivity and antiferromagnetic order are not mutually exclusive if the exchange field averages to zero over the superconducting coherence length. However, the magnetic order still has a large effect on the superconductivity. Their most striking prediction was the finite momentum pairing of the superconducting electrons into states $(\underline{k}\uparrow, -\underline{k} + \underline{Q}\downarrow)$ where \underline{Q} is a reciprocal lattice vector. Subsequent theories have described other modifications of the superconductivity. These include a prediction that, around T_N , magnetic moment fluctuations increase the magnetic pair breaking, and below T_N , magnons decrease the strength of the phonon mediated electron-electron pairing mechanism [15]. To date, no accepted theory of the coexistence of incommensurate antiferromagnetic order and superconductivity has been put forward. A theory by Morozov describing the suppression of superconductivity by incommensurate order in $\text{HoNi}_2\text{B}_2\text{C}$ concludes that an interaction between the incommensurate Bragg planes and the electron Fermi surface allows superconductivity to be destroyed by small concentrations of non-magnetic impurities [16]. This interaction is not present when the compound is in a commensurate antiferromagnetic ordered state.

2.2 Heavy fermion and valence fluctuation behaviour in rare earth compounds.

2.2.1 Introduction.

Heavy fermion and valence fluctuation behaviour can arise in compounds containing rare earth elements such as Ce or Yb, or actinide elements such as U or Np. This thesis is concerned with rare earth compounds; therefore, the actinide compounds will not be considered here. The rare earth standard model describes compounds in which the rare earth $4f$ electrons are localised. The conduction band is made up of the rare earth $5d$ and $6s$ electrons and electrons from other ions in the compound. In heavy fermion and valence fluctuation compounds, the $4f$ electrons are not completely localised and, to varying degrees, hybridise with the conduction electrons. At high temperatures, the thermal population of energetic conduction electron states ensures

that these compounds exhibit behaviour broadly consistent with the standard model. For example, the static susceptibility is indicative of non-interacting local moment paramagnetism of the $4f$ electrons. As the temperature is lowered below a characteristic temperature, T_K or the Kondo temperature, the thermodynamic behaviour of these compounds becomes dominated by excitations within the rare earth $4f$ /conduction electron correlated system. The explanation of the low temperature behaviour presents a major challenge to theoretical physicists and is one of the main reasons for experimental interest in heavy fermion and valence fluctuation compounds. For example, heavy fermion compounds, in particular, display coexistent localised and itinerant electronic behaviour which is difficult to reconcile with traditional theoretical models. The behaviour of heavy fermion and valence fluctuation compounds is often described using Fermi liquid theory. The interactions between the $4f$ and the conduction electrons are considered to renormalise or scale the properties of the non-interacting conduction electrons. The resulting quasi-particles therefore possess, to some extent, the character of both the conduction and the $4f$ electrons.

In valence fluctuation compounds, the $4f$ /conduction electron mixing is strong enough to cause both spin fluctuations and fluctuations in the $4f$ charge. The values of T_K are high in these compounds (~ 100 K). In heavy fermion compounds, the mixing is too weak to produce charge fluctuations and only the spin fluctuations remain. The values of T_K are much lower than in valence fluctuation compounds and the more localised behaviour of the quasi-particles results in extremely large values of the effective mass.

In compounds with a low concentration of rare earth ions, the interactions between different rare earth sites can be ignored. If spin-orbit and crystal field effects are included, the properties of these compounds can be understood in terms of $4f$ /conduction electron mixing occurring independently on each rare earth site. The Anderson model, outlined below, describes this situation very well. In more concentrated compounds, the interactions between different rare earth sites can no longer be ignored. Exchange interactions between the rare earth sites can lead to long

range magnetic order and coherence between the sites can lead to superconductivity. The concentrated compounds are more difficult to understand as it is here where the coexistence of localised and itinerant behaviour is most conspicuous. Models are often based on the formation of narrow itinerant bands of interacting quasi-particles.

2.2.2 The Fermi liquid theory.

The phenomenological Fermi liquid theory describes an interacting fermion system. In dilute heavy fermion and valence fluctuation compounds the interactions are taken to be those between the $4f$ and the conduction electrons. In a simple model, the band structure of the conduction electrons is ignored and they are approximated by a free electron gas. The interactions are considered to readjust the Fermi sphere of the conduction electrons. The energy required to add an electron near the surface of this readjusted Fermi sphere is calculated to be

$$\varepsilon(\underline{k}) = \mu + \frac{\hbar^2 k_F}{m^*} |\underline{k} - \underline{k}_F|. \quad \text{Eq 2.23}$$

As the entire Fermi sphere has been readjusted as a result of the interactions, the energy of this electron is different to that of a free electron. The interactions are said to ‘dress’ the electron and its consequential lack of physical identity results in it being referred to as a quasi-particle. The increase in the energy required to create a quasi-particle in moving away from the Fermi surface is characterised by an effective mass m^* . If more quasi-particles are introduced into the system, their energies will be different from those predicted by equation 2.23 as the energy of any one quasi-particle is now a function of the distribution of all the others. If the quasi-particle distribution function is known, the thermodynamic properties of the interacting system can be calculated. It can be shown that the electronic specific heat of the Fermi liquid has the same form as an ideal gas but with m replaced by m^* . Similarly, the static susceptibility is proportional to the Pauli susceptibility of a free electron gas, but is enhanced by a factor depending on m^*/m . Therefore, both the conduction electron mass, or the electronic specific heat, and the static susceptibility are enhanced or renormalised by the interactions with the $4f$ electrons. In more concentrated heavy

fermion and valence fluctuation compounds, the interactions between different rare earth sites can be incorporated within the Fermi liquid theory by considering interactions between the quasi-particles [4].

2.2.3 Dilute compounds.

If spin-orbit and crystal field effects are taken into account, the electronic properties of dilute heavy fermion and valence fluctuation compounds are described very well by the Anderson model [16].

In this model the conduction electrons form a single band consisting of the $5d$ and $6s$ electrons from the rare earth ions and the conduction electrons from other ions in the compound. In the absence of mixing with the conduction electrons, the ground state of the $4f$ electrons, subject to spin-orbit and crystal field effects, is described by the rare earth standard model. However, interactions via the R.K.K.Y. exchange between the $4f$ electrons on different rare earth sites are neglected as the rare earth concentration is low.

The Anderson Hamiltonian describes a mixing between the ground state multiplet of the $4f$ electrons and the conduction band,

$$\mathcal{H}_A = \sum_{k,m} \varepsilon_k c_{k m}^+ c_{k m} + \varepsilon_f \sum_m f_m^+ f_m + V \sum_{k,m} (f_m^+ c_{k m} + c_{k m}^+ f_m) + U \sum_{m>m'} f_m^+ f_m f_{m'}^+ f_{m'}.$$

Eq 2.24

The first term is the energy of the electrons in the conduction band; ε_k is the conduction electron energy, and $c_{k m}^+$ and $c_{k m}$ are the creation and annihilation operators. The second term is the energy of the $4f$ electrons; f_m^+ and f_m are the creation and annihilation operators for a $4f$ electron with energy ε_f . The hopping matrix element which describes the mixing of the $4f$ and the conduction electrons is V . The last term represents the interaction of the $4f$ electrons with each other. The Fermi level lies at an energy of zero and the unhybridised $4f$ electron level lies below

it (ε_f is negative). The conduction electron bandwidth is given by D , and V is related to the hybridised width of the $4f$ electron level Δ (when the $4f$ electron interaction energy U is zero) by

$$\Delta = \pi g_c(0)V^2, \tag{Eq 2.25}$$

where $g_c(0)$ is the conduction electron density of states for both spin directions at the Fermi level.

In valence fluctuation compounds, the hybridised width of the $4f$ electron level is greater than its separation from the conduction band ($|\varepsilon_f| \leq \Delta$). This overlap gives rise to charge fluctuations. In heavy fermion systems, the hybridised width of the $4f$ electron level is much less than its separation from the conduction band ($|\varepsilon_f| \gg \Delta$), and charge fluctuations do not occur.

If $|\varepsilon_f| \gg \Delta$, $U \gg \Delta$ and $U + 2\varepsilon_f = 0$, the Anderson Hamiltonian represents heavy fermion behaviour, and in this region can be transformed into the Coqblin-Schrieffer Hamiltonian [18]

$$\mathcal{H}_{CS} = \sum_{k,m} \varepsilon_k c_{km}^\dagger c_{km} - j \sum_{k,k',m,m'} c_{k'm'}^\dagger f_m^\dagger f_{m'} c_{km}, \tag{Eq 2.26}$$

which represents the weak $4f$ / conduction electron mixing as an effective exchange interaction with coupling constant

$$j = V^2 \frac{U}{\varepsilon_f(\varepsilon_f + U)}. \tag{Eq 2.27}$$

For $U + \varepsilon_f > 0$, the exchange constant is negative and this results, at low temperatures, in a reduction in the effective magnetic moment at the rare earth site.

For heavy fermion systems where the lowest crystal field multiplet is a doublet and excitations to the excited multiplets sufficiently energetic to be ignored, the Coqblin-Schrieffer Hamiltonian can be further transformed into the Kondo Hamiltonian

$$\mathcal{H}_K = \sum_{\underline{k}, \sigma} \varepsilon_{\underline{k}} c_{\underline{k}\sigma}^+ c_{\underline{k}\sigma} - j \sum_{\underline{k}\underline{k}', \sigma\sigma'} \underline{J} c_{\underline{k}'\sigma'} c_{\underline{k}\sigma}, \quad \text{Eq 2.28}$$

where \underline{J} and $\underline{\sigma}$ give the angular momentum associated with the rare earth site and conduction electrons respectively [19].

A solution of the Anderson, Coqblin-Schrieffer or Kondo Hamiltonians gives a value for the Kondo temperature, below which valence fluctuation or heavy fermion behaviour are displayed

$$T_K = \frac{D}{k_B} \exp\left(\frac{\pi \varepsilon_f}{g \Delta}\right), \quad \text{Eq 2.29}$$

where g is the degeneracy of the unhybridised $4f$ multiplet. Below the Kondo temperature, the thermodynamic behaviour of these compounds becomes dominated by excitations within the rare earth $4f$ / conduction electron correlated system. These quasi-particle excitations give rise to a large peak in the electronic density of states near the Fermi level. This phenomenon is known as the Kondo resonance and is one of the main theoretical predictions associated with heavy fermion and valence fluctuation behaviour. It can be experimentally observed by X-ray absorption spectroscopy. At temperatures above the Kondo temperature, the resonance is washed out as higher energy excitations become important in determining the properties of the compound.

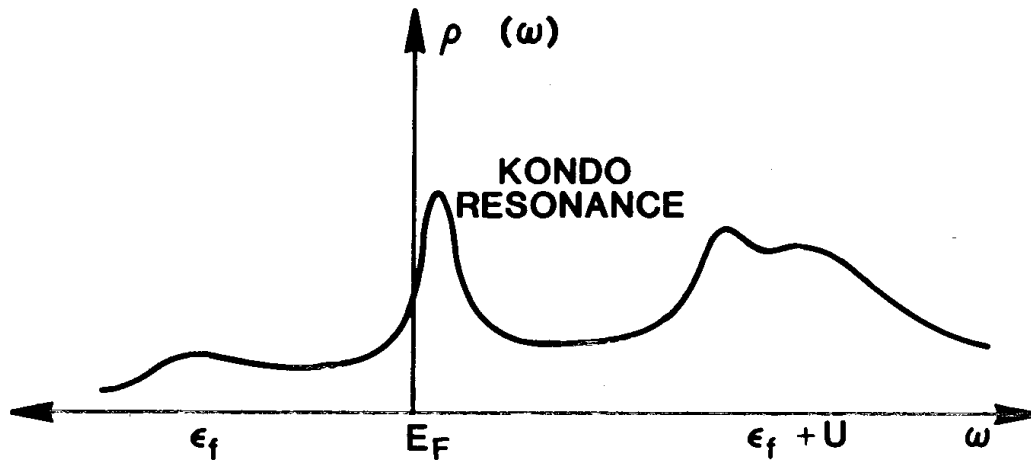


Fig 2.3 : The Kondo resonance. The density of states of the quasi-particles verses energy. E_F is the Fermi level and ϵ_f is the position of the unmixed $4f$ electron level. U is the $4f$ electron self interaction energy.

The thermodynamic behaviour of the quasi-particles is similar in many respects to that of a non-interacting electron gas. However, the large density of quasi-particle states at the Fermi level leads to an effective electronic mass scaled by

$$\frac{m^*}{m} \propto \frac{T_F}{T_K} . \quad \text{Eq 2.30}$$

For heavy fermion compounds, where T_K is low (~ 10 K), the effective mass is often of the order $10^3 m$. In many compounds, as the temperature tends towards absolute zero, the antiferromagnetic correlations amongst the $4f$ and the conduction electrons leads to a complete removal of the rare earth magnetic moment. In this case, the ground state of the compound is a non-magnetic singlet [20].

2.2.3.1 Magnetic specific heat.

If the phonon contribution is subtracted, the Kondo resonance is clearly visible in the specific heat of heavy fermion and valence fluctuation compounds.

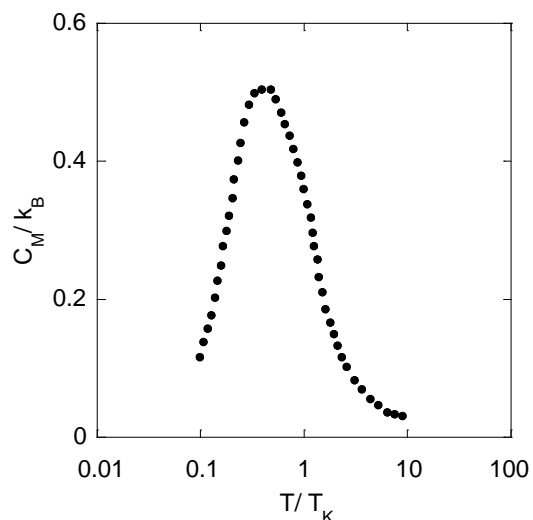


Fig 2.4 : Typical magnetic specific heat verses temperature for a dilute heavy fermion or valence fluctuation compound.

The general form of the magnetic specific heat is the same for heavy fermion and valence fluctuation compounds. The exact position and width of the Kondo peak is dependent on the degeneracy of the $4f$ ground state. Variations from the above form can occur in dilute compounds where the crystal field splitting is the same order of magnitude as the Kondo energy. In these compounds, the Kondo peak may be shifted in temperature and superimposed on a background due to transitions to the excited crystal field levels. In heavy fermion compounds, the linear contribution to the specific heat is very large (the Sommerfeld coefficient lies in the range $400 \text{ mJ mol}^{-1} \text{ K}^{-2} < \gamma < 1.6 \text{ J mol}^{-1} \text{ K}^{-2}$) due to the enhanced electron effective mass [21].

2.2.3.2 Static susceptibility.

The form of the static susceptibility depends on the extent to which the compound exhibits heavy fermion or valence fluctuation behaviour. This is reflected in the value of the average rare earth $4f$ valence n_f . In the case of cerium or ytterbium ions, a valence of unity corresponds to the rare earth ion having an ionisation state of +3. In this state, a cerium ion will possess one $4f$ electron, and a ytterbium ion will possess one $4f$ hole (or 13 $4f$ electrons). As n_f decreases, and the compound moves towards valence fluctuation behaviour, a cerium ion will tend to lose its $4f$ electron, and a ytterbium ion will tend to lose its $4f$ hole (or gain an electron). These two processes

are related by an electron/ hole inversion and are qualitatively analogous. The static susceptibility also depends on the degeneracy of the $4f$ ground state multiplet involved in the formation of the Kondo resonance.

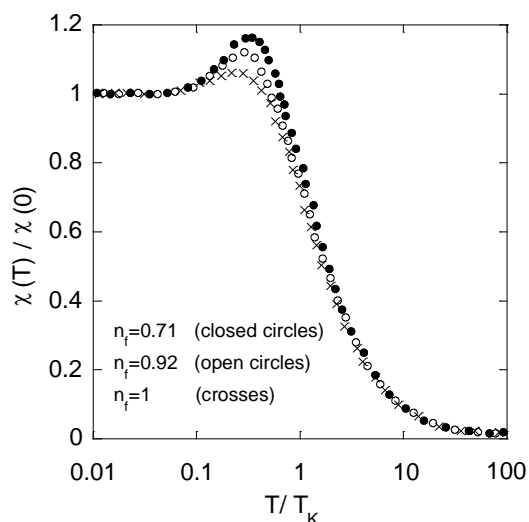


Fig 2.5 : Typical static susceptibility versus temperature for a dilute valence fluctuation or heavy fermion compound. Different values of the average rare earth valence n_f (electrons for Ce, holes for Yb) are shown for a $4f$ ground state degeneracy of $g = 6$.

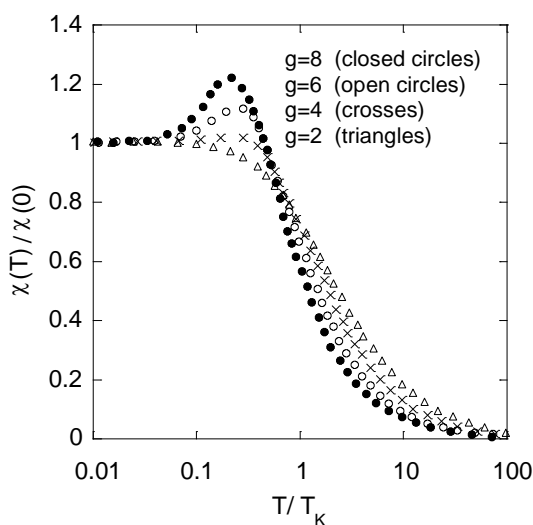


Fig 2.6 : Typical static susceptibility versus temperature for a dilute valence fluctuation or heavy fermion compound. Different values of g of the rare earth ground state multiplet are shown.

The most significant feature in figures 2.5 and 2.6 is the different types of behaviour above and below T_K . Above this temperature, the susceptibility is indicative of non-interacting local moment paramagnetism. As the temperature is reduced below T_K , the effective rare earth magnetic moment is reduced. This leads to a reduction in the paramagnetic contribution to the susceptibility. At very low temperatures, the susceptibility is entirely due to the temperature independent Pauli susceptibility of the

quasi-particles. Figure 2.5 shows the variation of the form of the static susceptibility as a function of n_f for a rare earth ground state multiplet with $g = 6$. As the value of n_f decreases (moving towards valence fluctuation behaviour), the peak in the susceptibility below T_K becomes more pronounced. Figure 2.6 shows the variation in the susceptibility as a function of the value of g of the rare earth ground state multiplet. The peak in the susceptibility becomes less pronounced as the value of g decreases. For $g = 2$, and values of n_f close to unity, the behaviour of the compound is described by the Kondo formulation of the Anderson Hamiltonian, and the susceptibility peak disappears completely [22].

2.2.3.3 Resistivity.

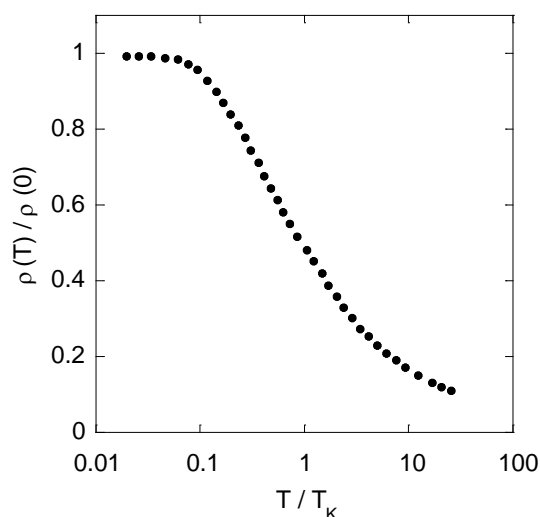


Fig 2.7 : Typical resistivity verses temperature for a dilute heavy fermion or valence fluctuation compound.

The form of the resistivity for heavy fermion and valence fluctuation compounds is the same. As the temperature is lowered, the proportion of conduction electrons involved in the formation of the Kondo resonance increases. This equates to an increase in the scattering of the conduction electrons by the rare earth $4f$ electrons. As the temperature tends towards absolute zero, the Kondo resonance becomes fully formed and the resistivity achieves a maximum. This behaviour should be contrasted with the resistivity of more concentrated rare earth systems [21].

2.2.4 Concentrated compounds.

In compounds with a high concentration of rare earth ions, the interactions between different rare earth sites become important. There is now a competition between the formation of a non-magnetic ground state via the Kondo effect and the formation of a magnetic ground state via the R.K.K.Y. interaction. The energy of both these ground states depends on the $4f/$ conduction electron exchange parameter j and the conduction electron density of states at the Fermi level. For small values of $|j g_c(0)|$, the energy of the R.K.K.Y. interaction is the greater, and the rare earth sites in the compound have stable local moments consistent with the standard model. For values of $|j g_c(0)|$ close to unity, the Kondo energy is the greater, and the compound displays valence fluctuation behaviour; in this regime, the magnetic moment of the $4f$ electrons is completely compensated by the conduction electrons, and the inter-site magnetic interactions are unimportant. In between these two extremes, the properties of the compound are more difficult to predict; in many heavy fermion compounds, hybridisation of the $4f/$ conduction electrons is observed coexisting with long range magnetic order of the substantially reduced $4f$ magnetic moments.

One theoretical description of concentrated heavy fermion and valence fluctuation compounds is given by the periodic Anderson Hamiltonian

$$\mathcal{H}_{PA} = \sum_{k,m} \varepsilon_k c_{km}^+ c_{km} + \varepsilon_f \sum_{m,i} f_{mi}^+ f_{mi} + V \sum_{k,m,i} \left[\exp(i\mathbf{k} \cdot \mathbf{R}_i) c_{km}^+ f_{mi} + \text{h.c.} \right] + U \sum_{m>m',i} f_{mi}^+ f_{mi} f_{m'i}^+ f_{m'i}, \quad \text{Eq 2.31}$$

where the intra-site electron hopping term of the Anderson Hamiltonian is replaced by a summation over all rare earth lattice sites at positions $\{\mathbf{R}_i\}$. A solution of this Hamiltonian predicts the formation of narrow itinerant bands of independent quasi-particles. The narrowness of these bands is responsible for the large density of states at the Fermi level (or Kondo resonance) seen in concentrated compounds. The energy profile of the Kondo resonance is more complicated than in dilute compounds, and

may no longer be isotropic, as it is now a function of the quasi-particle band structure and crystal symmetry of the compound. The R.K.K.Y. interaction can be included in the above analysis by introducing interactions between the quasi-particles; it can also be added explicitly to the periodic Anderson Hamiltonian. Both approaches predict long range magnetic order in the itinerant quasi-particle Fermi liquid [22]. This description has similar features to the Stoner theory of itinerant magnetic order in the transition metal elements [4].

2.2.4.1 Resistivity.

One of the most striking differences between the behaviour of concentrated and dilute compounds is seen in the resistivity.

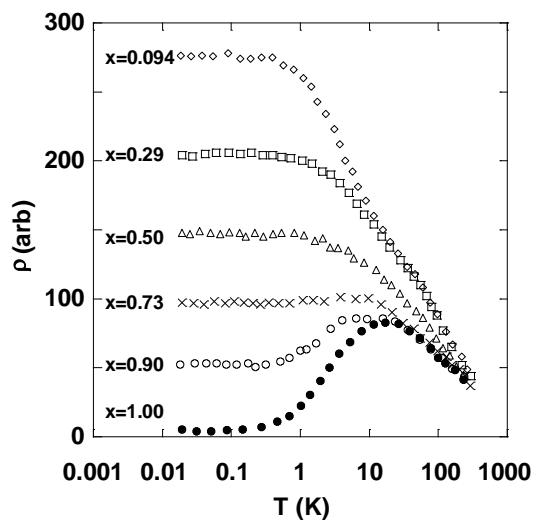


Fig 2.8 : Typical resistivity verses temperature for a heavy fermion or valence fluctuation compound for different concentrations of the Kondo ion x .

In concentrated compounds, as the temperature is lowered below another characteristic temperature $T_0 < T_K$, coherence can arise between the individual Kondo hybridised rare earth lattice sites. In this region, the magnetic moments of the rare earth ions either vanish due to complete spin compensation or they form a periodic magnetic structure. In both cases, the elastic scattering of the conduction electrons is substantially removed. Below the coherence temperature T_0 , many properties of the compound can be described by the Fermi liquid theory. This theory successfully predicts the quadratic temperature dependence of the resistivity which is

observed in many concentrated compounds below T_0 . A gradual progression between dilute and concentrated resistivity behaviour is shown in figure 2.8 [20].

2.2.4.2 Heavy fermion superconductivity.

Some concentrated heavy fermion compounds become superconducting. Initially this may seem unlikely, as small concentrations of ‘Kondo’ rare earth ions added to a ‘non-Kondo’ rare earth superconductor can suppress the formation of the superconducting pairs and drastically reduce the transition temperature as compared with the non-doped compound (see § 2.1.4.2). However, in many superconducting heavy fermion compounds, the jump in the specific heat on entering the superconducting state corresponds to the enhanced effective mass. This implies that the superconducting pairs are formed by the quasi-particles. The nature of the quasi-particle attraction is still unclear. Some theories rely on conventional electron-phonon coupling while others consider that the pairing is due to quasi-particle - quasi-particle interactions analogous to those responsible for pairing in superfluid ^3He [23]. One reason for the adoption of the latter approach is that Fermi liquid theory is used to describe both the properties of superfluid ^3He and the non-superconducting behaviour of heavy fermion compounds (see § 2.2.2).

2.2.5 Inelastic neutron scattering experiments on dilute and concentrated compounds.

The relationships between the partial differential cross section for the magnetic scattering of neutrons, the magnetic correlation function and imaginary part of the magnetic susceptibility are given in § 3.2.4.3. The following discussion assumes that the instrumental resolution function has been deconvolved. For non-interacting rare earth ions, without any interaction with the conduction electrons, the imaginary part of the magnetic susceptibility consists of a series of delta functions

$$\chi(\omega) = \sum_i \delta(\omega - \Delta_i), \quad \text{Eq 2.32}$$

where Δ_i is the energy of the i^{th} C.E.F. level. In the case of paramagnetic rare earth ions, interacting with the conduction electrons via a direct exchange (without heavy fermion or valence fluctuation hybridisation), the resulting relaxation pathways lead to a broadening of these delta peaks. The main contribution arises from the spin-spin interactions, and this leads to a Korringa-like Lorentzian linewidth $\Gamma(T)$ associated with each of the peaks

$$\Gamma(T) \propto [(g-1)jg_c(0)]^2 k_B T. \quad \text{Eq 2.33}$$

The width of the zero-energy transfer peak is governed solely by this broadening and goes to zero as $T \rightarrow 0$. The inelastic peak widths have additional broadening contributions arising from interactions between the C.E.F. transitions, and remain finite as the temperature goes to absolute zero. A theoretical description of the above scheme is given by the Becker-Fulde-Keller (B.F.K) theory [25]. The hybridisation of the rare earth and conduction electrons in heavy fermion and valence fluctuation compounds results in a substantial departure from the B.F.K. predictions for the low energy magnetic susceptibility. For moderate heavy fermion compounds, the Korringa-like line width is replaced by

$$\Gamma(T) \propto \Gamma_0 + bT^{1/2}, \quad \text{Eq 2.34}$$

where the residual Lorentzian width at $T = 0$, Γ_0 , gives an estimate of the energy scale of the rare earth/ conduction electron hybridisation ($\Gamma_0/2 \sim k_B T_K/\hbar$). For more heavily hybridised valence fluctuation compounds (T_K is large), the temperature dependent part of this line width is less significant than Γ_0 , resulting in a temperature independent line width up to high temperatures.

In concentrated compounds, interactions between the rare earth ions, or the onset of superconductivity, can cause departures from this simple scheme. For example, in compounds where the residual magnetic moments enter an ordered state, the quasi-elastic peak may move to finite energies and gain a q dependence in addition to that

determined by the C.E.F. selection rules [22]. In some compounds, interactions between the C.E.F. transitions and the lattice excitations introduce further relaxation pathways. In these cases, the excited peaks may be additionally broadened, their degeneracy broken, and their position in energy moved [24].

References.

- [1] D.C. Mattis, *The Theory of Magnetism*, Harper and Row (1965).
- [2] J. Jensen and A.R. Mackintosh, *Rare Earth Magnetism, Structures and Excitations*, Oxford University Press (1991).
- [3] N.W. Ashcroft and N.D. Mermin, *Solid State Physics*, Holt-Saunders (1975).
- [4] R.M. White, *Quantum Theory of Magnetism*, Springer Verlag (1982).
- [5] M.B. Maple, *Coexistence of Superconductivity and Magnetism*, N.A.T.O. ASI Series Summer Schools (1983).
- [6] A.A. Abrikosov and L.P. Gor'kov, *Sov. Phys. JETP*, **12**, 1243 (1961).
- [7] E.M. Hartmann *et al.*, *Phys. Rev. Lett.*, **26**, 428 (1971).
- [8] B.S. Chandrasekhar, *Appl. Phys. Lett.*, **1**, 7 (1962).
- [9] L.P. Gor'kov and A.I. Rusinov, *Sov. Phys. JETP*, **19**, 922 (1964).
- [10] P.W. Anderson and H. Suhl, *Phys. Rev.*, **116**, 898 (1959).
- [11] D.E. Moncton *et al.*, *Phys. Rev. Lett.*, **45**, 2060 (1980).
- [12] U. Krey, *Int. J. Magnetism*, **3**, 65 (1972).
- [13] E.I. Blount *et al.*, *Phys. Rev. Lett.*, **42**, 1079 (1979).
- [14] W. Baltensperger and S. Strässler, *Phys. Cond. Materie*, **1**, 20 (1963).
- [15] P. Fulde and J. Keller, *Topics in Current Physics*, Vol. 34, Chap. 9, Springer-Verlag (1982).
- [16] A.I. Morozov, *Pis'ma Zh. Eksp. Teor. Fiz.*, **63**, 702 (1996).
- [17] P.W. Anderson. *Phys. Rev.*, **124**, 41 (1961).
- [18] B. Coqblin and J.R. Schrieffer, *Phys. Rev.*, **185**, 847 (1969).
- [19] J. Kondo. *Progr. Theoret. Phys.*, **32**, 37 (1964).
- [20] P. Fulde, *J. Phys. F: Met. Phys.*, **18**, 601 (1988)
- [21] P.A. Lee *et al.*, *Comments Cond. Mat. Phys.*, **12** No. 3, 99 (1986).

-
- [22] M. Loewenhaupt and K.H. Fischer, *Handbook of Magnetic Materials*, Vol. 7, Elsevier (1993).
- [23] M. Tinkham, *Introduction to Superconductivity*, McGraw Hill (1996).
- [24] P.Fulde and M. Loewenhaupt, *Advances in Physics*, **34**, Vol. 5, 589 (1986).
- [25] K.W. Becker *et al.*, *Z. Phys. B*, **28**, 9 (1977).

CHAPTER 3

NEUTRON SCATTERING

This chapter describes the theory of neutron scattering. The first two sections introduce the basic concepts and experimental procedures. This is followed by detailed descriptions of the specific experimental techniques used in this thesis.

3.1 Introduction.

Neutron scattering is an experimental technique used in a wide range of scientific subjects to study the nuclear and magnetic structure and excitations of materials. There are many different types of neutron scattering experiment, but all of them depend on the same general principle:

A beam of neutrons is directed at a sample of the material to be studied. These neutrons are scattered by the sample. The neutrons can be produced with wavelengths that are comparable to the interatomic spacing in materials, and with energies that are comparable to the separation of their energy levels. Therefore, analysis of interference effects between the scattered neutrons gives information concerning the structure of the sample, and analysis of the energies of the neutrons gives information concerning the nature and spacing of the energy levels of the sample.

3.2 General neutron scattering.

3.2.1 The production of neutrons.

The neutron scattering experiments in this thesis have been conducted at the Institut Laue Langevin (I.L.L.) in Grenoble, France, and at the ISIS facility of the Rutherford Appleton Laboratory in Didcot, U.K. The method of producing neutrons at these two establishments is different.

The I.L.L. operates a 58 MW enriched uranium nuclear reactor. The neutrons produced within the fuel element have an average wavelength of the order of 10^{-4} Å, which corresponds to an energy of several MeV. Therefore, to be of use in scattering experiments, these neutrons have to be slowed down or moderated. This is done by a tank of heavy water that surrounds the fuel element. In this tank, the fast neutrons are slowed down by repeated collisions with the D₂O molecules. The wavelength distribution of the neutrons that emerge is dependent on the temperature of the tank. The temperature of the tank at the I.L.L. is 300 K, which corresponds to a neutron wavelength range of 1 Å to 3 Å. Neutrons with these wavelengths are called thermal neutrons, and are suitable for use in many types of scattering experiment. However, certain experiments require longer or shorter wavelengths, and these are produced using different moderators. A liquid deuterium moderator at a temperature of 25 K is used to produce neutrons with wavelengths in the range 3 Å to 30 Å, which are referred to as cold neutrons. Neutrons with wavelengths below 1 Å are called hot neutrons, and are produced using a graphite moderator at a temperature of 2400 K [1].

At ISIS, neutrons are produced by bombarding a depleted tantalum target with highly energetic protons from a particle accelerator. Each proton produces many neutrons when it hits the target nuclei. These neutrons also have too much energy to be used in scattering experiments and have to be moderated. Different final wavelength ranges are obtained using water (316 K), liquid methane (100 K), and liquid hydrogen (20 K) moderators. In contrast to the I.L.L., the neutrons at ISIS are produced in pulses at a frequency of 50 Hz, which allows certain types of experiment to be performed more easily [2].

3.2.2 Interaction of the neutron with matter.

A free neutron interacts with an atom in two ways: with the nucleus via the strong nuclear force, and with the electrons via the electromagnetic force. The neutron does not have a charge and is therefore able to penetrate into the interior of a sample without being scattered by the coulomb interaction with the atoms. Therefore, it can be used to study the bulk properties of the sample.

3.2.2.1 The strong nuclear force interaction.

Neutrons are hadrons, and therefore interact with the nuclei of atoms via the strong nuclear force. The potential between a neutron and the nucleus of an atom can be written as

$$V(\underline{r}) = \frac{2\pi \hbar^2}{m} b \delta(\underline{r}) , \quad \text{Eq 3.1}$$

where m is the mass of the neutron. This potential is called the Fermi pseudopotential, and is very short range ($\sim 10^{-14}$ m to 10^{-15} m), hence the definition in terms of a delta function. The constant b is called the scattering length. It is a measure of the strength of the interaction, and is defined as

$$b = A + B \underline{\sigma} \cdot \underline{i} , \quad \text{Eq 3.2}$$

where $(1/2)\underline{\sigma}$ is the spin of the neutron, \underline{i} is the spin of the nucleus, and A and B are constants. In general, the scattering length is complex; the imaginary part represents absorption of the neutron by the nucleus; the real part may be positive or negative, depending on the energy of the neutron and the type of nucleus, and represents scattering of the neutron. For the majority of nuclei, the imaginary component is considerably smaller than the real component; in this case, the real part is assumed to be independent of the energy of the neutron while the imaginary part is considered to be a function of the neutron energy. For a small number of nuclei, neutron absorption corresponds to the formation of a compound nucleus close to an excited state; in this case, the imaginary component of the scattering length may be large, and both the real and imaginary components are considered to be dependent on the incident neutron energy [3].

3.2.2.2 The electromagnetic force interaction.

Neutrons have a spin of $1/2$, and an associated magnetic moment. Therefore, they also interact with the magnetic moment of the unpaired electrons in atoms via the electromagnetic force. The potential between a neutron with Pauli spin operator $\underline{\sigma}$, and an electron with spin \underline{s} and linear momentum \underline{p} is

$$V(\underline{r}) = -\frac{\mu_0}{4\pi} \gamma \mu_N 2\mu_B \underline{\sigma} \cdot \left(\underline{\nabla} \times \left(\frac{\underline{s} \times \hat{r}}{r^2} \right) + \frac{1}{\hbar} \frac{\underline{p} \times \hat{r}}{r^2} \right). \quad \text{Eq 3.3}$$

The two terms on the right hand side of the above equation are referred to as the spin and orbital contributions respectively. It should be noted that the potential is long range, and both terms correspond to non central forces [3].

3.2.3 The detection of neutrons.

There are several different types of detector used in neutron scattering experiments. One of the most common is the ^3He gas detector. It consists of a stainless steel tube containing ^3He gas under pressure. A thin tungsten wire, charged to a high voltage, runs down the centre of the tube. The detection process starts with the absorption of a neutron by a ^3He nucleus



The high energy ions that are produced cause further ionisation of ^3He atoms, and this triggers a cascade discharge to the tungsten wire. The voltage of this discharge is small, and it must therefore be amplified before it is transferred to the detection electronics [4].

3.2.4 A general neutron scattering experiment.

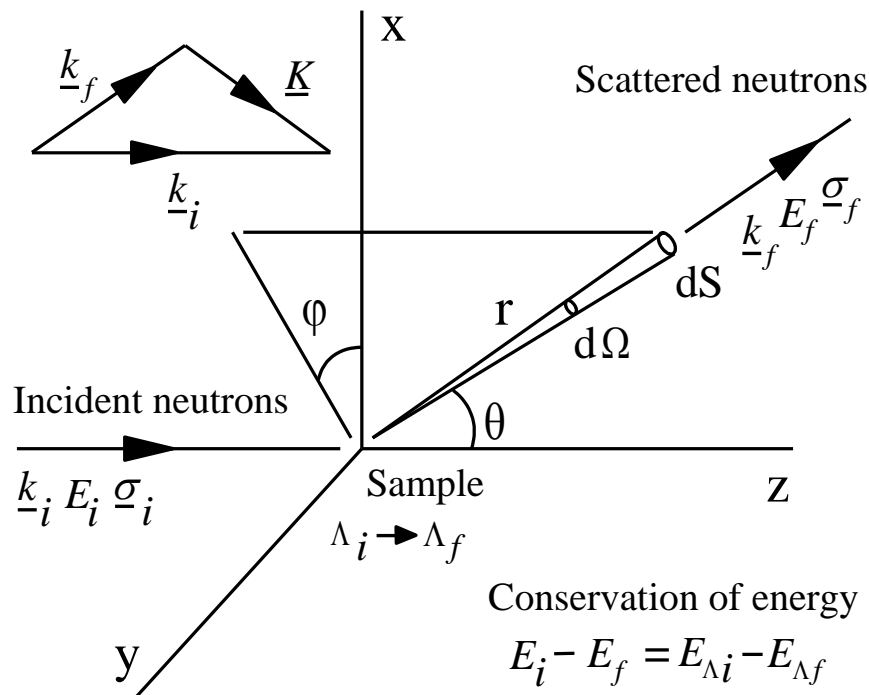


Fig 3.1 : Geometry of a general neutron scattering experiment.

A neutron in a state with wavevector \underline{k}_i , energy E_i and spin state σ_i is directed onto a sample of the material to be investigated. The sample is at a temperature T , and has a finite probability of being in one of a range of states $\{\Lambda_i\}$. The probability P_{Λ_i} that the sample is in a state Λ_i is proportional to the product of the thermodynamic occupation factor and the degeneracy for that state.

$$P_{\Lambda_i} \propto \exp\left(-\frac{E_{\Lambda_i}}{k_B T}\right) \times g(\Lambda_i) \quad \text{Eq 3.4}$$

Let us assume that the sample is in a state Λ_i . After the neutron enters the sample, it will interact with the atoms via the processes described in § 3.2.2. As a consequence of these interactions, the neutron will be scattered into a state with wavevector \underline{k}_f , energy E_f and spin state σ_f . If $E_i = E_f$ (or $|\underline{k}_i| = |\underline{k}_f|$), then the scattering is

elastic and the sample remains in the state Λ_i . If $E_i \neq E_f$ (or $|\underline{k}_i| \neq |\underline{k}_f|$), then the scattering is inelastic and the sample will change to a state Λ_f , such that the law of conservation of energy, $E_i - E_f = E_{\Lambda_i} - E_{\Lambda_f}$, is satisfied. The process whereby the sample goes from a state Λ_i to a state Λ_f is called an excitation. In a neutron scattering experiment, many neutrons are scattered in this way, and they will, in general, all have different values for \underline{k}_f , E_f and σ_f .

A number of quantities are defined to describe the scattering. The flux Φ of neutrons in the incident beam is defined as

$$\Phi = \text{number of neutrons per second, per unit normal area.} \quad \text{Eq 3.5}$$

The total scattering cross section of the sample is defined as

$$\sigma = \frac{\text{total number of neutrons scattered per second.}}{\Phi}. \quad \text{Eq 3.6}$$

The differential cross section of the sample is defined as

$$\frac{d\sigma}{d\Omega} = \frac{\text{number of neutrons scattered per second, into solid angle } d\Omega, \text{ in the direction } \theta, \varphi.}{\Phi d\Omega}. \quad \text{Eq 3.7}$$

The partial differential cross section of the sample is defined as

$$\frac{d^2\sigma}{d\Omega dE_f} = \frac{\text{number of neutrons scattered per second, into solid angle } d\Omega, \text{ in the direction } \theta, \varphi, \text{ with final energy between } E_f \text{ and } E_f + dE_f.}{\Phi d\Omega dE_f}. \quad \text{Eq 3.8}$$

For an arbitrary interaction potential V , the partial differential cross section for the process where neutrons are scattered from a state $(\underline{k}_i, E_i, \sigma_i)$ to a state $(\underline{k}_f, E_f, \sigma_f)$, and the sample changes from a state Λ_i to a state Λ_f , is given by

$$\left(\frac{d^2 \sigma_V}{d\Omega dE_f} \right)_{k_i E_i \sigma_i \Lambda_i}^{k_f E_f \sigma_f \Lambda_f} = \frac{k_f}{k_i} \left| \left\langle \sigma_f \underline{k}_f \Lambda_f | V | \sigma_i \underline{k}_i \Lambda_i \right\rangle \right|^2 \delta(E_i - E_f + E_{\Lambda_i} - E_{\Lambda_f}),$$

Eq 3.9

where the delta function represents the conservation of energy in the scattering process. There may be other transitions within the sample that scatter neutrons into a state $(\underline{k}_f, E_f, \sigma_f)$, and this equation must be summed over Λ_i and Λ_f in order to include these

$$\left(\frac{d^2 \sigma_V}{d\Omega dE_f} \right)_{k_i E_i \sigma_i}^{k_f E_f \sigma_f} = \frac{k_f}{k_i} \sum_{\Lambda_i \Lambda_f} P_{\Lambda_i} \left| \left\langle \sigma_f \underline{k}_f \Lambda_f | V | \sigma_i \underline{k}_i \Lambda_i \right\rangle \right|^2 \delta(E_i - E_f + E_{\Lambda_i} - E_{\Lambda_f}).$$

Eq 3.10

In the case of the scattering of neutrons from an arbitrary distribution of N nuclei via the strong nuclear force, the above equation reduces to

$$\left(\frac{d^2 \sigma_N}{d\Omega dE_f} \right)_{k_i E_i \sigma_i}^{k_f E_f \sigma_f} = \frac{k_f}{k_i} \sum_{\Lambda_i \Lambda_f} P_{\Lambda_i} \left| \left\langle \sigma_f \Lambda_f \left| \sum_{n=1}^N b_n \exp(i\underline{K} \cdot \underline{n}) \right| \sigma_i \Lambda_i \right\rangle \right|^2 \delta(\hbar\omega + E_{\Lambda_i} - E_{\Lambda_f}),$$

Eq 3.11

where the difference between the initial and final wavevector and energy of the neutron is $\underline{K} = \underline{k}_i - \underline{k}_f$ and $\hbar\omega = E_i - E_f$ respectively. The position of the n^{th} nucleus is \underline{n} , and its scattering length is b_n . This equation gives a connection between $(\underline{K}, \omega, \sigma_i, \sigma_f)$ and the nuclear structure and excitations of the sample. This connection is not obvious as the equation is written in a very general form. Its use becomes more transparent when it is applied to a specific type of neutron scattering experiment and sample [5].

In the case of the scattering of neutrons from an arbitrary distribution of M electrons via the electromagnetic force, equation 3.10 becomes

$$\left(\frac{d^2 \sigma_M}{d\Omega dE_f} \right)_{k_i E_i \sigma_i}^{k_f E_f \sigma_f} = \left(\frac{m}{2\pi \hbar^2} \right)^2 (2\gamma \mu_N \mu_B)^2 (4\pi)^2 \frac{k_f}{k_i} \sum_{\Lambda_i \Lambda_f} P_{\Lambda_i} \times$$

$$\left\langle \sigma_i \Lambda_i \left| \left(\underline{\sigma} \cdot \underline{Q}_p \right)^+ \right| \sigma_f \Lambda_f \right\rangle \left\langle \sigma_f \Lambda_f \left| \left(\underline{\sigma} \cdot \underline{Q}_p \right) \right| \sigma_i \Lambda_i \right\rangle \delta(\hbar\omega + E_{\Lambda_i} - E_{\Lambda_f}),$$

Eq 3.12

where

$$\underline{Q}_p = \sum_{m=1}^M \exp(i\underline{K} \cdot \underline{m}) \left\{ \hat{\underline{K}} \times (\underline{s}_m \times \hat{\underline{K}}) + \frac{i}{\hbar |\underline{K}|} (\underline{p}_m \times \hat{\underline{K}}) \right\}.$$

The position, spin and linear momentum of the m^{th} electron are \underline{m} , \underline{s}_m and \underline{p}_m respectively. This equation gives a connection between $(\underline{K}, \omega, \sigma_i, \sigma_f)$ and the magnetic structure and excitations of the sample. As with equation 3.11, the use of this equation becomes more clear when it is applied to a specific type of neutron scattering experiment and sample [6].

If the values of \underline{K} , ω , σ_i and σ_f are measured for a large number of neutrons, then the function $d^2 \sigma_N / d\Omega dE_f(\underline{K}, \omega, \sigma_i, \sigma_f)$ can be experimentally determined. It can then be compared with equation 3.11 (applied to the specific type of experiment and sample) to give information concerning the nuclear structure and excitations of the sample. The function $d^2 \sigma_M / d\Omega dE_f(\underline{K}, \omega, \sigma_i, \sigma_f)$ can be determined in the same way, and compared with equation 3.12 (again, appropriately applied) to give information concerning the magnetic structure and excitations of the sample.

To map out the above functions for all useful values of \underline{K} , ω , σ_i and σ_f would take a very long time. In practice, in any one neutron scattering experiment, the above functions are only measured for small regions of $(\underline{K}, \omega, \sigma_i, \sigma_f)$ space. The region

of this space that is measured defines the type of neutron scattering experiment. Most of the different types of experiment fall into four groups: unpolarised elastic, unpolarised inelastic, polarised elastic, and polarised inelastic neutron scattering.

3.2.4.1 Unpolarised elastic neutron scattering.

In unpolarised elastic neutron scattering experiments, the value of σ_i for each neutron is random and the value of σ_f is not measured. In most experiments, only \underline{k}_i and the direction of \underline{k}_f are measured. As $|\underline{k}_f|$ (or ω) is not measured, there is no way to determine if the neutron has been scattered elastically or inelastically. This does not present a large problem when the number of inelastically scattered neutrons is much less than the number of elastically scattered neutrons as only a small error is introduced if it is assumed that all the neutrons have been scattered elastically. However, in some experiments, the number of inelastically scattered neutrons is large, and theoretical corrections must be made; if this is not possible, an experiment can be performed where $|\underline{k}_f|$ is measured and the inelastically scattered neutrons subtracted. These types of experiments are used to give information concerning the structure of the sample and are often referred to as diffraction experiments. The experiments described in § 5.1, 5.3 and 5.4 use this technique [3].

3.2.4.2 Unpolarised inelastic neutron scattering.

In unpolarised inelastic neutron scattering experiments, again, the value of σ_i for each neutron is random and the value of σ_f is not measured. Both \underline{K} and ω are measured, and any region of (\underline{K}, ω) space may be explored. This type of experiment is designed to examine the region where $\omega \neq 0$, and therefore to study the excitations of the sample. The experiments described in chapter 6 use this technique [3].

3.2.4.3 Magnetic susceptibility and inelastic neutron scattering.

The dynamic, \underline{q} dependent, susceptibility of a material that has a magnetisation $M(\underline{q}, \underline{\omega})$ induced by a magnetic field $H(\underline{q}, \underline{\omega})$ is defined as

$$\chi(\underline{q}, \underline{\omega}) = \frac{M(\underline{q}, \underline{\omega})}{H(\underline{q}, \underline{\omega})}. \quad \text{Eq 3.13}$$

In general, the susceptibility is complex, reflecting the fact that a phase difference may exist between the induced magnetisation and the driving magnetic field.

$$\chi(\underline{q}, \underline{\omega}) = \chi'(\underline{q}, \underline{\omega}) + i\chi''(\underline{q}, \underline{\omega}). \quad \text{Eq 3.14}$$

The partial differential cross section for the magnetic scattering of neutrons, given in equation 3.12, can be rewritten in the general form

$$\frac{d^2\sigma_M}{d\Omega d\omega_f} = \frac{k_f}{k_i} \frac{1}{2\pi} \left(\frac{\gamma \mu_N e^2}{mc^2} \right)^2 S(\underline{q}, \omega), \quad \text{Eq 3.15}$$

where $S(\underline{q}, \omega)$ is the spatial and temporal Fourier transform of the magnetic correlation function. There are two theorems that are especially useful for interpreting the results of inelastic neutron scattering experiments. The fluctuation dissipation theorem relates the Fourier transformed correlation function to the imaginary part of the susceptibility

$$\chi''(\underline{q}, \omega) = \left[1 - \exp\left(-\frac{\hbar\omega}{k_B T}\right) \right] S(\underline{q}, \omega). \quad \text{Eq 3.16}$$

The factor in square brackets satisfies the principle of detailed balance which is needed to correct for the initial thermal population of states within the scattering

system. The Kramers-Kronig theorem relates the integral of the imaginary susceptibility with respect to ω to the static, \underline{q} dependent, susceptibility.

$$\chi(\underline{q}, \infty) = \frac{1}{\pi} \int_{-\infty}^{\infty} \frac{1}{\omega} \chi''(\underline{q}, \omega) d\omega. \quad \text{Eq 3.17}$$

This theorem is useful for relating the results of inelastic neutron scattering experiments to static susceptibility measurements performed using laboratory magnetometers [7].

3.2.4.4 Polarised neutron scattering.

In polarised elastic, and polarised inelastic neutron scattering experiments, σ_i and σ_f are measured, in addition to the quantities listed above for the unpolarised experiments. These experiments are only performed when the required information concerning the sample cannot be obtained using unpolarised neutrons. This is because the production and detection of polarised neutrons is complicated and the incident neutron flux is considerably reduced. The experiment described in § 5.2 uses polarised neutrons [8].

3.3 Neutron scattering techniques.

3.3.1 Determination of the nuclear structure, average crystallite radius and mosaic spread of single crystals using unpolarised elastic neutron scattering and the D9 diffractometer at the I.L.L.

3.3.1.1 Derivation of the nuclear unit cell structure factor and Bragg's law.

The partial differential cross section for the scattering of neutrons from an arbitrary distribution of nuclei via the strong nuclear force is given by equation 3.11. For a non-Bravais single crystal sample and unpolarised neutron beam, this equation reduces to

$$\left(\frac{d^2 \sigma_N}{d\Omega dE_f} \right)_{k_i E_i}^{k_f E_f} = \frac{k_f}{k_i} \frac{1}{2\pi \hbar} \sum_{l d} \sum_{l' d'} \langle b_d b_{d'} \rangle_{\text{sp, iso}} \exp(i \underline{K} \cdot (\underline{l} + \underline{d} - \underline{l}' - \underline{d}')) \times \int_{-\infty}^{+\infty} \langle \exp(-i \underline{K} \cdot \underline{u}(\underline{l}', \underline{d}', 0)) \exp(i \underline{K} \cdot \underline{u}(\underline{l}, \underline{d}, t)) \rangle \exp(-i \omega t) dt, \quad \text{Eq 3.18}$$

where t is time, \underline{l} is the position of the l^{th} unit cell and \underline{d} is the equilibrium position of the d^{th} nuclei within that unit cell.

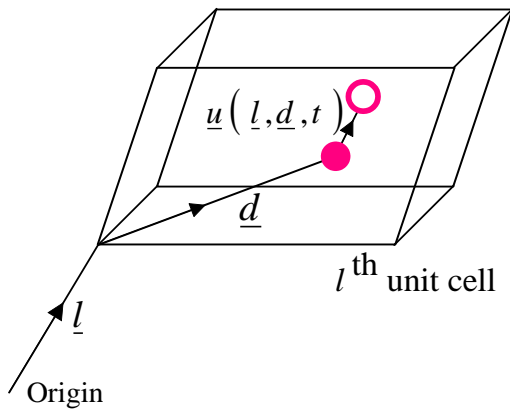


Fig 3.2 : Position vector of the d^{th} nuclei in the l^{th} unit cell.

- equilibrium position
- instantaneous position

The thermal displacement of the nucleus from its equilibrium position is given by $\underline{u}(\underline{l}, \underline{d}, t)$, and this can be expressed as a sum of the displacements due to a set of normal modes

$$\underline{u}(\underline{l}, \underline{d}, t) = \left(\frac{\hbar}{2M_d N} \right)^{1/2} \sum_{\underline{q} j} \frac{1}{\sqrt{\omega_{\underline{q} j}}} \left\{ \underline{e}_{d \underline{q} j} a_{\underline{q} j} \exp(i(\underline{q} \cdot \underline{l} - \omega_{\underline{q} j} t)) + \underline{e}_{d \underline{q} j}^* a_{\underline{q} j}^+ \exp(-i(\underline{q} \cdot \underline{l} - \omega_{\underline{q} j} t)) \right\},$$

Eq 3.19

where \underline{q} , j , $\omega_{\underline{q} j}$ and $\underline{e}_{d \underline{q} j}$ are the wavevector, polarisation index, angular frequency and polarisation vector of the mode. The mass of the d^{th} atom is given by M_d , and there are N values of \underline{q} in the first Brillouin zone. The creation and annihilation operators for the mode $\underline{q} j$ are $a_{\underline{q} j}^+$ and $a_{\underline{q} j}$ respectively. The products of the

scattering lengths in equation 3.18 are averaged over variations in nuclear spin and isotopic composition.

Equation 3.18 implicitly describes two distinct types of scattering, known as coherent and incoherent. Incoherent scattering depends on the correlation between the positions of the same nucleus at different times; therefore, it does not give rise to interference effects. The coherent scattering depends on the correlation between the positions of the same nucleus at different times, and on the correlation between the positions of different nuclei at different times. This type of scattering gives rise to interference effects, and is therefore useful for determining the nuclear structure of the crystal. The coherent partial differential cross section is

$$\left(\frac{d^2 \sigma_{N, \text{coh}}}{d\Omega dE_f} \right)_{k_i E_i}^{k_f E_f} = \frac{k_f}{k_i} \frac{1}{2\pi \hbar} \sum_{l, d} \sum_{l', d'} \langle b_d \rangle_{\text{sp, iso}} \langle b_{d'} \rangle_{\text{sp, iso}} \exp(i \underline{K} \cdot (\underline{l} + \underline{d} - \underline{l}' - \underline{d}')) \times$$

$$\int_{-\infty}^{+\infty} \langle \exp(-i \underline{K} \cdot \underline{u}(\underline{l}', \underline{d}', 0)) \exp(i \underline{K} \cdot \underline{u}(\underline{l}, \underline{d}, t)) \rangle \exp(-i \omega t) dt \quad \text{Eq 3.20}$$

The average over the scattering lengths is no longer an average over their product, but two separate averages before the product is performed. The coherent elastic differential cross section can be derived from the above equation, and is

$$\left(\frac{d\sigma_{N, \text{coh, el}}}{d\Omega} \right)_{k_i}^{k_f} = N \frac{(2\pi)^3}{v_0} \sum_{\underline{\tau}} \delta(\underline{K} - \underline{\tau}) |F_N(\underline{K})|^2, \quad \text{Eq 3.21}$$

where v_0 is the volume of the unit cell, $\underline{\tau}$ is a reciprocal lattice vector of the crystal, and the nuclear unit cell structure factor is

$$F_N(\underline{\tau}) = \sum_d \langle b_d \rangle_{\text{sp, iso}} \exp(i \underline{\tau} \cdot \underline{d}) \exp(-W_d). \quad \text{Eq 3.22}$$

The nuclear unit cell structure factor is dependent on the scattering lengths and positions of the atoms in the basis, and quantities that are dependent on the thermal motions of the atoms which correspond to a superposition of normal mode vibrations. These quantities are called the Debye-Waller factors and are given by

$$W_d = \frac{\hbar}{4M_d N} \sum_{\underline{qj}} \frac{|\underline{\tau} \cdot \underline{e}_{d\underline{qj}}|^2}{\omega_{\underline{qj}}} \langle 2n_{\underline{qj}} + 1 \rangle, \quad \text{Eq 3.23}$$

where $n_{\underline{qj}}$ is the quantum number for the mode \underline{qj} . It can be rewritten, for an orthorhombic crystal, as

$$W_d = \frac{1}{4} \left(B_{11d} ha^* ha^* + B_{22d} kb^* kb^* + B_{33d} lc^* lc^* \right), \quad \text{Eq 3.24}$$

where (ha^*, kb^*, lc^*) is the reciprocal lattice vector, and B_{11d} , B_{22d} and B_{33d} are the anisotropic temperature factors for the d^{th} atom. These give the axes lengths of an ellipsoid that corresponds to the standard deviation of the atom's distribution in space.

Equation 3.21 implies that there is scattering only in directions where the change in wavevector of the neutrons \underline{K} is equal to a reciprocal lattice vector of the crystal $\underline{\tau}$. This principle is known as Bragg's law, and is fundamental to all elastic scattering experiments on periodic structures [3].

3.3.1.2 A description of the general technique.

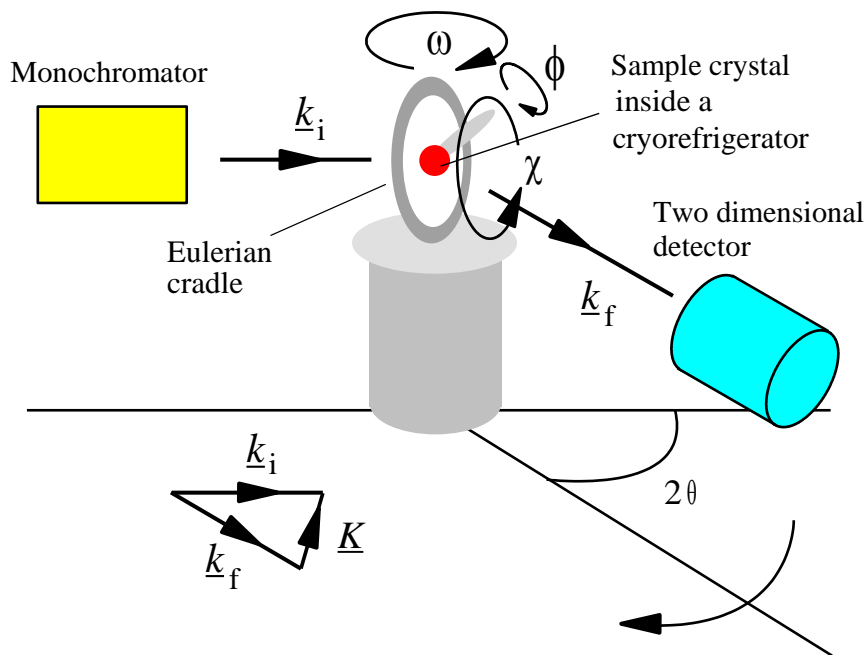


Fig 3.3 : The D9 diffractometer [9].

It is assumed that the lattice parameters of the crystal to be studied are known approximately before the following experiment is performed. This will usually have been done by performing an elastic neutron, or X-ray scattering experiment, on a powder sample of the material under investigation.

In this technique, a monochromatic neutron beam is directed at a single crystal, placed inside a cryo-refrigerator, mounted at the centre of an Eulerian cradle. An Eulerian cradle is a device with three independent axes of rotation that is used to orientate the crystal with respect to the incident neutron beam. If the orientation of the reciprocal lattice of the crystal is known with respect to the angles of the Eulerian cradle (ω , χ , ϕ), and the change in wavevector of the neutrons is known with respect to the angle of the detector 2θ , then the values for these angles needed to access any reciprocal lattice vector can be calculated. The relationship between the angles (ω , χ , ϕ) and the reciprocal lattice is expressed by a matrix, called the orientation matrix, and the values of 2θ for each reflection are calculated using Bragg's law. In practice, due to the geometry of D9, and the magnitude of the neutron wavevector

used, there are limitations on the regions of reciprocal space that may be accessed [10].

After the orientation matrix has been calculated, the angles ω , χ , ϕ and θ are adjusted to move the crystal and detector to positions where the Bragg condition is satisfied for a reciprocal lattice vector of the crystal, so that the number of neutrons scattered per unit time into the associated Bragg peak can be measured. A single crystal consists of many crystallites, all slightly misaligned with respect to one another. This misalignment is called the mosaic spread of the crystal, and causes the delta function in equation 3.21 to be spread out into a peak of finite width (see § 5.1.4.2). Therefore, in order to include the scattering from all of the crystallites in the mosaic, a scan is performed where the value of ω is stepped through a series of positions either side of the Bragg peak centre. At each of these positions, the detector is left to count the number of neutrons scattered for a fixed period of time. Due to the finite resolution of the D9 diffractometer, the scattered neutrons for a particular step in the scan will have a spread in their final trajectories. In order to count all of these neutrons, the D9 detector has a finite aperture. The number of neutrons scattered per unit time as a function of ω is called the rocking curve for the particular reciprocal lattice vector. A two dimensional detector is used on D9 to improve the accuracy of centering on the Bragg peaks [9].

The integrated area under the rocking curve gives the intensity of the Bragg peak, which is the total number of neutrons scattered per unit time into the Bragg peak. This can be calculated from equation 3.21, and is given by

$$I(\underline{\tau}) = \frac{V}{v_0^2} \Phi \frac{\lambda^3}{\sin 2\theta} |F_N(\underline{\tau})|^2, \quad \text{Eq 3.25}$$

where λ is the wavelength of the neutrons, V is the sample volume and Φ is the incident neutron flux. In a typical experiment, $I(\underline{\tau})$ is measured for a large number of Bragg reflections. This set of Bragg reflections is usually chosen so that a large

unique region of reciprocal space is represented. Using the above equation, the corresponding set of $\{|F_N(\underline{\tau})|^2\}$ are calculated [10].

The set of $\{|F_N(\underline{\tau})|^2\}$ are used to determine the positions, occupancies and thermal parameters of the atoms in the unit cell, and the average crystallite radius and mosaic spread of the crystal, as described in § 5.1.5.1.

The values of ω , χ , and θ at the centre of each Bragg peak are also recorded. These values are used to calculate the real space unit cell lattice vectors more accurately, as described in § 5.1.5.2.

3.3.2 Determination of the magnetisation density in single crystal samples using polarised elastic neutron scattering and the D3 diffractometer at the I.L.L.

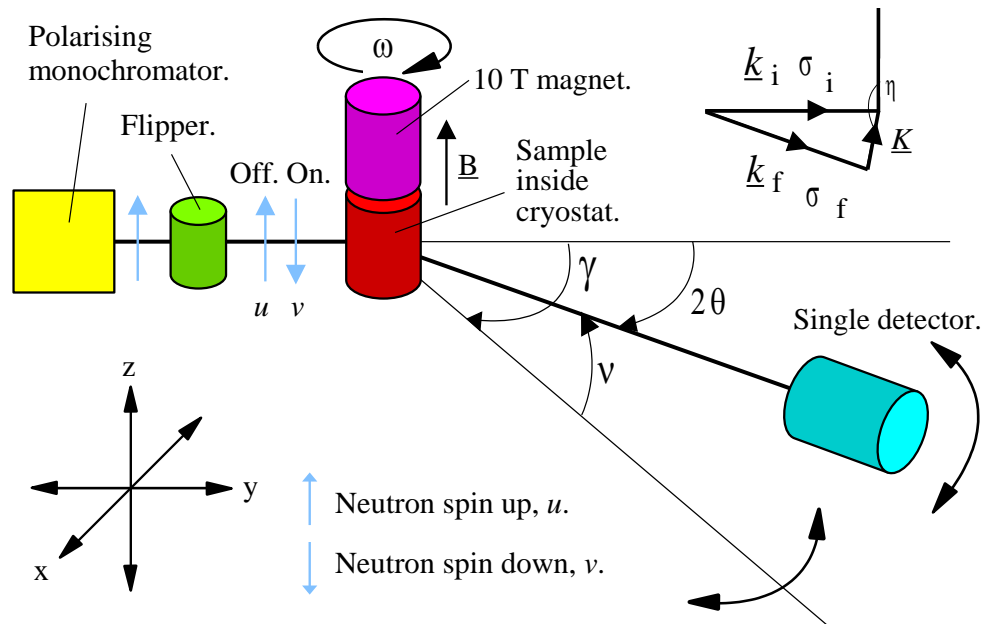


Fig 3.4 : The D3 diffractometer [9].

The partial differential cross section for the scattering of neutrons from an arbitrary distribution of nuclei via the strong nuclear force and an arbitrary distribution of electrons via the electromagnetic force is given by the sum of equations 3.11 and 3.12.

$$\left(\frac{d^2 \sigma_{NM}}{d\Omega dE_f} \right)_{k_i E_i \sigma_i}^{k_f E_f \sigma_f} = \frac{k_f}{k_i} \sum_{\Lambda_i \Lambda_f} P_{\Lambda_i} \left\langle \sigma_f \Lambda_f \left| \sum_n \left\{ (A_n + B_n \underline{\sigma} \cdot \underline{I}_n) \exp(i \underline{K} \cdot \underline{n}) \right\} - \gamma r_0 \underline{\sigma} \cdot \underline{Q}_p \right| \sigma_i \Lambda_i \right\rangle^2 \times$$

$$\delta(\hbar\omega + E_{\Lambda_i} - E_{\Lambda_f}), \quad \text{Eq 3.26}$$

where $r_0 = \mu_0 e^2 / 4\pi m_e$ is the classical radius of the electron.

For a non-Bravais single crystal sample with localised electrons, the above equation becomes, in the dipole approximation,

$$\left(\frac{d^2 \sigma_{NM}}{d\Omega dE_f} \right)_{k_i E_i \sigma_i}^{k_f E_f \sigma_f} = \frac{k_f}{k_i} \sum_{\Lambda_i \Lambda_f} P_{\Lambda_i} \left\langle \Lambda_f \left| \sum_l \exp(i \underline{K} \cdot \underline{l}) \left\langle \sigma_f \left| f_N(\underline{K}) - \gamma r_0 \underline{\sigma} \cdot \underline{f}_M(\underline{K}) \right| \sigma_i \right\rangle \right| \Lambda_i \right\rangle^2 \times$$

$$\delta(\hbar\omega + E_{\Lambda_i} - E_{\Lambda_f}), \quad \text{Eq 3.27}$$

where

$$f_N(\underline{K}) = \sum_d \langle A_d + B_d \underline{\sigma} \cdot \underline{I}_d \rangle_{\text{sp, iso}} \exp(i \underline{K} \cdot \underline{d}), \quad \text{Eq 3.28}$$

$$\underline{f}_M(\underline{K}) = \hat{\underline{K}} \times \left[\sum_d f_d(\underline{K}) \exp(i \underline{K} \cdot \underline{d}) \langle \hat{\underline{\varepsilon}}_d \rangle \times \hat{\underline{K}} \right], \quad \text{Eq 3.29}$$

and the positions of the nuclei are defined as shown in figure 3.2, [3]. The term $f_d(\underline{K})$ in the above equation describes the distribution of the electrons orbiting the d^{th} nuclei, and $\langle \hat{\underline{\varepsilon}}_d \rangle$ is a unit vector parallel to the average direction of the electrons angular momentum operator. For many atoms, this distribution can be described by

$$f_d(\underline{K}) = \sum_l \sum_{m=-l}^l a_{dlm} F_{dlm}(\underline{K}), \quad \text{Eq 3.30}$$

where the sum is over wavefunctions with azimuthal and magnetic quantum numbers given by l and m , and a_{dlm} is the magnitude of the angular momentum operator associated with the unpaired electrons in the lm^{th} wavefunction. The normalised form factor for this wavefunction is

$$F_{dlm}(\underline{K}) = Y(l, m) \langle j_l(\underline{K}) \rangle_d, \quad \text{Eq 3.31}$$

where $Y(l, m)$ is the spherical harmonic, and $\langle j_l(\underline{K}) \rangle_d$ is the radial integral. The values of the radial integrals for a particular ion, and value of l , are calculated using Hartree-Fock theory (transition metal elements) and Dirac-Fock theory (rare earth and actinide elements) and are given in crystallography tables [11].

In this technique, a monochromatic polarised neutron beam is directed at a single crystal placed inside a cryostat. The crystal is orientated such that the scattering plane to be accessed is near the horizontal (in the xy plane in figure 3.4). The polarisation of the neutron beam can be such that the neutron spins are aligned parallel (neutron spin up, u), or antiparallel (neutron spin down, v) to the positive z direction. The polarising monochromator produces a neutron beam in the spin up state. A spin flipper, when set to on, is used to give a neutron beam in the spin down state. In this geometry, equation 3.27 can be spilt into four terms corresponding to the four spin state transitions ($u \rightarrow u$), ($v \rightarrow v$), ($u \rightarrow v$) and ($v \rightarrow u$). For each of these terms, the spin matrix elements are given by

$$\begin{aligned} \langle u | f_N(\underline{K}) - \gamma r_0 \underline{\sigma} \cdot \underline{f}_M(\underline{K}) | u \rangle &= \sum_d \langle A_d + B_d I_d^Z \rangle_{\text{sp, iso}} \exp(i\underline{K} \cdot \underline{d}) - \gamma r_0 f_M^Z(\underline{K}), \\ \langle v | f_N(\underline{K}) - \gamma r_0 \underline{\sigma} \cdot \underline{f}_M(\underline{K}) | v \rangle &= \sum_d \langle A_d - B_d I_d^Z \rangle_{\text{sp, iso}} \exp(i\underline{K} \cdot \underline{d}) + \gamma r_0 f_M^Z(\underline{K}), \\ \langle u | f_N(\underline{K}) - \gamma r_0 \underline{\sigma} \cdot \underline{f}_M(\underline{K}) | v \rangle &= \sum_d \langle B_d (I_d^X - iI_d^Y) \rangle_{\text{sp, iso}} \exp(i\underline{K} \cdot \underline{d}) - \gamma r_0 (f_M^X(\underline{K}) - if_M^Y(\underline{K})), \\ \langle v | f_N(\underline{K}) - \gamma r_0 \underline{\sigma} \cdot \underline{f}_M(\underline{K}) | u \rangle &= \sum_d \langle B_d (I_d^X + iI_d^Y) \rangle_{\text{sp, iso}} \exp(i\underline{K} \cdot \underline{d}) - \gamma r_0 (f_M^X(\underline{K}) + if_M^Y(\underline{K})). \end{aligned}$$

$$\text{Eq 3.32}$$

The first two terms are referred to as non-spin-flip as the spin state of the neutron is not changed on scattering; the second two terms are referred to as spin-flip. The spins of the nuclei in the crystal are randomly orientated at all temperatures above a few mK. Therefore, an average over their values gives

$$\langle I_d^X \rangle_{\text{sp}} = 0, \quad \langle I_d^Y \rangle_{\text{sp}} = 0 \quad \text{and} \quad \langle I_d^Z \rangle_{\text{sp}} = 0. \quad \text{Eq 3.33}$$

If the above equations are substituted into the spin matrix elements, they become

$$\begin{aligned} \langle u | f_N(\underline{K}) - \gamma r_0 \underline{\sigma} \cdot \underline{f}_M(\underline{K}) | u \rangle &= \sum_d \langle A_d \rangle_{\text{iso}} \exp(i\underline{K} \cdot \underline{d}) - \gamma r_0 f_M^Z(\underline{K}), \\ \langle v | f_N(\underline{K}) - \gamma r_0 \underline{\sigma} \cdot \underline{f}_M(\underline{K}) | v \rangle &= \sum_d \langle A_d \rangle_{\text{iso}} \exp(i\underline{K} \cdot \underline{d}) + \gamma r_0 f_M^Z(\underline{K}), \\ \langle u | f_N(\underline{K}) - \gamma r_0 \underline{\sigma} \cdot \underline{f}_M(\underline{K}) | v \rangle &= -\gamma r_0 (f_M^X(\underline{K}) - if_M^Y(\underline{K})) \quad \text{and} \\ \langle v | f_N(\underline{K}) - \gamma r_0 \underline{\sigma} \cdot \underline{f}_M(\underline{K}) | u \rangle &= -\gamma r_0 (f_M^X(\underline{K}) + if_M^Y(\underline{K})). \end{aligned} \quad \text{Eq 3.34}$$

If a magnetic field is applied to the crystal, strong enough to align the magnetic moments of the unpaired electrons along the negative z direction, and only scattering within the xy plane is considered, we have

$$f_M^Z(\underline{K}) = \sum_d f_d(\underline{K}) \exp(i\underline{K} \cdot \underline{d}), \quad f_M^X(\underline{K}) = 0 \quad \text{and} \quad f_M^Y(\underline{K}) = 0. \quad \text{Eq 3.35}$$

Under these conditions, the spin matrix elements are

$$\begin{aligned} \langle u | f_N(\underline{K}) - \gamma r_0 \underline{\sigma} \cdot \underline{f}_M(\underline{K}) | u \rangle &= \sum_d \langle A_d \rangle_{\text{iso}} \exp(i\underline{K} \cdot \underline{d}) + \gamma r_0 f_M^Z(\underline{K}), \\ \langle v | f_N(\underline{K}) - \gamma r_0 \underline{\sigma} \cdot \underline{f}_M(\underline{K}) | v \rangle &= \sum_d \langle A_d \rangle_{\text{iso}} \exp(i\underline{K} \cdot \underline{d}) - \gamma r_0 f_M^Z(\underline{K}), \\ \langle u | f_N(\underline{K}) - \gamma r_0 \underline{\sigma} \cdot \underline{f}_M(\underline{K}) | v \rangle &= 0 \quad \text{and} \\ \langle v | f_N(\underline{K}) - \gamma r_0 \underline{\sigma} \cdot \underline{f}_M(\underline{K}) | u \rangle &= 0, \end{aligned} \tag{Eq 3.36}$$

and there is no spin-flip scattering. The above equations can be substituted into equation 3.27 to give the partial differential cross sections for the two non-spin-flip scattering processes. The corresponding coherent elastic differential cross sections can then be derived. These are given by

$$\left(\frac{d\sigma_{NM,\text{coh,el}}}{d\Omega} \right)_{k_i u}^{k_f u} = N \frac{(2\pi)^3}{v_0} \sum_{\underline{\tau}} \delta(\underline{K} - \underline{\tau}) |F_N(\underline{K}) + \gamma r_0 F_M(\underline{K})|^2 \quad \text{and} \tag{Eq 3.37}$$

$$\left(\frac{d\sigma_{NM,\text{coh,el}}}{d\Omega} \right)_{k_i v}^{k_f v} = N \frac{(2\pi)^3}{v_0} \sum_{\underline{\tau}} \delta(\underline{K} - \underline{\tau}) |F_N(\underline{K}) - \gamma r_0 F_M(\underline{K})|^2, \tag{Eq 3.38}$$

where

$$F_N(\underline{K}) = \sum_d \langle A_d \rangle_{\text{iso}} \exp(i\underline{K} \cdot \underline{d}) \exp(-W_d) \tag{Eq 3.39}$$

is the nuclear unit cell structure factor, introduced in § 3.3.11, and

$$F_M(\underline{K}) = \sum_d f_d(\underline{K}) \exp(i\underline{K} \cdot \underline{d}) \exp(-W_d) \tag{Eq 3.40}$$

is the magnetic unit cell structure factor [6].

After the crystal has been mounted and aligned, the crystal and detector are moved to positions where the Bragg condition is satisfied for a reciprocal lattice vector. In principle, this is done in the same way as in the D9 experiment; however, the details are different. The D3 diffractometer is not fitted with an Eulerian cradle and the crystal, once mounted, can only be rotated about the z axis (ω). The detector can move through a large angle in the xy plane (γ) and can be rotated by a smaller angle out of this plane ($-25 < \nu < +5$), (see figure 3.4). This lack of orientational flexibility means that only a limited region of reciprocal space is accessible for each crystal mounting and during an experiment the crystal will have to be remounted in order to gain access to a larger region (the angle between the incident and diffracted beam is 2θ).

After the Bragg peak has been located with respect to the detector angle 2θ , a scan is performed to find the position of its maximum with respect to ω . Once this maximum has been located, the spin flipper is set to 'off', to give an incident neutron beam in the spin up state. The detector is left to count the number of neutrons scattered for a fixed period of time. The spin flipper is then set to 'on', to give an incident neutron beam in the spin down state. The detector is left to count for the same period of time. This flipper off / flipper on counting is also performed with the crystal and detector moved to positions either side of the Bragg peak; this is done to obtain values for the background scattering.

The ratio of the spin up to spin down scattering, at the maximum of the Bragg peak, is called the flipping ratio. As the integrated area under the Bragg peak is proportional to its maximum, the flipping ratio can be given by the ratio of equations 3.37 and 3.38,

$$R(\underline{\tau}) = \frac{\left(\frac{d\sigma_{NM,coh,el}}{d\Omega} \right)_{k_i u}^{k_f u}}{\left(\frac{d\sigma_{NM,coh,el}}{d\Omega} \right)_{k_i v}^{k_f v}} = \frac{|F_N(\underline{\tau}) + \gamma r_0 F_M(\underline{\tau})|^2}{|F_N(\underline{\tau}) - \gamma r_0 F_M(\underline{\tau})|^2}. \quad \text{Eq 3.41}$$

The flipping ratios are measured for a large number of Bragg reflections. The set of Bragg reflections is chosen carefully so that a large region of reciprocal space is represented. If the nuclear unit cell structure factors can be calculated from a theoretical model of the crystal, then a set of magnetic unit cell structure factors $\{|F_M(\underline{\tau})|\}$ can be calculated using the above equation and the method described in § 5.2.5.1.

The analysis described above assume that the electrons are localised around the positions of the nuclei. If this is not the case, a more general version of equation 3.29 is appropriate where the magnetic scattering term is not specific to any electronic model of the unit cell. This is given by

$$\underline{f}_M(\underline{K}) = \frac{1}{\mu_B} \hat{K} \times \left[\left\{ \int_{\text{unit cell}} \underline{m}(\underline{r}) \exp(i\underline{K} \cdot \underline{r}) d\underline{r} \right\} \times \hat{K} \right], \quad \text{Eq 3.42}$$

where the magnetisation density vector in the unit cell is $\underline{m}(\underline{r})$ [6].

If the above equation is used, instead of equation 3.29, in the above derivation, the relationship between the projection of the magnetisation density vector along the z direction $m(\underline{r})$ and the set of magnetic unit cell structure factors is given by

$$m(\underline{r}) = \frac{\mu_B}{v_0} \sum_{\underline{\tau}} F_M(\underline{\tau}) \exp(-i\underline{\tau} \cdot \underline{r}) \quad \text{and} \quad \text{Eq 3.43}$$

$$F_M(\underline{\tau}) = \frac{1}{\mu_B} \int_{\text{unit cell}} m(\underline{r}) \exp(i\underline{\tau} \cdot \underline{r}) d\underline{r}. \quad \text{Eq 3.44}$$

The set of $\{F_M(\underline{\tau})\}$ can be used to determine the magnetisation density or magnetic moment density associated with each atom in the unit cell using the methods described in § 5.2.5.2.

3.3.3 Determination of the crystal structure of a polycrystalline sample using unpolarised elastic neutron scattering and the D1B diffractometer at the I.L.L.

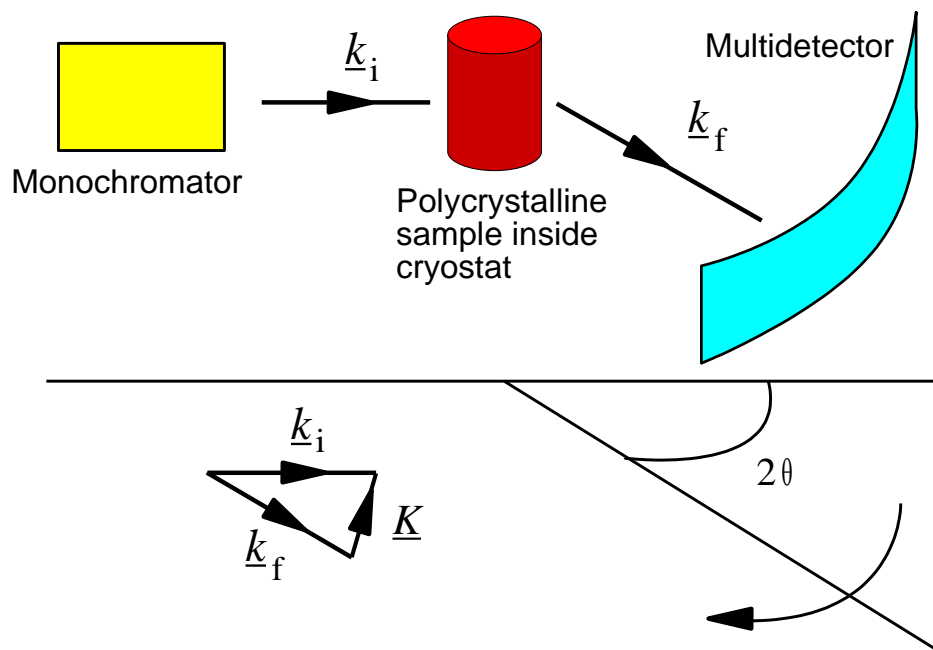


Fig 3.5 : The D1B diffractometer [9].

The derivation of the Laue equation is given in the description of the D9 experiment (§ 3.3.1). This experimental technique is similar to that of D9 in that the sample is placed in an unpolarised monochromatic beam. However, now, the Bragg condition is satisfied for all the reciprocal lattice vectors of the sample simultaneously by using a polycrystalline sample. For a particular reciprocal lattice vector, the elastically scattered neutrons emerge in a cone defined by a constant angle 2θ to the direct beam. The neutrons are collected by a large flat cone multidetector. The position in 2θ of the peaks in intensity can be used to determine the space group and lattice spacings of the crystal structure. With the use of equation 3.25 the intensity of the peaks can be used to determine the crystal basis. If more than one compound is present in a sample, the relative intensities of the Bragg reflections can be used to calculate the concentration of each of the compounds [3].

3.3.4 Magnetic inelastic neutron scattering from a polycrystalline sample using a direct geometry Time Of Flight (T.O.F.) spectrometer.

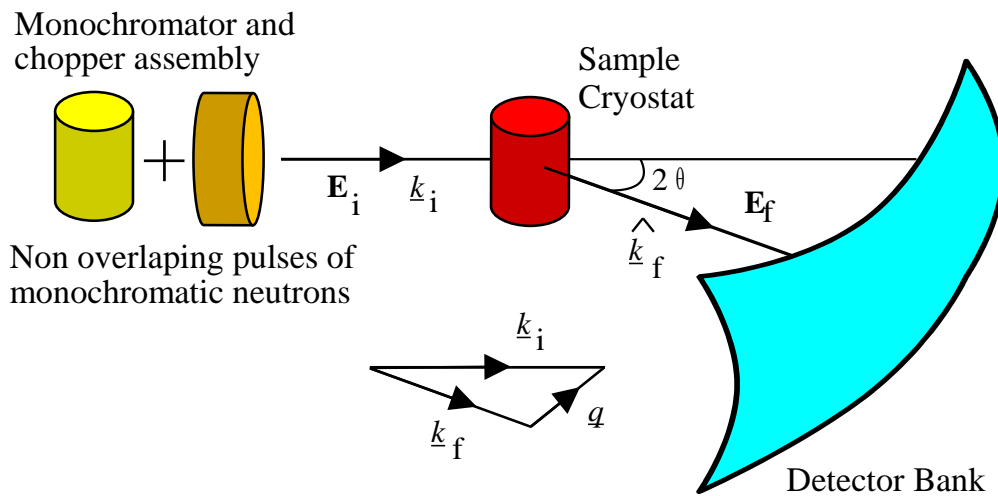


Fig 3.6 : A direct geometry time of flight spectrometer.

A polycrystalline sample is placed in a non-overlapping pulsed monochromatic neutron beam. The method of producing such a neutron beam varies depending on the type of neutron source and the particular T.O.F. spectrometer. At a spallation source, such as ISIS, the incoming neutrons are already produced in pulses. They must still be monochromated and, if the neutron energy is high enough, some pulses may have to be removed in order to ensure that they do not overlap. At a reactor source, such as the I.L.L., a continuous polychromatic neutron beam is produced. Therefore, it must be monochromated and pulsed. The exact method for monochromating and pulsing the neutrons for the instruments used in this thesis will be described in the relevant experimental sections (§ 6.1, 6.4 and 6.5).

The time that each neutron pulse hits the sample position is recorded. The neutrons are scattered into a large angle detector bank with many individual detectors at different angles relative to the incident neutron beam. The times that the scattered neutrons reach the individual detectors in the detector bank is also recorded. Therefore, the time differences can be used to calculate the final energies of the scattered neutrons. In this way both the momentum transfer $\underline{q} = \underline{k}_i - \underline{k}_f$ and energy transfer

$\omega = (\hbar/2m)(k_i^2 - k_f^2)$ into the sample can be calculated for the scattered neutrons. If the non-magnetic background scattering can be subtracted, the data obtained can be compared with the magnetic partial differential cross section given in equation 3.12, [12]. The non-magnetic background arises from nuclear scattering from the sample and spurious scattering from the instrument itself. A simple method of subtracting the former is to measure a non-magnetic sample with the same structure as the sample under investigation (for rare earth materials, this involves measuring the yttrium or lutetium compounds). An estimate of the instrument background can be made by performing measurements with just the sample holder in the beam. These techniques are explained further in the relevant experimental sections of this thesis (§ 6.1, 6.4 and 6.5).

The magnetic partial differential cross section obtained can be normalised to units of ‘mb sr⁻¹ meV⁻¹ [formula unit]⁻¹’ by measuring a vanadium sample. Vanadium has a high incoherent scattering length and a small coherent scattering length and therefore scatters isotropically and can be used for normalising for the solid angles of the individual detectors (see § 6.1).

After the above data processing has been completed, equations 3.15 and 3.16 can be used to give the imaginary part of the dynamic, \underline{q} dependent, susceptibility from the magnetic partial differential cross section. This can then be compared with theoretical models of the magnetic properties of the sample under investigation [12].

It should be noted that as a polycrystalline sample is used, the partial differential cross section measured at \underline{q} represents an average over all directions of the scattering vector in the reciprocal lattice of the sample. No directional information can be obtained.

3.3.5 Magnetic inelastic neutron scattering from a single crystal sample using a triple axis spectrometer.

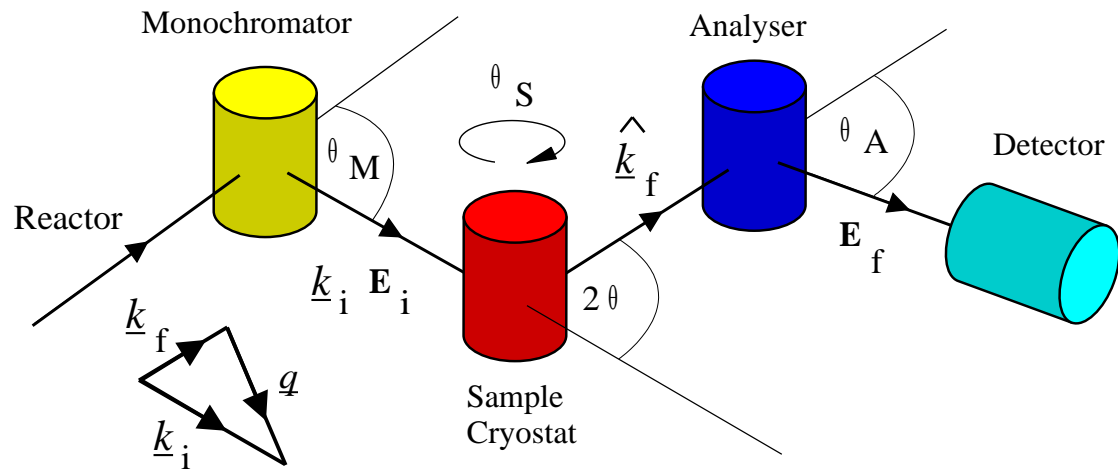


Fig 3.7 : Geometry of a triple axis spectrometer.

A single crystal sample is placed in the sample cryostat so that the scattering plane to be studied is approximately horizontal. The sample cryostat may be tilted to a limited extent afterwards in order to align the crystal precisely. A polychromatic neutron beam is incident on the monochromator. Monochromatic incident neutron beams with different values of \underline{k}_i can be directed towards the sample by altering the angle θ_M . The sample scatters the incident neutrons in all directions with a range of final energies. The angle 2θ is adjusted to move the analyser to a position where it receives neutrons scattered in a particular direction $\hat{\underline{k}}_f$. The angle θ_A is adjusted so that the analyser selects only those neutrons with a particular final energy E_f . In this way, adjustment of the angles 2θ and θ_A allows the detector to count only the neutrons scattered from the sample with a final wavevector \underline{k}_f . Once both \underline{k}_i and \underline{k}_f have been set, the scattering vector $\underline{q} = \underline{k}_i - \underline{k}_f$ and the energy transfer $\omega = (\hbar/2m)(k_i^2 - k_f^2)$ will have been determined. The scattering vector can be orientated with respect to the crystal lattice, within the scattering plane, by altering the angle θ_S . The region of (\underline{q}, ω) space that may be accessed in this way is governed by the values of \underline{k}_i and \underline{k}_f that the spectrometer can produce and measure

respectively. A triple axis spectrometer is operated in one of two ways: ‘constant- $|\underline{k}_i|$ ’ mode, or ‘constant- $|\underline{k}_f|$ ’ mode. The constant- $|\underline{k}_f|$ mode keeps θ_A fixed at each point in a scan through (\underline{q}, ω) space which enables an easier calculation of the resolution of the spectrometer. There are two types of common scan that are performed: a ‘ q -scan’ where the spectrometer measures neutrons scattered with a constant value of ω at different positions in \underline{q} space, and an ‘ ω -scan’ where the spectrometer measures neutrons scattered with different values of ω at the same position in \underline{q} space.

If the nuclear inelastic scattering can be subtracted, equations 3.15 and 3.16 can be used to give the imaginary part of the dynamic, \underline{q} dependent, susceptibility from the magnetic partial differential cross section. This can then be compared with theoretical models of the magnetic properties of the sample under investigation [12].

References.

- [1] <http://www.ill.fr/>
- [2] <http://www.isis.rl.ac.uk/>
- [3] G.L. Squires, *Introduction to the Theory of Thermal Neutron Scattering*, Dover (1996).
- [4] S.M. Bennington *et al.*, *A Practical Neutron Training Course*, RAL-93-083 (1993).
- [5] S.W. Lovesey, *Theory of Neutron Scattering from Condensed Matter*, Vol. 1, Oxford University Press, (1987).
- [6] S.W. Lovesey, *Theory of Neutron Scattering from Condensed Matter*, Vol. 2, Oxford University Press, (1987).
- [7] R.M. White, *Quantum Theory of Magnetism*, Springer Verlag (1982).
- [8] W.G. Williams, *Polarized Neutrons*, Oxford University Press, (1988).
- [9] *The Yellow Book: Guide to Neutron Research Facilities at the I.L.L.*, I.L.L. Publication (1997).
- [10] G.J. McIntyre, *Neutron and Synchrotron Radiation for Condensed Matter Studies*, Vol. 1, Chap. VII, Springer-Verlag (1994).

-
- [11] *International Tables for Crystallography*, Vol. C, Kluwer (1992)
- [12] *Neutron and Synchrotron Radiation for Condensed Matter Studies*, Vol. 1, Chap. VII, Springer-Verlag (1994).

CHAPTER 4

DATA ANALYSIS

This chapter outlines the data analysis techniques used in this thesis. It describes how Bayesian probability theory provides a unifying mathematical framework for deriving the procedures of least squares refinement and maximum entropy image construction. A derivation of the appropriate raw errors to be assigned in scattering experiments is also given.

4.1 The basic rules of probability.

The basic rules of probability theory are given in two equations: the sum rule, and the product rule. The sum rule is

$$\text{prob}(A|I) + \text{prob}(\bar{A}|I) = 1, \quad \text{Eq 4.1}$$

and states that the probability that A is true plus the probability that A is false is equal to one. The symbol ‘|’ means ‘given’, so everything to the right of this symbol is taken to be true. The letter I stands for the relevant background information that is available; this is needed, as calculations in probability are always based on a stated group of assumptions, which must be specified if the calculation is to have any meaning. The product rule is

$$\text{prob}(A, B|I) = \text{prob}(A|B, I) \times \text{prob}(B|I), \quad \text{Eq 4.2}$$

and states that the probability that both A and B are true is equal to the probability that A is true, given that B is true, multiplied by the probability that B is true irrespective of A .

In general, if $\{A_{n=1}^N\}$ is a set of parameters, then $\text{prob}(\{A\}|I)$ is an N dimensional function called the probability density function.

4.2 Bayesian probability theory.

The Bayesian formulation of probability theory provides a unified framework for deriving results in probability and statistical analysis. At the heart of this framework are two equations derived from the basic rules of probability: Bayes' theorem, and the theory of marginalisation.

Bayes' theorem is

$$\text{prob}(A|B, I) = \frac{\text{prob}(B|A, I) \times \text{prob}(A|I)}{\text{prob}(B|I)}, \quad \text{Eq 4.3}$$

and can easily be derived from the product rule. It is extremely useful for the analysis of experimental data, as will be seen in the following sections, as it relates $\text{prob}(A|B, I)$ to $\text{prob}(B|A, I)$. The theory of marginalisation is

$$\text{prob}(A|I) = \int_{-\infty}^{+\infty} \text{prob}(A, B|I) dB, \quad \text{Eq 4.4}$$

and provides a mechanism for removing a probability density function's dependence on a variable that is of no interest in an experiment.

Two statistical analysis techniques are used in this thesis: least squares refinement, and maximum entropy image construction. The justification for using both of these, in the applicable situation, can be found within the Bayesian formulation. The calculation of the errors associated with the counting of neutrons can also be performed within this framework.

4.3 Least squares refinement.

In least squares refinement, a set of experimental data $\{D_{n=0}^N\}$ is compared with a set of theoretical data $\{F_{n=0}^N\}$ generated from a model of the sample under investigation. Within this model, there are a set of parameters $\{X_{m=0}^M\}$ that can be iteratively adjusted until the experimental and theoretical data agree to the desired tolerance. In this raw form, least squares refinement is most effective when the sample model is well determined and the number of sample parameters is small.

From Bayes' theorem, the probability that the sample parameters are equal to $\{X_m\}$, given a set of data $\{D_n\}$, is

$$\text{prob}(\{X_m\}|\{D_n\}, I) = C \times \text{prob}(\{D_n\}|\{X_m\}, I) \times \text{prob}(\{X_m\}|I). \quad \text{Eq 4.5}$$

This is called the posterior probability density function; the denominator in Bayes' theorem has been rewritten as a normalisation constant C , as it is of no importance to the following analysis. The term $\text{prob}(\{X_m\}|I)$ is called the prior probability density function, and reflects everything that is known concerning the sample parameters before the collection of the data. If nothing is known, this can be set to a constant

$$\text{prob}(\{X_m\}|I) = \text{constant}, \quad \text{Eq 4.6}$$

and absorbed into C . The posterior p.d.f. can now be written as

$$\text{prob}(\{X_m\}|\{D_n\}, I) = C \times \text{prob}(\{D_n\}|\{X_m\}, I). \quad \text{Eq 4.7}$$

The term on the right is called the likelihood function, and gives the probability of obtaining the set of data $\{D_n\}$ given that the sample parameters are equal to $\{X_m\}$. If the data are independent, then it can be written as

$$\text{prob}(\{D_n\}|\{X_m\}, I) = \prod_{n=1}^N \text{prob}(D_n|\{X_m\}, I), \quad \text{Eq 4.8}$$

using repeated application of the product rule. If the variations associated with the experimental measurements form a Gaussian distribution, then the probability of measuring an individual datum can be written as

$$\text{prob}(D_n|\{X_m\}, I) = \frac{1}{\sigma_n \sqrt{2\pi}} \exp\left(-\frac{(F_n(\{X_m\}) - D_n)^2}{2\sigma_n^2}\right), \quad \text{Eq 4.9}$$

where σ_n is the standard deviation associated with the n^{th} datum. Equations 4.7, 4.8 and 4.9 combine to give

$$\text{prob}(\{X_m\}|\{D_n\}, I) = C \exp\left(-\sum_{n=1}^N \frac{(F_n(\{X_m\}) - D_n)^2}{2\sigma_n^2}\right), \quad \text{Eq 4.10}$$

if the coefficients of the exponential terms in equation 4.9 are absorbed into the constant C . The above function can vary very rapidly with the values of the sample parameters. For this reason, it is often more convenient to work with the logarithm of the posterior p.d.f. This gives

$$L = \ln \left[\text{prob}(\{X_m\}|\{D_n\}, I) \right] = \ln C - \frac{\chi^2}{2}, \quad \text{Eq 4.11}$$

where

$$\chi^2 = \sum_{n=1}^N \frac{(F_n(\{X_m\}) - D_n)^2}{\sigma_n^2} \quad \text{Eq 4.12}$$

is the sum of the squares of the normalised residuals $R_n = (F_n - D_n)/\sigma_n$. The most probable values of the sample parameters $\{X_{m0}\}$ will be obtained when L is a maximum. The condition for this maximum L_0 , is given by the sets of equations

$$\left(\frac{\partial L}{\partial \{X_m\}} \right)_{\{X_{m0}\}} = 0 \quad \text{and} \quad \left(\frac{\partial^2 L}{\partial \{X_m\}^2} \right)_{\{X_{m0}\}} < 0. \quad \text{Eq 4.13}$$

The errors associated with the $\{X_{m0}\}$ are given by the covariance matrix

$$\sigma_{ij}^2 = - \left(\frac{\partial^2 L}{\partial X_i \partial X_j} \right)_{\{X_{m0}\}}^{-1}, \quad (1 < i < M, \quad 1 < j < M), \quad \text{Eq 4.14}$$

which is derived from a Taylor series expansion of L around L_0 . The values of the $\{\sigma_{ii}\}$ give the standard deviations associated with the values of the $\{X_{i0}\}$, and the values of the $\{\sigma_{ij}^2\}$ provide information on the correlations between the values of the $\{X_{i0}\}$ and the $\{X_{j0}\}$ (for $i \neq j$).

In principle, the method for determining the values of the $\{X_{m0}\}$ is simple. An initial guess is made for the values of the sample parameters $\{X_{mg}\}$, and the values of $(\partial L / \partial \{X_m\})_{\{X_{mg}\}}$ calculated. These local gradient values are used to determine changes in the values of the sample parameters $\{\Delta X_m\}$ needed to move nearer to L_0 . This is repeated iteratively, until equation 4.12 is satisfied and the values of the $\{X_{m0}\}$ determined. The ease with which this is accomplished is heavily dependent on the shape of the function L , which is, in turn, dependent on the function $F_n(\{X_m\})$.

A measure of the agreement between the experimental and theoretically generated data is given by χ^2 . A good agreement is often thought to have been achieved when $\chi^2 \approx N$, as this implies that each experimental datum agrees on average with its theoretical counterpart to a tolerance of the standard deviation of the experimental data.

4.4 Maximum entropy and image construction.

If the properties of the sample are not understood very well, the least squares sample model will necessarily be very general, and will contain a large number of sample parameters in order to provide sufficient flexibility in the refinement. As the number of sample parameters increases past a certain point, the function L will become flat in certain directions in the parameter space $\{X_m\}$, and the technique of least squares refinement will cease to be a reliable method of analysis. This is because there will be many sets of values of the sample parameters that maximise L , and it will therefore be impossible to determine a unique set of the most probable values $\{X_{m0}\}$. In other words, the information contained within the data is less than that required to give unique values for all the sample parameters. Therefore, in order to proceed, it becomes necessary to introduce further information. If it is not possible to increase the number of data, or introduce a more specific model that reduces the number of sample parameters, the only option is to think more carefully about the assignment of the prior probability density function $\text{prob}(\{X_m\}|I)$. This situation can arise when the experimental data is used to give a real space image of some property in the sample. In this case, the sample parameters are the intensities of pixels in this image, and they will be large in number to achieve the necessary resolution.

The principle of maximum entropy states that when least squares refinement gives more than one set of values for the most probable sample parameters, the set with the largest entropy should be chosen. The set with the largest entropy will be the set that contains the least amount of information, or is the least complex. This set is more formally defined as the set that is most likely to arise out of pure chance while also

being compatible with the data. This set is chosen because all the information contained within the data has been used in deriving the function L , and there is therefore no justification for introducing further complexity into the sample parameters. This principle can be used in the assignment of the prior probability density function in an improved version of the least squares refinement.

In the case where the sample parameters are used to produce an image, the entropy of the image is given by

$$S = - \sum_{m=1}^M X_m \ln \left[\frac{X_m}{X_{mg}} \right]. \quad \text{Eq 4.15}$$

This form of the entropy is known as the Shannon-Jaynes entropy, as it includes the terms $\{X_{mg}\}$. In formal maximum entropy theory these terms are known as the measure. In effect, they define the position of the global maximum of entropy before any data has been introduced. In this context, they are simply the initial guesses of the pixel intensities in the image, and are all set to the same value as this corresponds to an image with no information or detail. There is still the question of what this value should be, as will be discussed in section § 5.2.5.2.3.

The principle of maximum entropy gives an assignment for the prior probability density function as

$$\text{prob}(\{X_m\}|I) \propto \exp(S), \quad \text{Eq 4.16}$$

which states that, before any data has been collected, the image with the highest entropy is favoured. If the above equation is used in the least squares method, instead of assigning a value of unity to $\text{prob}(\{X_m\}|I)$, equation 4.5 becomes

$$L_S = \ln \left[\text{prob}(\{X_m\}|\{D_n\}, E, I) \right] = \ln C - ES - \frac{\chi^2}{2}. \quad \text{Eq 4.17}$$

The above equation is the same as the least squares equation, except that it has a constraining term ES which always favours the image containing the least amount of information.

The term E is a function that is used to give a weighting between the entropy term and the least squares term. As for the least squares case, the above equation must be maximised in order to find the most probable values of the pixel intensities in the image. This maximisation can be thought of as a contest between disorder (entropy term) and order (least squares term), with E determining the relative contributions of each. If the data is of good quality, E will have a small value and the least squares term will have a large contribution to the maximisation of L_S . If the data is of bad quality, then E will have a large value and the entropy term will have a larger importance in the maximisation. For the case where the variations associated with the experimental measurements form a Gaussian distribution, E is often chosen such that $\chi^2 \approx N$ after the maximisation has been completed. This will be discussed further in § 5.2.5.2.3.

The condition for the maximum value of L_S , L_{S0} is given by the sets of equations

$$\left(\frac{\partial}{\partial \{X_m\}} \left[ES - \frac{\chi^2}{2} \right] \right)_{\{X_{m0}\}} = 0, \text{ and } \left(\frac{\partial^2}{\partial \{X_m\}^2} \left[ES - \frac{\chi^2}{2} \right] \right)_{\{X_{m0}\}} < 0.$$

Eq 4.18

As for least squares refinement, in principle, the method for determining the values of the $\{X_{m0}\}$ is simple. The values of the pixel intensities are set to values where they have maximum entropy $\{X_{mg}\}$. The values of $(\partial (ES)/\partial \{X_m\})_{\{X_{mg}\}}$ and $(\partial(\chi^2)/\partial \{X_m\})_{\{X_{mg}\}}$ are calculated, and the changes in the pixel intensities $\{\Delta X_m\}$ needed to reduce χ^2 while keeping S as large as possible are determined.

This is repeated iteratively, until equation 4.18 is satisfied and the values of $\{X_{m0}\}$ determined.

As in the least squares method, the errors associated with the $\{X_{m0}\}$ are given by the covariance matrix

$$\sigma_{ij}^2 = - \left(\frac{\partial^2 L_S}{\partial X_i \partial X_j} \right)_{\{X_{m0}\}}^{-1}, \quad (1 < i < M, \quad 1 < j < M), \quad \text{Eq 4.19}$$

As M is large, the error associated with a particular pixel intensity is likely to be large. However, as these pixels are small, a detail in the image may often be spread over many pixels. In this case, it is more appropriate to calculate the error associated with the sum of the pixel intensities in the entire image detail

$$d = \sum_{m=1}^M X_m u_m, \quad \text{Eq 4.20}$$

where u_m is equal to 1 if the pixel is part of the detail and 0 otherwise. The standard deviation of d is given by

$$\sigma(d) = \left[u_i \left(\frac{\partial^2 L_S}{\partial X_i \partial X_j} \right)_{\{X_{m0}\}}^{-1} u_j \right]^{1/2}. \quad \text{Eq 4.21}$$

In this thesis, the technique of maximum entropy is used to give three dimensional images of magnetisation density in single crystals from magnetic unit cell structure factors measured using the D3 diffractometer at the I.L.L.

4.5 Maximum entropy and counting statistics.

In general, neutron scattering experiments involve counting the number of neutrons P_N scattered in a particular direction (perhaps with a particular energy and spin state) for a fixed period of time T . If any statistical analysis is to be performed on the information obtained from such a measurement, the standard deviation $\sigma(P_N)$ of P_N has to be calculated. In order to do this, the probability of measuring a different number of neutrons P in a second hypothetical experiment has to be calculated. In the Bayesian formulation, this corresponds to determining the probability density function $\text{prob}(P|P_N, I)$.

As P has only been measured once, the average value for P , $\langle P \rangle$ is equal to P_N . This can be written as

$$\langle P \rangle = \sum_{P=0}^{\infty} P \text{prob}(P|P_N, I) = P_N, \quad \text{Eq 4.22}$$

and provides the only piece of information concerning this probability density function. There will be many probability density functions that satisfy this constraint, so more information is needed to arrive at a unique choice. As with deciding amongst the equally probable images in the previous section, the principle of maximum entropy can provide this extra information. In this case, the Shannon-Jaynes entropy is written as

$$S = - \sum_{P=0}^{\infty} \text{prob}(P|P_N, I) \log \left[\frac{\text{prob}(P|P_N, I)}{\text{prob}(P|I)} \right], \quad \text{Eq 4.23}$$

where $\text{prob}(P|I)$ is the probability density function for P appropriate before the value of P_N has been measured. By comparing with equation 4.15, it can be seen that $\text{prob}(P|I)$ is the measure. It gives the value of P that one would choose without

access to any data, and is assigned by assuming that in any small increment of time dT , during the period T , the probability of counting a neutron is the same as the probability of not counting a neutron (i.e. equal to $1/2$). If this is the case, then $\text{prob}(P|I)$ will not be uniform; the probability of counting P neutrons will be proportional to the number of ways that their detection can be distributed over the total counting time T . This leads (in the limit of $dT \rightarrow 0$) to an assignment of the measure as

$$\text{prob}(P|I) = \lim_{dT \rightarrow 0} \frac{(T/dT)^P}{P!} \exp\left(-\frac{T}{dT}\right). \quad \text{Eq 4.24}$$

The equation that has to be maximised in order to determine $\text{prob}(P|P_N, I)$ is given by

$$L_S = - \sum_{P=0}^{\infty} \text{prob}(P|P_N, I) \log \left[\frac{\text{prob}(P|P_N, I)}{\text{prob}(P|I)} \right] + \lambda \left[P_N - \sum_{P=0}^{\infty} P \text{prob}(P|P_N, I) \right]. \quad \text{Eq 4.25}$$

This equation is of exactly the same form as equation 4.17 as it consists of an entropy term that is constrained by the available data. Its solution is

$$\text{prob}(P|P_N, I) = \frac{(P_N)^P \exp(-P_N)}{P!}, \quad \text{Eq 4.26}$$

which is the Poisson distribution. If P_N is large, this can be approximated by the Gaussian distribution, and if this is done the value for the standard deviation of P_N is found to be

$$\sigma(P_N) = \sqrt{P_N}. \quad \text{Eq 4.27}$$

References

- [1] D.S. Sivia, *Data Analysis: A Bayesian Tutorial*, Oxford University Press (1998).

CHAPTER 5

ELASTIC NEUTRON SCATTERING EXPERIMENTS

This chapter contains the experiments to determine the magnetisation density in $\text{YbNi}_2\text{B}_2^{11}\text{C}$, $\text{ErNi}_2\text{B}_2^{11}\text{C}$, $\text{HoNi}_2\text{B}_2^{11}\text{C}$ and $\text{LuNi}_2\text{B}_2^{11}\text{C}$. These experiments were performed on the D9 and D3 diffractometers at the I.L.L. This chapter also contains a description of an experiment performed using the D10 diffractometer at the I.L.L. that was designed to search for magnetic order in the $\text{YbNi}_2\text{B}_2^{11}\text{C}$ compound at low temperatures. An experiment using the D1B diffractometer at the I.L.L., needed to determine the amount of Yb_2O_3 impurity present in the $\text{YbNi}_2\text{B}_2^{11}\text{C}$ polycrystalline sample, is also included.

5.1 Determination of the nuclear structure, average crystallite radius and mosaic spread of single crystals of $\text{RNi}_2\text{B}_2^{11}\text{C}$ [R = Yb, Er, Ho, Lu] using unpolarised elastic neutron scattering and the D9 diffractometer at the I.L.L.

5.1.1 Aims of the experiment.

In order to calculate the magnetisation density in a single crystal from the flipping ratios obtained in the D3 experiment (§ 5.2), the nuclear structure, including the thermal displacement parameters, average crystallite radius, and mosaic spread of that crystal must be known. In this experiment, these quantities were determined for single crystals of $\text{RNi}_2\text{B}_2^{11}\text{C}$, [R = Yb, Er, Ho, Lu].

5.1.2 Sample preparation.

The single crystals used in this experiment were prepared at the Ames laboratory using the Ni_2B^{11} flux growth technique [1]. The B^{11} isotope was used as it has a considerably lower neutron absorption cross section as compared with naturally

occurring boron (containing 20% by mass of B¹⁰). The following grey ‘flat-plate’ crystals were obtained:

Crystal	Mass (mg)	~Length (mm)	~Width (mm)	~Thickness (mm)
YbNi ₂ B ₂ ¹¹ C	73	5.5	5.0	0.5
ErNi ₂ B ₂ ¹¹ C	160	4.7	4.5	0.6
HoNi ₂ B ₂ ¹¹ C	45	3.8	3.5	0.4
LuNi ₂ B ₂ ¹¹ C	89	7.0	4.5	0.55

Fig 5.1 : Approximate masses and dimensions of the single crystal samples.

5.1.3 Data collection.

For each crystal, sets of Bragg peak intensities $\{ I(\underline{\tau}) \}$ were measured using the technique described in § 3.3.1.2. Measurements were made at different neutron wavelengths to aid in the determination of the average crystallite radius and mosaic spread of the crystal (see § 5.1.4.2). For each set of intensities, a standard reflection was periodically measured to check that D9, the reactor and the crystal were stable throughout the experiment.

Crystal	Temperature (K)	Wavelength (Å)	Number of reflections measured	Number of independent reflections	Range of h	Range of k	Range of l	Range of θ (°)
YbNi ₂ B ₂ ¹¹ C	15	0.548	881	302	-3 to 10	-8 to 7	-24 to 24	5 to 52
		0.706	507	153	-4 to 6	-6 to 5	-19 to 19	6 to 40
		0.840	528	154	-2 to 6	-6 to 5	-19 to 19	4 to 50
ErNi ₂ B ₂ ¹¹ C	20	0.548	1091	298	-4 to 8	-8 to 7	-24 to 24	5 to 40
		0.840	652	153	-4 to 6	-6 to 5	-19 to 19	5 to 50
HoNi ₂ B ₂ ¹¹ C	20	0.548	874	299	-4 to 8	-8 to 7	-24 to 24	5 to 40
		0.706	586	159	-4 to 6	-7 to 5	-19 to 19	6 to 53
		0.840	702	163	-4 to 6	-6 to 5	-19 to 19	5 to 53
LuNi ₂ B ₂ ¹¹ C	15	0.548	1061	297	0 to 10	0 to 8	-24 to 24	5 to 52
		0.840	664	180	-6 to 6	0 to 6	-20 to 20	5 to 55

Fig 5.2 : The data collected in the D9 experiment.

5.1.4 Correction factors.

Equation 3.25 relates the Bragg peak intensity $I(\underline{\tau})$ to the nuclear unit cell structure factor $F_N(\underline{\tau})$. This equation is based on a number of ideal assumptions concerning the diffraction process. In a real experiment, these assumptions are not valid, and the equation must be modified if it is to be used to determine the desired information concerning the crystal [2].

$$I(\underline{\tau}) = \frac{V}{v_0^2} \Phi \frac{\lambda^3}{\sin 2\theta} |F_N^{\text{uncorr}}(\underline{\tau})|^2 = \frac{V}{v_0^2} \Phi \frac{\lambda^3}{\sin 2\theta} A(\underline{\tau})E(\underline{\tau})M(\underline{\tau}) |F_N^{\text{corr}}(\underline{\tau})|^2 \quad \text{Eq 5.1}$$

The factors $A(\underline{\tau})$, $E(\underline{\tau})$ and $M(\underline{\tau})$ represent corrections made in order to take account of absorption, extinction and multiple scattering of the neutrons as they pass through the sample crystal. It follows that $F_N^{\text{corr}}(\underline{\tau})$ is the structure factor that has been corrected for absorption, extinction and multiple scattering, and $F_N^{\text{uncorr}}(\underline{\tau})$ is the structure factor that has not.

5.1.4.1 Absorption and incoherent scattering.

When a monochromatic neutron beam of initial intensity I_0 passes through a homogeneous sample of thickness p , its intensity is reduced due to absorption and incoherent scattering to

$$I_A = I_0 \exp(-\mu p), \quad \text{Eq 5.2}$$

where μ is the total linear attenuation coefficient. This coefficient is given by

$$\mu = \frac{\rho}{m_c} \sum_i n_i (\sigma_{Ai}(\lambda) + \sigma_{Ii}), \quad \text{Eq 5.3}$$

where m_c is the mass of the unit cell, n_i is the number of atoms of type i in the unit cell, and ρ is the density of the sample. The absorption cross section for the i^{th} atom is σ_{Ai} , and refers to the capture of neutrons by the nuclei of the atoms; it is a function of the neutron wavelength λ . The incoherent scattering cross section for the i^{th} atom is σ_{Ii} , and is normally considered to be independent of the neutron wavelength; incoherent scattering is included here, as it results in an apparent absorption of the coherent beam [2] [3] (see § 3.2.2.1).

It can be seen from the two preceding equations that the absorption of neutrons by a sample depends on the physical properties of the unit cell, the wavelength of the neutrons, and the path length that the neutrons travel through the sample. Absorption is independent of whether the sample is in a powder or a single crystal form.

The above theory can be used to determine the value for $A(\underline{\tau})$ in equation 5.1. The physical properties of the unit cell and the neutron wavelength are constant for each value of $\underline{\tau}$, but the path length is different. In order to calculate the path length for each value of $\underline{\tau}$, the crystal dimensions and the orientation of the crystal with respect to its reciprocal lattice must be known.

5.1.4.2 Extinction.

Corrections due to extinction are necessary when performing diffraction experiments using single crystal samples. In general, a single crystal is not perfect, and consists of many crystallites. These crystallites may be of differing sizes, and are misaligned with respect to one another. In the mosaic crystal model, a single crystal can be characterised by two parameters with respect to these imperfections: the average crystallite radius t , and the mosaic spread g which is a measure of the angular variation of the alignment of the crystallites [4].

Extinction is a reduction of the intensity of the incident or diffracted neutron beam due to coherent scattering, and exists in two forms: primary, and secondary extinction. In general, both types of extinction occur within a crystal.

Primary extinction occurs in crystals where t is large enough to cause a substantial reduction in the intensity of the incident beam within an individual crystallite. In this case, after the incident beam has travelled a small distance into a crystallite at the surface of the crystal, the majority of it will have been diffracted. This reduction in intensity of the incident beam means that crystal planes further inside the crystallite contribute less to the diffraction. Also, because of the perfect alignment of the crystal planes, the diffracted beam can be rescattered within the crystallite, causing it to become parallel to the incident beam again. This causes an overall reduction in the intensity of the diffracted beam. These effects can be thought of as an interference between the incident and diffracted beams within the crystallite causing a mutual transfer of intensity.

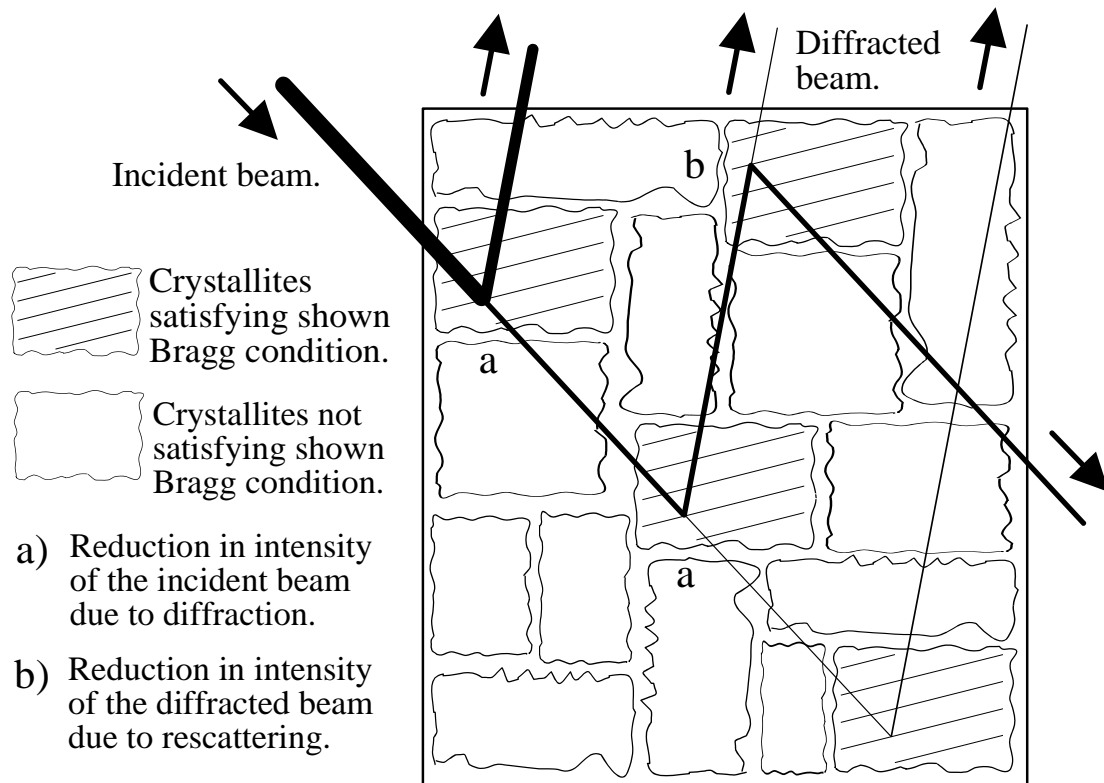


Fig 5.4 : Secondary extinction.

Simple scattering theory assumes that the incident beam is not reduced in intensity by diffraction, and the diffracted beam does not undergo rescattering. As can be seen from the above descriptions of primary and secondary extinction, these two assumptions are invalid. The corrections to the Bragg peak intensities due to extinction are given by

$$I_U(\tau) = E(\tau)I_C = y_P(\tau)y_S(\tau)I_C, \quad \text{Eq 5.4}$$

where I_U is the uncorrected intensity, and I_C is the corrected intensity [5]. The corrections for primary and secondary extinction are treated independently, and are given by y_P and y_S ; these are combined to give the total correction E . The starting point in the calculation of both extinction corrections is a differential equation expressing the mutual transfer of intensity between incident and diffracted beams

$$\frac{\partial I_I}{\partial x} + \frac{\partial I_D}{\partial y} = 0, \quad \text{Eq 5.5}$$

where (x, y) is a general point in the crystal. An analytic integration of this equation across the whole crystal is not possible, even for the simplest crystal shapes. Therefore, the integration is done numerically, and analytic expressions for y_P and y_S are found by a least squares fit to the data. These are

$$y_P = \left[1 + 2x_P + \frac{A_P(\theta)x_P^2}{1 + B_P(\theta)x_P} \right]^{-1/2}, \quad x_P = \frac{t\lambda^3}{v_0^2 \sin(2\theta)} f(t, g) |F_N(\underline{r})|^2, \quad \text{Eq 5.6}$$

and

$$y_S = \left[1 + 2x_S + \frac{A_S(\theta)x_S^2}{1 + B_S(\theta)x_S} \right]^{-1/2}, \quad x_S = \frac{\bar{T}\lambda^3}{v_0^2 \sin(2\theta)} f(t, g) |F_N(\underline{r})|^2, \quad \text{Eq 5.7}$$

where \bar{T} is the absorption weighted mean path length through the crystal for the reflection, and F_N is the nuclear structure factor. The neutron wavelength is λ , v_0 is the volume of the unit cell, and $f(t, g)$ is a function of the average crystallite radius and mosaic spread of the crystal. The angle between the incident and diffracted beams is 2θ , and $A_p(\theta)$, $B_p(\theta)$, $A_s(\theta)$ and $B_s(\theta)$ are functions of θ only [6].

The relative amounts of primary and secondary extinction, for a particular reflection, are determined by the values of \bar{T} , t , g and θ . The fact that both types of extinction are proportional to λ^3 is important, as this dependence is useful for characterising the extinction in an experiment.

5.1.4.3 Multiple scattering.

Multiple scattering is a transfer of intensity between the incident or diffracted beams of two different reflections k and h [2]. Some of the intensity of the incident beam for reflection k can be taken by reflection h , reducing the intensity of the diffracted beam for reflection k . This process is known as 'Aufhellung'. Also, the diffracted beam for reflection h can be considered to contribute to the incident beam for the reflection $k-h$. This causes an increase in the intensity of the diffracted beam for the $k-h$ reflection. This is called 'Umweganregung'. Multiple scattering depends on the size, mosaic spread and crystallite radius of the sample and the divergence of the incident neutron beam. It is almost independent of the neutron wavelength. For crystal structures with a high density of reflections, the Umweganregung effect is the more serious. A reasonable correction can often be made by subtracting a fixed contribution from all the reflections [7]. This results in a large percentage reduction in the intensities of the weak reflections, but makes a much smaller difference to the more intense reflections. Extinction, where the incident and diffracted beams are from the same reflection, is a special cases of multiple scattering and is the larger effect.

5.1.5 Analysis of the data.

The processing of the data was performed using three of the standard diffraction data analysis computer programs available at the I.L.L: RACER, DATAP and REFORM. The least squares refinement was performed using the SFLSQ program of the Cambridge Crystallography Subroutine Library (C.C.S.L.) [8]. All the programs are written in the FORTRAN language.

For each crystal, RACER, DATAP and REFORM were used to produce sets of nuclear structure factors for each neutron wavelength. A SFLSQ refinement was performed on each data set to determine the multiple scattering correction needed to be made to the output of DATAP (see § 5.1.5.1.2.1). After these corrections had been made, for each crystal, the corrected files output by REFORM at different wavelengths were combined and the final least squares refinement performed on the combined data.

5.1.5.1 Determination of the positions and thermal parameters of the atoms in the unit cell, and the average crystallite radius and mosaic spread of the crystal using least squares refinement.

5.1.5.1.1 RACER.

RACER calculates the integrated Bragg peak intensities from the collected data. The raw data from a D9 experiment is stored as a three dimensional array of intensities. The three dimensions correspond to the x and z positions of the multidetector, and the rotation of the crystal ω . In order to determine the correct total intensity of the Bragg peak, a determination of the 3-D peak profile and background intensity is made, so that the three dimensional integration does not include a large contribution from the background. This would cause the estimated standard deviation of the peak intensity to be artificially high which could prevent a successful measurement of the weak reflections. In RACER, the strong reflections are used to determine ellipsoids in x , z and ω , throughout the observational space, that contain the minimum amount of background intensity while still being certain to include the whole peak. These ellipsoids are then used as *a priori* boundaries when performing the integration of the weak reflections in the same region of detector space. After RACER has calculated the Bragg peak intensities $\{ I(\underline{\tau}) \}$ and their standard deviations $\{ \sigma [I(\underline{\tau})] \}$, it calculates the corresponding set of the squares of the uncorrected nuclear unit cell structure factors $\{ | F_N^{\text{uncorr}}(\underline{\tau})|^2 \}$ and their standard deviations $\{ \sigma [| F_N^{\text{uncorr}}(\underline{\tau})|^2] \}$ [9].

5.1.5.1.2 DATAP.

DATAP takes the output from RACER, along with a file that contains the total linear absorption coefficient, the crystal dimensions, and information that allows the orientation of the reciprocal lattice of the crystal to be calculated with respect to the angles of the Eulerian cradle, and calculates the transmission factors $\{ A(\underline{\tau}) \}$, and the absorption weighted mean path lengths $\{ \bar{T}(\underline{\tau}) \}$ for each reflection. The $\{ \bar{T}(\underline{\tau}) \}$ are used by REFORM to calculate parameters that are used by SFLSQ to calculate the extinction corrections. DATAP then corrects the squares of the nuclear unit cell

structure factors for absorption $\{|F_N^{\text{uncorr}}(\underline{\tau})|^2/A(\underline{\tau})\}$, and calculates the corrected standard deviations $\{\sigma[|F_N^{\text{uncorr}}(\underline{\tau})|^2/A(\underline{\tau})]\}$. DATAP outputs $\{\bar{T}(\underline{\tau})\}$, $\{A(\underline{\tau})\}$ $\{|F_N^{\text{uncorr}}(\underline{\tau})|^2/A(\underline{\tau})\}$ and $\{\sigma[|F_N^{\text{uncorr}}(\underline{\tau})|^2/A(\underline{\tau})]\}$.

5.1.5.1.2.1 Multiple scattering correction to the output of DATAP.

For all four crystals, the experimentally determined nuclear structure factors were found to be systematically higher than their theoretical counterparts for the weak reflections in the initial refinements of the crystal structures (e.g. fig 5.5). This implied that the data needed to be corrected for the ‘Umweganregung’ multiple scattering process (see § 5.1.4.3). This was done by subtracting a fixed contribution C from all of the squares of the nuclear unit cell structure factors $\{|F_N^{\text{uncorr}}(\underline{\tau})|^2/A(\underline{\tau})\}$ output from DATAP. The size of this contribution was taken to be the average difference in the squares of the experimentally and theoretically determined structure factors of the weak reflections output by SFLSQ.

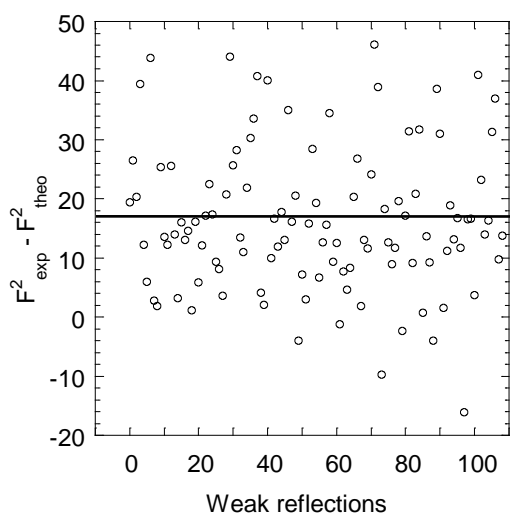


Fig 5.5 : Differences in the squares of the experimentally and theoretically determined structure factors of the weak reflections for $\text{LuNi}_2\text{B}_2^{11}\text{C}$ using a neutron wavelength of 0.0840 \AA .

$$C = F^2_{\text{exp}} - F^2_{\text{theo}} = 18.$$

The multiple scattering correction had little effect on the final refined parameters, but will prove important in the analysis of the polarised neutron data (see § 5.2).

5.1.5.1.3 REFORM.

REFORM takes the output from DATAP and calculates the nuclear unit cell structure factors (corrected for absorption) $\{ F_N^{\text{uncorr}}(\underline{\tau}) / \sqrt{A(\underline{\tau})} \}$, and their standard deviations $\{ \sigma [F_N^{\text{uncorr}}(\underline{\tau}) / \sqrt{A(\underline{\tau})}] \}$. It also calculates four parameters $C1$, $C2$, $C3$ and $C4$, that are used by SFLSQ to calculate the extinction corrections. REFORM outputs all these quantities.

5.1.5.1.4 SFLSQ.

SFLSQ performs the least squares refinement. Using the notation of § 4.3, the experimental data are given by

$$\{ D_{n=1}^N \} = \{ F_N^{\text{uncorr}}(\underline{\tau}) / \sqrt{A(\underline{\tau})} \}, \quad \text{Eq 5.8}$$

and their standard deviations by

$$\{ \sigma_{n=1}^N \} = \left\{ \sigma \left[F_N^{\text{uncorr}}(\underline{\tau}) / \sqrt{A(\underline{\tau})} \right] \right\}. \quad \text{Eq 5.9}$$

Using equations 5.1 and 3.22, the theoretically generated data are given by

$$\{ F_{n=1}^N \} = \left\{ \sqrt{E(\underline{\tau})} F_N^{\text{corr}}(\underline{\tau}) \right\} = \left\{ \sqrt{E(\underline{\tau})} \sum_d \langle b_d \rangle_{\text{sp,iso}} \exp(i \underline{\tau} \cdot \underline{d}) \exp(-W_d) \right\}. \quad \text{Eq 5.10}$$

The right hand side of the above equation is calculated from a model of the unit cell, average crystallite radius and mosaic spread of the crystal. It is a function of many variables, some of which are known before the experiment is performed, and some that can be treated as adjustable parameters in the least squares refinement $\{ X_{m=1}^M \}$.

Known variables.	Adjustable sample parameters $\{X_m\}$.
λ neutron wavelength.	t average crystallite radius of the crystal.
μ total linear absorption coefficient for the sample.	g mosaic spread of the crystal.
$\{\underline{\tau}\}$ reciprocal lattice vectors for the reflections .	$\{\underline{d}\}$ basis positions of the atoms.
$\{p\}$ path lengths for the reflections (function of crystal dimensions).	$\{B_{ii_d}\}$ anisotropic temperature factors of the atoms.
$\{\langle b_d \rangle\}$ scattering lengths for the atoms.	

Fig 5.6 : Known variables and adjustable sample parameters in the least squares refinement.

SFLSQ takes the output from REFORM and a file that contains the contains initial guesses for the values of the adjustable sample parameters $\{X_{mg}\}$. Equations 5.8, 5.9 and 5.10 can be substituted into equation 4.10, to give the probability density function for the sample parameters

$$\text{prob}\left(\{X_m\}|\{D_n\}, I\right) = C \exp - \sum_{n=1}^N \left[\frac{\left[\left(\sqrt{E} F_N^{\text{corr}}(\{X_{m=1}^M\}) \right)_n - \left(\frac{F_N^{\text{uncorr}}}{\sqrt{A}} \right)_n \right]^2}{2 \left[\sigma_n \left(\frac{F_N^{\text{uncorr}}}{\sqrt{A}} \right) \right]^2} \right].$$

Eq 5.11

SFLSQ maximises this function to obtain the most probable values for the sample parameters $\{X_{m0}\}$ (a description of the general method used to do this is given in § 4.3). After the refinement, SFLSQ changes the values of the sample parameters to their most probable values. An additional file is output that contains the experimental

data $\{ F_N^{\text{uncorr}}(\underline{\tau})/\sqrt{A(\underline{\tau})} \}$, their standard deviations $\{ \sigma [F_N^{\text{uncorr}}(\underline{\tau})/\sqrt{A(\underline{\tau})}] \}$, the theoretically generated data $\{ \sqrt{E(\underline{\tau})} F_N^{\text{corr}}(\underline{\tau}) \}$ and the normalised residuals

$$\left\{ R_{n=1}^N \right\} = \left\{ \frac{\left(\sqrt{E(\underline{\tau})} F_N^{\text{corr}}(\underline{\tau}) \right)_n - \left(F_N^{\text{uncorr}}(\underline{\tau})/\sqrt{A(\underline{\tau})} \right)_n}{\sigma_n \left[F_N^{\text{uncorr}}(\underline{\tau})/\sqrt{A(\underline{\tau})} \right]} \right\}.$$

At the end of the output file, there are a set of values that characterise the success of the refinement. The most important of these are the sum of the normalised residuals

$$R = \frac{1}{N} \sum_{n=1}^N R_n \quad \text{and} \quad \chi^2 = \frac{1}{N} \sum_{n=1}^N (R_n)^2 \quad \text{where } N \text{ is the number of observed reflections.}$$

As SFLSQ calculates the extinction corrections in producing the theoretically generated data, the set of extinction corrections $\{ E(\underline{\tau}) \}$ are also output.

5.1.5.2 Calculation of the real space unit cell lattice vectors using least squares refinement.

Accurate values for the real space unit cell lattice parameters were determined using another least squares refinement program called RAFD9. It takes an output file from RACER, containing the values of ω , χ , ϕ and θ for each Bragg reflection, and a file containing the initial guesses for the values of the lattice parameters a , b , c , α , β and γ . After the minimisation, the refined values for the lattice parameters are output.

5.1.6 Results

Crystal	T (K)	Wav' th (Å)	Absorption			Extinction	Multi' scatt'	Scale factor
			μ (mm ⁻¹)	A_{min}	A_{max}	E_{min}	C	S
YbNi ₂ B ₂ ¹¹ C	15	0.548	0.0440	0.87	0.98	0.78	5	5.08
		0.706	0.0490	0.86	0.98	0.73	7	5.95
		0.840	0.0550	0.83	0.97	0.71	9	6.96
ErNi ₂ B ₂ ¹¹ C	20	0.548	0.0976	0.81	0.96	0.78	1	4.14
		0.840	0.1380	0.66	0.95	0.56	3	5.90
HoNi ₂ B ₂ ¹¹ C	20	0.548	0.0512	0.89	0.98	0.81	2	4.32
		0.706	0.0610	0.85	0.97	0.58	2	5.29
		0.840	0.0694	0.83	0.97	0.55	3	6.12
LuNi ₂ B ₂ ¹¹ C	15	0.548	0.0575	0.81	0.98	0.60	6	7.71
		0.840	0.0791	0.70	0.98	0.35	18	16.44

Fig 5.7 Data concerning the absorption, extinction and multiple scattering corrections.

The above table shows the linear attenuation coefficient and the minimum and maximum absorption and extinction corrections used in the processing of all the reflections for each data set. It also gives the value of C ($= F_{exp}^2 - F_{theo}^2$, see § 5.1.5.1.2.1) and the scale factor S . For all the data sets E_{max} was equal to unity.

		YbNi ₂ B ₂ ¹¹ C	ErNi ₂ B ₂ ¹¹ C	HoNi ₂ B ₂ ¹¹ C	LuNi ₂ B ₂ ¹¹ C
R	ITF	0.098(5)	0.127(7)	0.017(8)	0.028(6)
Ni	ITF	0.094(5)	0.152(5)	0.159(6)	0.085(5)
B	ITF	0.26(1)	0.293(9)	0.27(1)	0.239(5)
	Z	0.36028(5)	0.35961(5)	0.35911(6)	0.36061(3)
	SITE	1.002(5)	0.993(5)	0.967(6)	0.981(5)
C	ITF	0.238(9)	0.234(8)	0.24(1)	0.174(6)
MOSC		0.152(3)	0.264(5)	0.316(7)	0.72(2)
χ^2		6.0	3.38	7.31	14.2

Fig 5.8 The refined sample parameters.

ITF	(\AA^2)	- Isotropic temperature parameter.
Z	(c)	- Position of the boron atom on the crystallographic c axis.
SITE		- Occupation of the boron site (unity is 100% occupation).
MOSC	(rad^{-1})	- Mosaic spread of the crystal.
χ^2 / N		- χ^2 divided by the number of data.

Refinement of the value for the crystallite radius was not possible. A value of 70 μm was used for all four crystals. The site occupation of the boron site was refined because the B^{11} isotope used in the production of the crystals contains a small amount of B^{10} . Refinements with isotropic and anisotropic temperature factors were performed; no significant differences in the success of the fit was found.

5.2 Determination of the magnetisation density in single crystals of $\text{RNi}_2\text{B}_2^{11}\text{C}$ [R = Yb, Er, Ho, Lu] using polarised elastic neutron scattering and the D3 diffractometer at the I.L.L.

5.2.1 Aims of the experiment.

This experiment was designed to look for differences in the magnetisation density associated with the rare earth site and the nickel/ boron sublattice amongst the four compounds $\text{RNi}_2\text{B}_2^{11}\text{C}$ [R = Yb, Er, Ho, Lu]. The electronic properties of these four compounds are discussed in detail in § 1.2.

The first aim of this experiment was to look for differences between the magnetisation density in the $\text{YbNi}_2\text{B}_2^{11}\text{C}$ compound below and above the Kondo temperature, measured at temperatures of 2 K and 40 K respectively. The second aim was to compare the magnetisation density in the $\text{YbNi}_2\text{B}_2^{11}\text{C}$ compound with that in the $\text{ErNi}_2\text{B}_2^{11}\text{C}$ and $\text{HoNi}_2\text{B}_2^{11}\text{C}$, to look for differences between the non-superconducting heavy fermion compound and superconducting compounds that also exhibit long range magnetic order at low temperatures. There has been a debate as to the existence of a magnetic moment on the nickel site in the superconducting nickel borocarbides [10]. This is an important issue, as the presence of a moment on this site would seem incompatible with conventional phonon mediated superconductivity and

would perhaps lend weight to the idea that magnetic fluctuation pairing or other exotic mechanisms are involved in the superconducting order in these compounds (see § 2.2.4.2). The final aim was to look at the magnetisation density associated with the nickel/ boron sublattice of the superconducting, but non magnetically ordered, compound, $\text{LuNi}_2\text{B}_2^{11}\text{C}$.

5.2.2 Sample preparation.

The single crystals used in this experiment were the same ones (necessarily) that were used in the D9 experiment (see § 5.1.2).

5.2.3 Data collection.

For each crystal, sets of flipping ratios $\{ R(\underline{\tau}) \}$ were measured using the technique described in § 3.3.2. All the data were obtained using a neutron wavelength of 0.840 Å. In order to survey a large enough region of reciprocal space, each set of flipping ratios contained data measured with the crystal in two orientations: in the first orientation, the magnetic field was approximately parallel to the [100] reciprocal lattice vector of the crystal; in the second, the field was approximately parallel to the [110] vector. As the crystals have a tetragonal unit cell, the magnitudes of $m(\underline{r})$ projected along these two crystal vectors are equal (to 1st order), and the flipping ratios obtained in each orientation could therefore be combined into a single data set. Any discrepancies between the magnitudes of the magnetic structure factors obtained from the two orientations was absorbed by a small scaling.

5.2.3.1 The $\text{YbNi}_2\text{B}_2^{11}\text{C}$ crystal.

Two sets of flipping ratios were measured at temperatures of 2 K and 40 K. These two temperatures were chosen as they lie below and above the Kondo temperature of $\text{YbNi}_2\text{B}_2^{11}\text{C}$. The applied field was 4.6 T.

5.2.3.2 The $\text{ErNi}_2\text{B}_2^{11}\text{C}$ and $\text{HoNi}_2\text{B}_2^{11}\text{C}$ crystals.

One set of flipping ratios was measured at a temperature of 20 K for each crystal. This temperature was chosen as it is above both the superconducting and magnetic ordering temperatures. Another set, measured for less time, was measured at 40 K for each crystal. These higher temperature data were needed in order to determine uniquely the magnetic structure factors from the flipping ratios (see § 5.2.5.1.3). The applied field was 4.6 T.

5.2.3.4 The $\text{LuNi}_2\text{B}_2^{11}\text{C}$ crystal.

One set of flipping ratios was measured at a temperature of 1.5 K, using an applied field of 9.2 T. The temperature and applied field were chosen to maximise the magnetic signal. Measurements at this temperature were possible as the applied field exceeded the critical field of $\text{LuNi}_2\text{B}_2^{11}\text{C}$ [11]. A full set of flipping ratios were not measured for this sample as the flipping ratios were all very close to unity and a considerable amount of time was needed to achieve convincing statistics on each reflection.

Crystal	Temperature (K)	Magnetic field (T)	Number of measured flipping ratios	Number of independent flipping ratios	Range of h	Range of k	Range of l	Range of θ ($^\circ$)
YbNi ₂ B ₂ ¹¹ C	2	4.6	531	135	-6 to 6	-4 to 5	-19 to 19	5 to 53
	40	4.6	580	136	-6 to 6	-4 to 5	-19 to 19	5 to 53
ErNi ₂ B ₂ ¹¹ C	20	4.6	357	123	-5 to 4	-6 to 6	-18 to 19	4 to 52
	40	4.6	235	123	-5 to 4	-4 to 6	-18 to 19	5 to 52
HoNi ₂ B ₂ ¹¹ C	20	4.6	737	145	-6 to 6	-4 to 5	-20 to 20	4 to 50
	40	4.6	317	145	-6 to 6	-4 to 5	-20 to 20	4 to 50
LuNi ₂ B ₂ ¹¹ C	1.5	9.2	51	17	-2 to 3	-1 to 0	-10 to 10	4 to 33

Fig 5.9 : A summary of the data collected in the D3 experiment.

5.2.4 Correction factors.

Equation 3.41 allows a set of magnetic unit cell structure factors $\{F_M(\underline{\tau})\}$ to be calculated from a set of flipping ratios $\{R(\underline{\tau})\}$. However, it must first be corrected for the following effects:

5.2.4.1 Polarisation.

The polarisation of a neutron beam is defined as

$$P = \frac{N \uparrow - N \downarrow}{N \uparrow + N \downarrow}, \quad \text{Eq 5.12}$$

where $N \uparrow$ and $N \downarrow$ are the numbers of neutrons in the spin-up and spin-down states respectively [12]. It is therefore a number between 1 (beam 100 % polarised in the spin-up state) and -1 (beam 100 % polarised in the spin-down state). Equation 3.41 gives the flipping ratio for the case where the spin-up and spin-down beams are 100 % polarised. In general, polarising monochromators and spin flippers are not perfect, and the polarisation of neutron beams is less than 100 %.

If the polarisations of the spin-up and spin-down beams are given by $P \uparrow$ ($0 < P \uparrow < 1$) and $P \downarrow$ ($-1 < P \downarrow < 0$) respectively, then equation 3.41 becomes

$$R(\underline{\tau}) = \frac{|F_N(\underline{\tau}) + \gamma r_0 F_M(\underline{\tau})|^2 (1 + P \uparrow) + |F_N(\underline{\tau}) - \gamma r_0 F_M(\underline{\tau})|^2 (1 - P \uparrow)}{|F_N(\underline{\tau}) - \gamma r_0 F_M(\underline{\tau})|^2 (1 - P \downarrow) + |F_N(\underline{\tau}) + \gamma r_0 F_M(\underline{\tau})|^2 (1 + P \downarrow)}, \quad \text{Eq 5.13}$$

where $P \downarrow$ is equal to $-P \uparrow \times E$ and E is the flipper efficiency ($0 < E < 1$).

Before this experiment, $P \uparrow$ and E were determined using two calibration samples, $\text{Co}_{0.92}\text{Fe}_{0.08}$ and Cu_2MnAl (Heusler crystal). The cobalt-iron alloy has $F_N(\underline{\tau})$ equal to $\gamma r_0 F_M(\underline{\tau})$ for the (200) reflection. If this flipping ratio is measured, then equation 5.13 gives a relation between $P \uparrow$ and E . The Heusler crystal has $F_N(\underline{\tau})$ equal to $-\gamma r_0 F_M(\underline{\tau})$ for the (111) reflection. A similar measurement gives another equation relating $P \uparrow$ and E . The two quantities can be determined by a solution of the resulting simultaneous equations [13].

5.2.4.2 Scattering vector tilt.

The above equation assumes that the scattering vector is in the xy plane (see figure 3.4, and equation 3.35). However, flipping ratios are often measured with the final neutron wavevector rotated an angle ν out of this plane. If this is taken into account, the above equation becomes

$$R(\underline{\tau}) = \frac{|F_N(\underline{\tau}) + \gamma r_0 \sin(\eta) F_M(\underline{\tau})|^2 (1 + P \uparrow) + |F_N(\underline{\tau}) - \gamma r_0 \sin(\eta) F_M(\underline{\tau})|^2 (1 - P \uparrow)}{|F_N(\underline{\tau}) - \gamma r_0 \sin(\eta) F_M(\underline{\tau})|^2 (1 - P \downarrow) + |F_N(\underline{\tau}) + \gamma r_0 \sin(\eta) F_M(\underline{\tau})|^2 (1 + P \downarrow)} \quad \text{Eq 5.14}$$

where η is the angle between the scattering vector and the direction of magnetisation (z axis) [13]

5.2.4.3 Extinction.

A description of extinction is given in § 5.1.4.2. The extinction corrections are different for the spin-up and spin-down measurements as the total scattering cross sections for the two spin states are different. If these extinction corrections are denoted by $y \uparrow$ and $y \downarrow$, then the above equation becomes

$$R(\underline{\tau}) = \frac{y \uparrow |F_N(\underline{\tau}) + \gamma r_0 \sin(\eta) F_M(\underline{\tau})|^2 (1 + P \uparrow) + y \downarrow |F_N(\underline{\tau}) - \gamma r_0 \sin(\eta) F_M(\underline{\tau})|^2 (1 - P \uparrow)}{y \downarrow |F_N(\underline{\tau}) - \gamma r_0 \sin(\eta) F_M(\underline{\tau})|^2 (1 - P \downarrow) + y \uparrow |F_N(\underline{\tau}) + \gamma r_0 \sin(\eta) F_M(\underline{\tau})|^2 (1 + P \downarrow)}$$

Eq 5.15

If the extinction correction to the nuclear structure factor, described in § 5.1.4, can be represented as $F_N^{\text{uncorr}} = F_N^{\text{corr}} \sqrt{(1 - dN)}$, then the relationship between the magnetic structure factor obtained with and without the extinction correction, described above, is $F_M^{\text{uncorr}} = F_M^{\text{corr}} \sqrt{(1 - 2dN)}$. Therefore, the extinction correction to the flipping ratios has twice the effect on the quantity of interest as compared with the extinction correction in the D9 experiment [14].

5.2.4.4 Multiple scattering.

A description of multiple scattering is given in § 5.1.4.3. The ‘Umweganregung’ transfer of intensity causes an additional contribution to the numerator and denominator of equation 5.15, causing the flipping ratio to move closer to unity. This effect is more serious for the weaker reflections and results in the magnetic structure factors being underestimated. The multiple scattering corrections used in the D9 experiment were used to make a first order correction to the magnetic structure factors obtained using equation 5.15,

$$F_M^{\text{mul}}(\underline{\tau}) = \frac{F_M^{\text{no mul}}(\underline{\tau})}{F_N^{\text{calc}}} \sqrt{(F_N^{\text{calc}})^2 + (C/S)}.$$

Eq 5.16

$F_M^{\text{noml}}(\underline{\tau})$ is the magnetic structure factor obtained from equation 5.15, $F_N^{\text{calc}}(\underline{\tau})$ is the nuclear structure factor calculated from the information obtained in the D9 experiment, C is the multiple scattering correction applied to the squares of the nuclear structure factors in the D9 experiment (see § 5.1.5.1.2.1), and S is the refined D9 scale factor. The D9 multiple scattering corrections could be used in this way, because in this experiment D3 was operating with a similar neutron wavelength and incident neutron beam divergence [15].

5.2.5 Analysis of the data.

5.2.5.1 Calculation of the magnetic unit cell structure factors from the flipping ratios.

Three C.C.S.L. programs were used to calculate the set of magnetic structure factors $\{ F_N^{\text{calc}}(\underline{\tau}) \}$ from the set of flipping ratios $\{ R(\underline{\tau}) \}$. The data processing was done using D3OP97 and ARRNGE. The calculation of the magnetic structure factors was performed by SORGAM.

5.2.5.1.1 D3OP97.

D3OP97 is the initial data processing program. It takes the raw data from the D3 computer and calculates a set of flipping ratios $\{ R(\underline{\tau}) \}$ and their standard deviations $\{ \sigma[R(\underline{\tau})] \}$, and writes these to a file. D3OP97 outputs another file that contains information concerning the orientation of the crystal with respect to the angles ω , 2θ and ν , and the polarisation of the spin up $P \uparrow$ and spin down $P \downarrow$ beams.

After D3OP97 has been executed, the output orientational and polarisation information is manually merged with the file output by SFLSQ that contains the refined nuclear structure, average crystallite radius, mosaic spread and absorption parameters (see § 5.1.5.1.4). The resulting file is used by ARRNGE and SORGAM as described below.

5.2.5.1.2 ARRNGE.

ARRNGE arranges the flipping ratios output by D3OP97 into groups that are related by the symmetry of the unit cell, and subgroups of repeated measurements, using the space group information contained in the refined parameter file prepared using D3OP97 and SFLSQ.

5.2.5.1.3 SORGAM.

SORGAM takes the output from ARRNGE and the refined parameter file, produced using D3OP97 and SFLSQ, and calculates the magnetic structure factors from the flipping ratios using equations 5.15 and 5.16. The flipping ratio is a quadratic function of the magnetic structure factor and has two solutions. For samples where the magnetic structure factors are small (i.e. magnetic structure factors \ll nuclear structure factors), the flipping ratio is close to unity, and there is no doubt in deciding which solution to accept as the magnetic structure factor as the other solution produces an unphysical answer (i.e. very large). In the case of samples with larger magnetic structure factors, this may not be the case, and additional information must be obtained. The size of a magnetic structure factor should reduce with increasing temperature as the thermal motion of the magnetic moments increases. This reduction should be proportionately the same for all the structure factors. Therefore, if the flipping ratio is measured at two temperatures, both solutions can be found at each temperature, giving four magnetic structure factors. Only one of the four ratios of low temperature to high temperature structure factors will give the correct value for the reduction of magnetic structure factor with increasing temperature. A list can then be given to SORGAM to tell it which solution of the flipping ratio equation to take to produce the final magnetic structure factors $\{ \langle F_M(\underline{\tau}) \rangle_S \}$ to be used to calculate the magnetisation density.

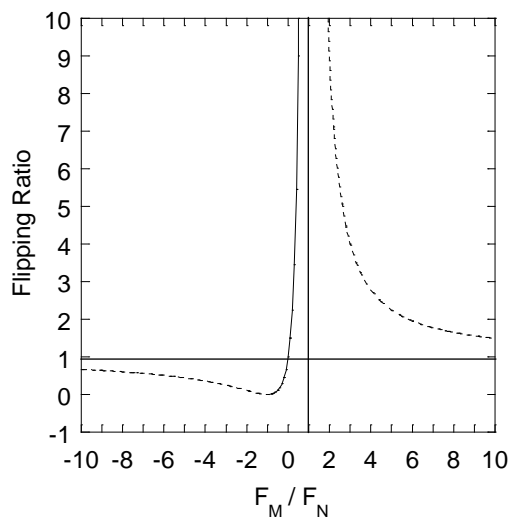


Fig 5.10 : Flipping ratio versus the ratio of the magnetic structure factor to the nuclear structure factor. The solid line (dashed) line shows the region of the graph giving the smaller (larger) magnetic structure factor for a given flipping ratio

SORGAM averages together repeated measurements of the same flipping ratio and those measurements that are related by the symmetry of the unit cell.

5.2.5.2 Calculation of the magnetisation density in the unit cell.

When the magnetic unit cell structure factors have been obtained, the calculation of the magnetisation density in the unit cell can be performed. However, this calculation is not straight forward as the data set is limited. In any experiment, the time available is finite, and this restricts the number of structure factors that can be measured, and the precision to which any one structure factor can be determined. The wavelength of the neutrons also places a limit on the range of reciprocal space that can be explored. We can consider three methods of calculating the magnetisation density: a simple Fourier transform of the structure factors, a least squares refinement to a model of the magnetisation density, and maximum entropy image reconstruction.

5.2.5.2.1 Calculation of the magnetisation density in the unit cell by performing a Fourier transform of the magnetic unit cell structure factors.

The asymmetric unit of the crystal is divided into M pixels of equal volume v_m . The magnetisation density within one of these pixels m_m is found by substituting the values of the $\{ \langle F_M(\underline{\tau}) \rangle_S \}$ obtained from SORGAM into equation 3.43. This gives

$$m_m = \frac{\mu_B}{v_a} \sum_{\underline{\tau}} \langle F_M(\underline{\tau}) \rangle_S \langle \exp(-i\underline{\tau} \cdot \underline{r}_m) \rangle_S, \quad \text{Eq 5.17}$$

where \underline{r}_m is the position vector of the centre of the pixel, and v_a is the volume of the asymmetric unit. The above equation can be used to determine the $\{m_m\}$, and construct an image of the magnetisation density in the unit cell. This method is simple, but suffers from several significant problems. All the unmeasured structure factors are implicitly set equal to zero. As the majority of unmeasured structure factors are at high q , the resulting series termination may introduce high frequency spherical ripples into the image that can make the detection of small real features difficult. Calculations to determine the errors associated with the values of the $\{m_m\}$ are difficult [16].

5.2.5.2.2 Calculation of the magnetisation density associated with each atom in the unit cell using least squares refinement.

The problems with the method described above are due to the lack of data and their Fourier nature. It would therefore be helpful to introduce some more information. This can be done by using a model to describe the magnetisation density. The technique of least squares refinement can then be used to refine this model based on the values of the $\{\langle F_M(\underline{\tau}) \rangle_S\}$ as described in § 4.3. The difference between the experimental structure factors and those calculated from the refined model can be taken. A Fourier transform of these difference structure factors can be made. The resulting difference image suffers much less from the effects of series termination as the unmeasured difference structure factors should have a value of zero.

If the electrons are thought to be localised around the positions of the nuclei, the model described in § 3.3.2 can be used.

In this experiment, MPLSQ (a modification of the program SFLSQ used in the D9 experiment) was used for the least squares refinement. The experimental data

$$\{D_{n=1}^N\} = \left\{ \langle F_M(\underline{\tau}) \rangle_S \right\}, \quad \text{Eq 5.18}$$

and their standard deviations

$$\{\sigma_{n=1}^N\} = \left\{ \sigma \left[\langle F_M(\underline{\tau}) \rangle_S \right] \right\}, \quad \text{Eq 5.19}$$

are output from SORGAM. The theoretically generated data are given by

$$\{F_{n=1}^N\} = \left\{ \langle F_M(\underline{\tau}) \rangle_S^{\text{calc}} \right\} = \left\{ \sum_d \sum_l \sum_{m=-l}^l a_{dlm} \langle F_{dlm}(\underline{\tau}) \exp(i\underline{\tau} \cdot \underline{d}) \exp(-W_d) \rangle_S \right\}, \quad \text{Eq 5.20}$$

where the adjustable sample parameters in the least squares refinement are the

$$\{X_{m=1}^M\} = \{a_{dlm}\}, \quad \text{Eq 5.21}$$

where a_{dlm} is the magnitude of the angular momentum operator associated with the unpaired electrons in the lm^{th} wavefunction of the d^{th} atom in the unit cell. In a refinement, the smallest number of the $\{a_{dlm}\}$ are used that are needed to give a satisfactory agreement between the experimental and theoretically generated data. Apart from the experimentally determined magnetic structure factors, MPLSQ requires an input file containing the initial guesses for the values of the $\{a_{dlm}\}$.

Equations 5.18, 5.19, 5.20 and 5.21 can be substituted into equation 4.10 to give the probability density function for the sample parameters

$$\text{prob}\left(\{a_{dlm}\} \middle| \left\{ \langle F_M(\underline{\tau}) \rangle_S \right\}, I\right) = C \times \exp - \sum_{n=1}^N \left[\frac{\left[\left(\sum_d \sum_l \sum_{m=-l}^l a_{dlm} \langle F_{dlm}(\underline{\tau}) \exp(i\underline{\tau} \cdot \underline{d}) \exp(-W_d) \rangle_S \right)_n - \left(\langle F_M(\underline{\tau}) \rangle_S \right)_n \right]^2}{\left[\sigma_n \left[\langle F_M(\underline{\tau}) \rangle_S \right] \right]^2} \right].$$

Eq 5.22

MPLSQ maximises this function to obtain the most probable values for the sample parameters $\{a_{dlm0}\}$. After the refinement, MPLSQ changes the values of the sample parameters to their most probable values. An additional file is output that contains information concerning the success of the refinement, similar to the file output by SFSLQ in the D9 refinement.

The magnetisation density associated with the d^{th} atom is given by the Fourier transform of the normalised form factors used to model that atom $\{F_{dlm}(\underline{\tau})\}$, scaled by the refined values of the angular momentum operator magnitudes $\{a_{dlm0}\}$. The total magnetic moment associated with the d^{th} atom is given by

$$\mu_d = -2\mu_B \sum_l \sum_{m=-l}^l a_{dlm}.$$

Eq 5.23

This method does not suffer to the same extent from the problems associated with the simple Fourier transform method [16]. The standard deviations associated with the $\{a_{dlm0}\}$ can be calculated from the probability density function. However, in many problems, the reason for performing a magnetisation density experiment is to help determine a model for the electronic structure of the sample, and if the electrons are thought to be delocalised the above atom centred model is of limited use.

5.2.5.2.3 Calculation of the magnetisation density in the unit cell using maximum entropy image reconstruction.

The maximum entropy image reconstruction in this thesis was performed using software written by A. J. Markvardsen [17]. The principle of maximum entropy with respect to image construction was outlined in § 4.4. In this context, it allows the calculation of the magnetisation density in the unit cell without an *a priori* theoretical model. However, the entropy constraint means that it does not suffer from the introduction of noise to the same extent as the simple Fourier transform method. It also allows the standard deviations of particular features in the resulting image to be calculated more easily from the resulting probability density function.

The data $\{D_{n=1}^N\}$ and their standard deviations $\{\sigma_{n=1}^N\}$ are as given for the least squares refinement. The theoretically generated data are given by

$$\{F_{n=1}^N\} = \left\{ \langle F_M(\underline{r}) \rangle_S^{\text{calc}} \right\} = \left\{ \frac{\nu_m}{\mu_B} \sum_{\text{asym unit}, m=1}^M \langle \exp(i\underline{r} \cdot \underline{r}_m) \rangle_S (m_m \uparrow - m_m \downarrow) \right\}, \quad \text{Eq 5.24}$$

where $m_m \uparrow$ and $m_m \downarrow$ are the positive and negative magnetisation densities in the m^{th} pixel, and the sum is over the M pixels in the asymmetric unit. The Shannon-Jaynes entropy is given by

$$S(\{m_m\}) = - \sum_{\text{asym unit}, m=1}^M \left(m_m \uparrow \ln \left[\frac{m_m \uparrow}{m_{mg} \uparrow} \right] + m_m \downarrow \ln \left[\frac{m_m \downarrow}{m_{mg} \downarrow} \right] \right), \quad \text{Eq 5.25}$$

The magnetisation density is split into separate positive and negative images because the logarithmic nature of the single entropy term in the simple formalism outlined in § 4.4 is only capable of producing positive images. This method of producing images containing positive and negative regions was first used in the analysis of nuclear spin density in N.M.R. experiments [18]. It follows that the posterior probability density function for the magnetisation density is

$$\text{prob}\left(\{m_m\} \left| \left\{ \langle F_M(\underline{r}) \rangle_S \right\}, I \right) = C \times \exp \left\{ ES(\{m_m\}) - \sum_{n=1}^N \left(\frac{\left[\left(\langle F_M(\underline{r}) \rangle_S^{\text{calc}} \right)_n - \left(\langle F_M(\underline{r}) \rangle_S \right)_n \right]^2}{\left[\sigma_n \left[\langle F_M(\underline{r}) \rangle_S \right] \right]^2} \right) \right\}. \quad \text{Eq 5.26}$$

Although a rigid model is not required, there are two *a priori* parameters that must be decided upon before the maximisation procedure can take place. The first parameter, E , gives a weighting between the entropy term and the least squares term. Sophisticated methods exist for determining its value based on the covariance matrix of the posterior probability density function [19]. However, Markvardsen uses a simpler approach. He chooses E such that $\chi^2 \approx N$ at the end of maximisation process. This was found to be satisfactory for data of high quality as small variations from this criterion do not change the resulting image significantly [17]. The second parameter, $m_{mg} = m_{mg} \uparrow -m_{mg} \downarrow$, determines the initial average magnetisation density in each pixel in the image. A method for finding a suitable value for this parameter has been determined by Markvardsen:

The maximisation is performed many times with different values for m_{mg} . For each maximisation, the resulting average magnetisation density, \bar{m} , can be calculated. For small values of $m_{mg} \ll \bar{m}$, the calculated values of the magnetic structure factors that have not been experimentally measured (usually high q) are much less than an extrapolation of the experimentally determined data would suggest. This situation is similar to the one encountered in the Fourier transform analysis of the data (see § 5.2.5.2.1). For values of $m_{mg} \gg \bar{m}$, these calculated values are higher than an extrapolation of the experimental data. A value of $m_{mg} \sim \bar{m} / 4$, causes the calculated structure factors that have not been experimentally determined to be close to the values that would be obtained by extrapolating the experimental data. This is found to be the case in all the magnetisation images that have been produced using the Markvardsen algorithm to date. Therefore, the most reliable maximum entropy constructions are thought to be produced starting with a value for m_{mg} of $\bar{m} / 4$ [17].

The values of *a priori* parameters should be quoted with the results of all data analysis techniques. This is especially true of techniques, such as maximum entropy, where the prior information has a complex relationship with its effect on the resulting image.

5.2.6 Results.

Assuming a simple model, with spherical magnetisation density on the rare earth, nickel, boron and carbon sites, the calculated contributions to all the observable magnetic structure factors of $\text{RNi}_2\text{B}_2^{11}\text{C}$ (up to a Q of $\sim 12.5 \text{ \AA}^{-1}$) are shown in fig 5.11. Approximately 60 % of the magnetic structure factors contain contributions from all the atomic sites and the remaining structure factors have contributions from the rare earth, boron and carbon sites only.

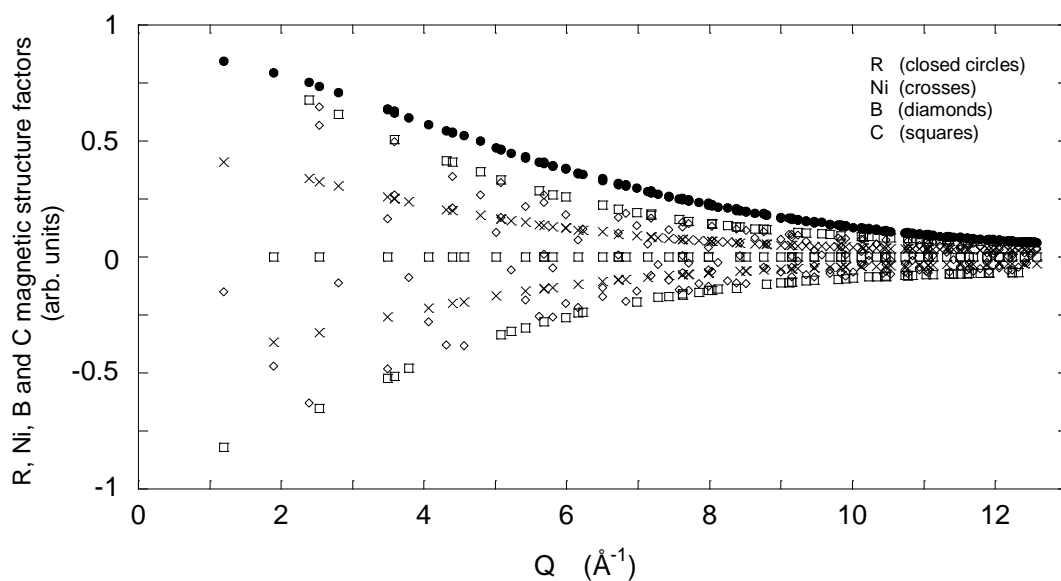


Fig 5.11 : The calculated contributions to the magnetic structure factors of $\text{RNi}_2\text{B}_2^{11}\text{C}$ from each site. The relative magnitudes of the structure factors from different sites are on an arbitrary relative scale. This scale varies significantly amongst the compounds. In general, the rare earth structure factors are very much larger than the others.

The contribution from the rare earth site to an individual structure factor is always positive but the nickel, boron and carbon contributions may be positive or negative [20].

For the $\text{YbNi}_2\text{B}_2^{11}\text{C}$ and $\text{LuNi}_2\text{B}_2^{11}\text{C}$ samples, all the measured flipping ratios were close to unity. Therefore, there was no difficulty in unambiguously assigning the magnetic structure factors from the flipping ratios. For the $\text{ErNi}_2\text{B}_2^{11}\text{C}$ and $\text{HoNi}_2\text{B}_2^{11}\text{C}$ samples, many flipping ratios were much larger or smaller than unity. In these cases, the method outlined in § 5.2.5.1.3 was used to determine the correct solution of the flipping ratio equation.

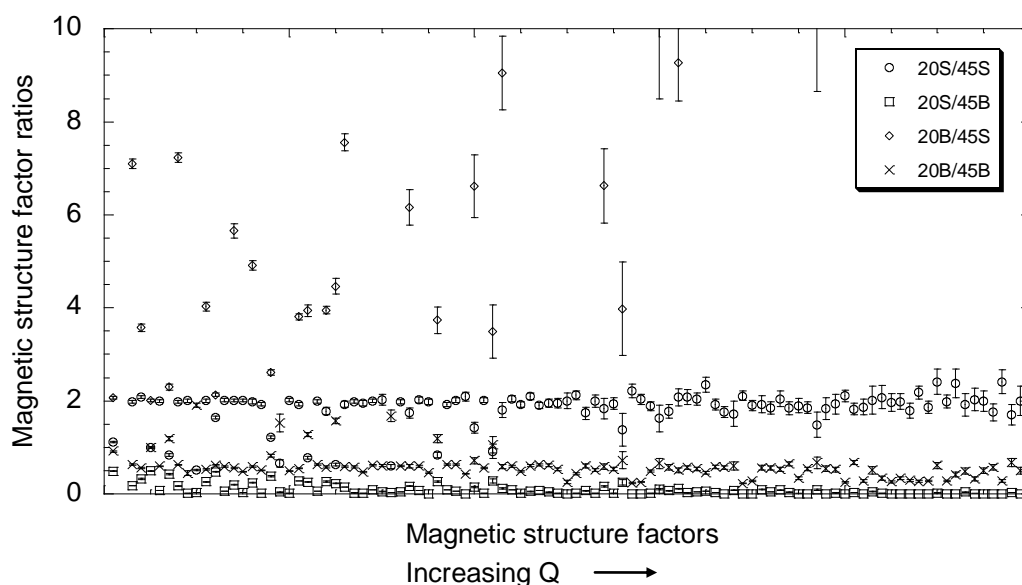


Fig 5.12 : The ratios of the magnetic structure factors obtained from the flipping ratio equation at temperatures of 20 K and 45 K for $\text{ErNi}_2\text{B}_2^{11}\text{C}$. *S* and *B* denote magnetic structure factors obtained using the smaller and larger root of the flipping ratio equation respectively.

It can be seen from figure 5.12 that the correct value for the ratio of the low temperature to high temperature magnetic structure factor for the $\text{ErNi}_2\text{B}_2^{11}\text{C}$ data is ~ 2 . Using this plot, and a similar one for the $\text{HoNi}_2\text{B}_2^{11}\text{C}$ sample, magnetic structure factors were discarded from each data set where none of the ratios of low temperature to high temperature structure factors were near the obvious modal value.

The SORGAM program corrects the structure factors for polarisation, absorption, extinction and multiple scattering. In order to see the relative sizes of the changes to the structure factors from each of these corrections, the above procedure was used to produce four sets of structure factors that each contained only one of the corrections. The following figure provides a typical example of the relative contributions to the magnetic structure factors from each of the corrections for all four crystals:

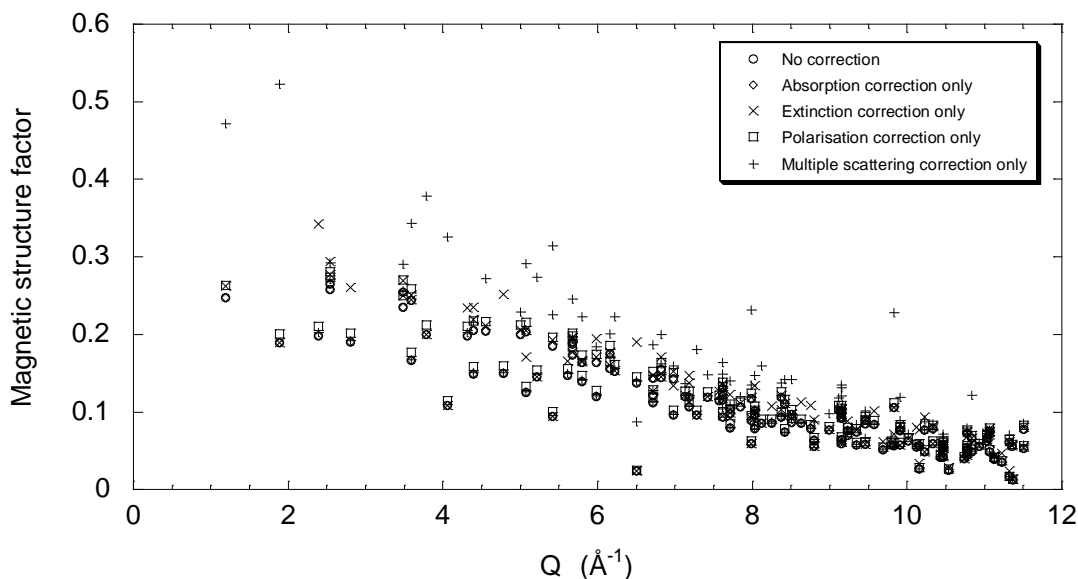


Fig 5.14 : Magnetic structure factors for $\text{YbNi}_2\text{B}_2^{11}\text{C}$ output from SORGAM with different corrections (the multiple scattering correction shown here is equivalent to the D9 correction).

It can be seen from the above plot that the multiple scattering correction has a much larger effect than the other corrections. The correction is proportionately larger for those reflections with small nuclear structure factors. Unfortunately, there is a fair degree of uncertainty about the size of the multiple scattering corrections to be made to the structure factors for all four crystals. The D9 multiple scattering corrections on which the D3 corrections are based are determined from graphs similar to the one shown in fig 5.5. It is obvious from this graph that there is a significant error associated with the determination of C . Also, although similar, the neutron wavelength and incident neutron beam divergence of D9 and D3 are not exactly the same. As this correction is large and there is uncertainty as to its magnitude, its effect

on the resulting magnetisation density maps of the compounds must be studied very carefully.

For each compound, five sets of magnetic structure factors were produced with a multiple scattering correction of 0, 0.5, 1, 1.5 and 2 times the D9 correction. The magnetisation density was calculated from these structure factors using the least squares refinement and maximum entropy methods described above. In the least squares refinement, initially, the magnetisation density on each site was modelled only with their F_{00} form factors. The higher order anisotropic form factors were then introduced to determine if they produced better agreement between experimental and theoretical structure factors. After this had been completed, the ytterbium and erbium sites were modelled with the F_{00} and F_{44} form factors and the holmium site was modelled using the F_{00} , F_{40} , F_{60} and F_{64} form factors. The lutetium site was modelled with the F_{00} form factor only. The nickel, boron and carbon sites in all the compounds were modelled with the F_{00} form factor only. The maximum entropy image construction for each set of structure factors was performed as described in § 5.2.5.2.3

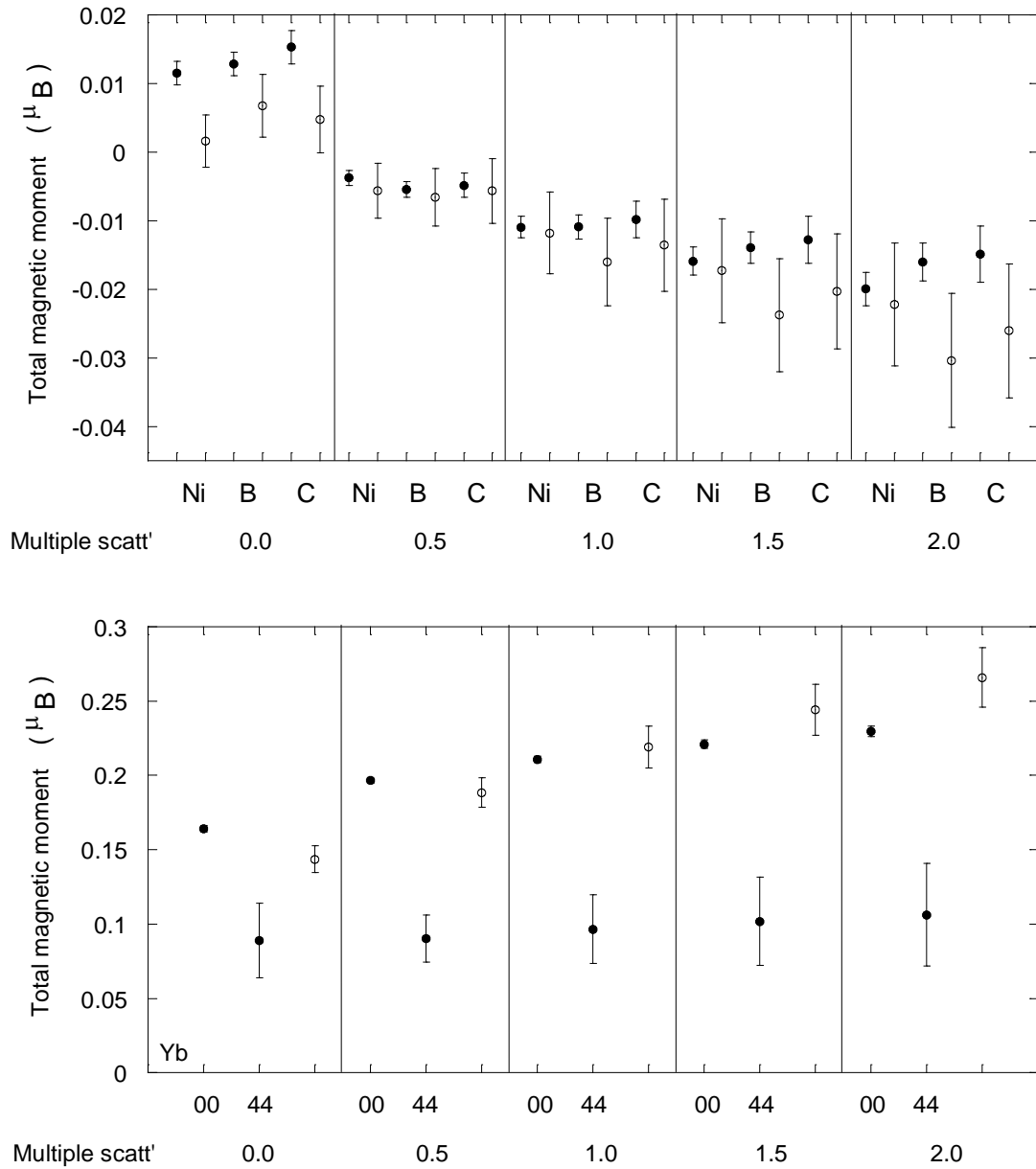


Fig 5.15 :

Total magnetic moments of the Yb, Ni, B and C sites of $\text{YbNi}_2\text{B}_2^{11}\text{C}$ at 2 K for multiple scattering corrections of 0.0, 0.5, 1.5 and 2.0 times the D9 correction. Closed (open) circles are data determined by least squares refinement (maximum entropy image construction). The F_{00} and F_{44} form factors are used for the Yb site least squares refinement and the F_{00} form factors are used for the Ni, B and C sites. The maximum entropy *a priori* parameters are $m_{mg} = 0.845 \mu_B$ and $\chi^2 = 135$ after maximisation has finished.

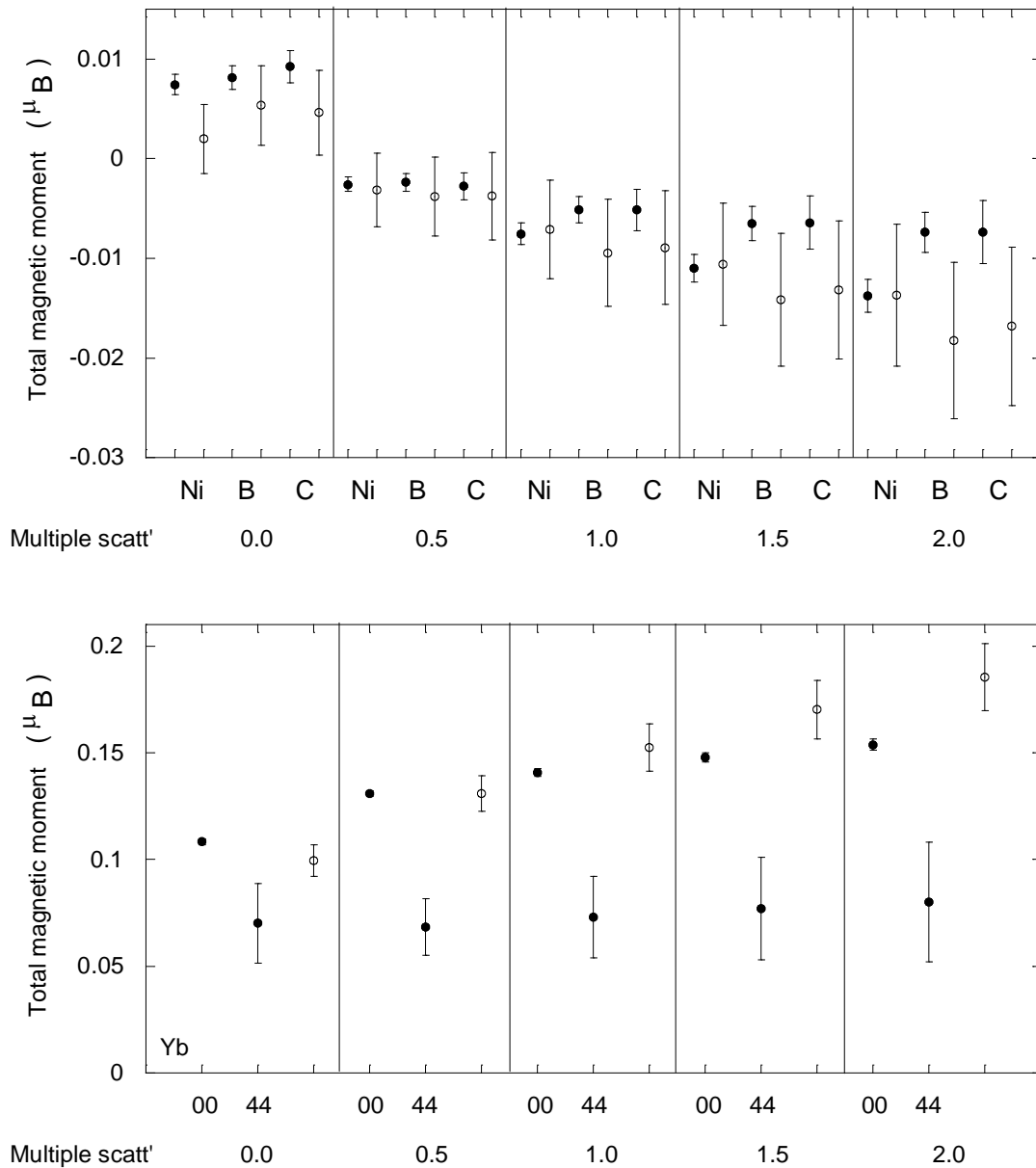


Fig 5.16 :

Total magnetic moments of the Yb, Ni, B and C sites of $\text{YbNi}_2\text{B}_2^{11}\text{C}$ at 40 K for multiple scattering corrections of 0.0, 0.5, 1.5 and 2.0 times the D9 correction. Closed (open) circles are data determined by least squares refinement (maximum entropy image construction). The F_{00} and F_{44} form factors are used for the Yb site least squares refinement and the F_{00} form factors are used for the Ni, B and C sites. The maximum entropy *a priori* parameters are $m_{mg} = 0.507 \mu_B$ and $\chi^2 = 136$ after maximisation has finished.

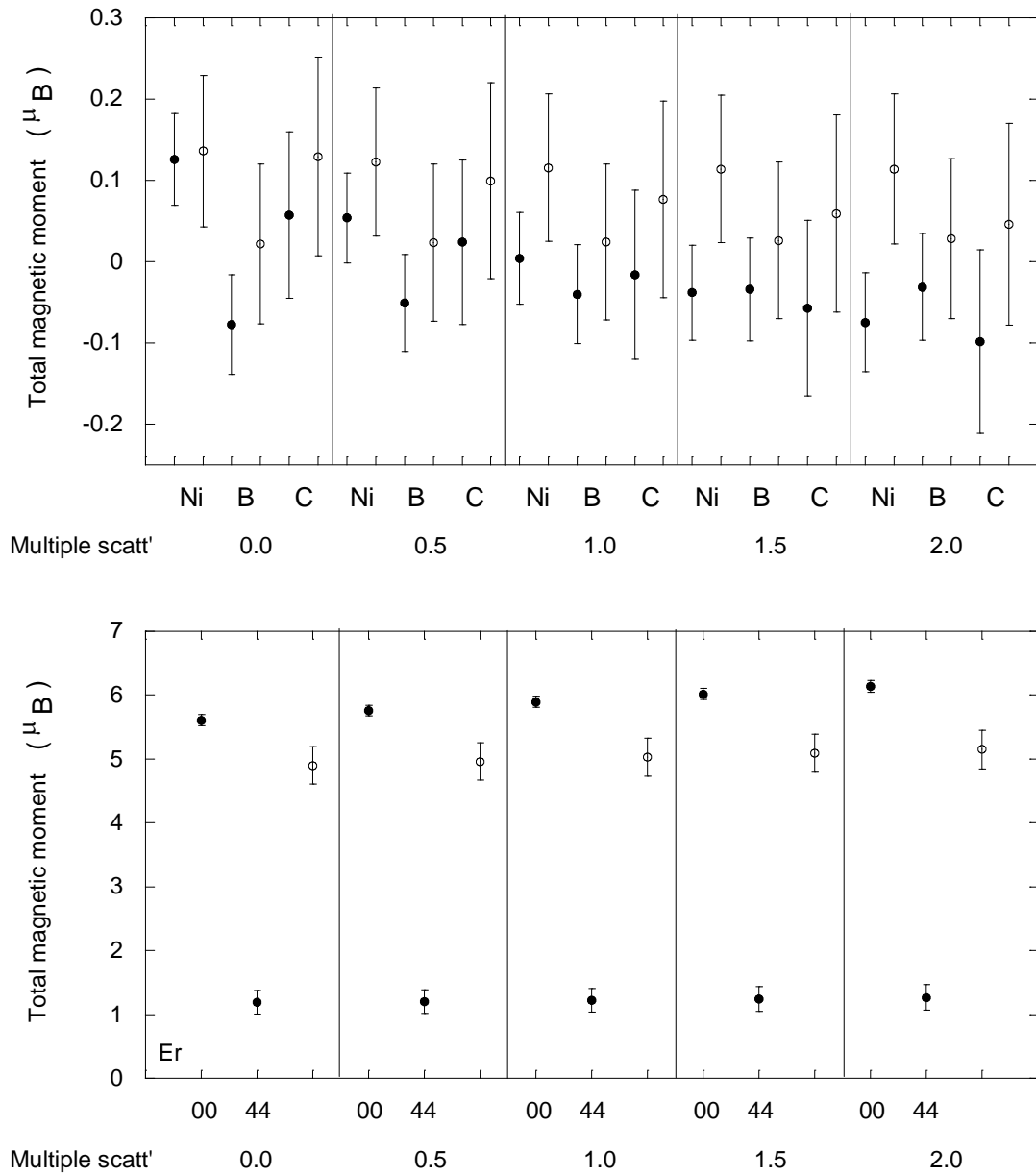


Fig 5.17 :

Total magnetic moments of the Er, Ni, B and C sites of $\text{ErNi}_2\text{B}_2^{11}\text{C}$ at 20 K for multiple scattering corrections of 0.0, 0.5, 1.5 and 2.0 times the D9 correction. Closed (open) circles are data determined by least squares refinement (maximum entropy image construction). The F_{00} and F_{44} form factors are used for the Er site least squares refinement and the F_{00} form factors are used for the Ni, B and C sites. The maximum entropy *a priori* parameters are $m_{mg} = 12.468 \mu_B$ and $\chi^2 = 123$ after maximisation has finished.

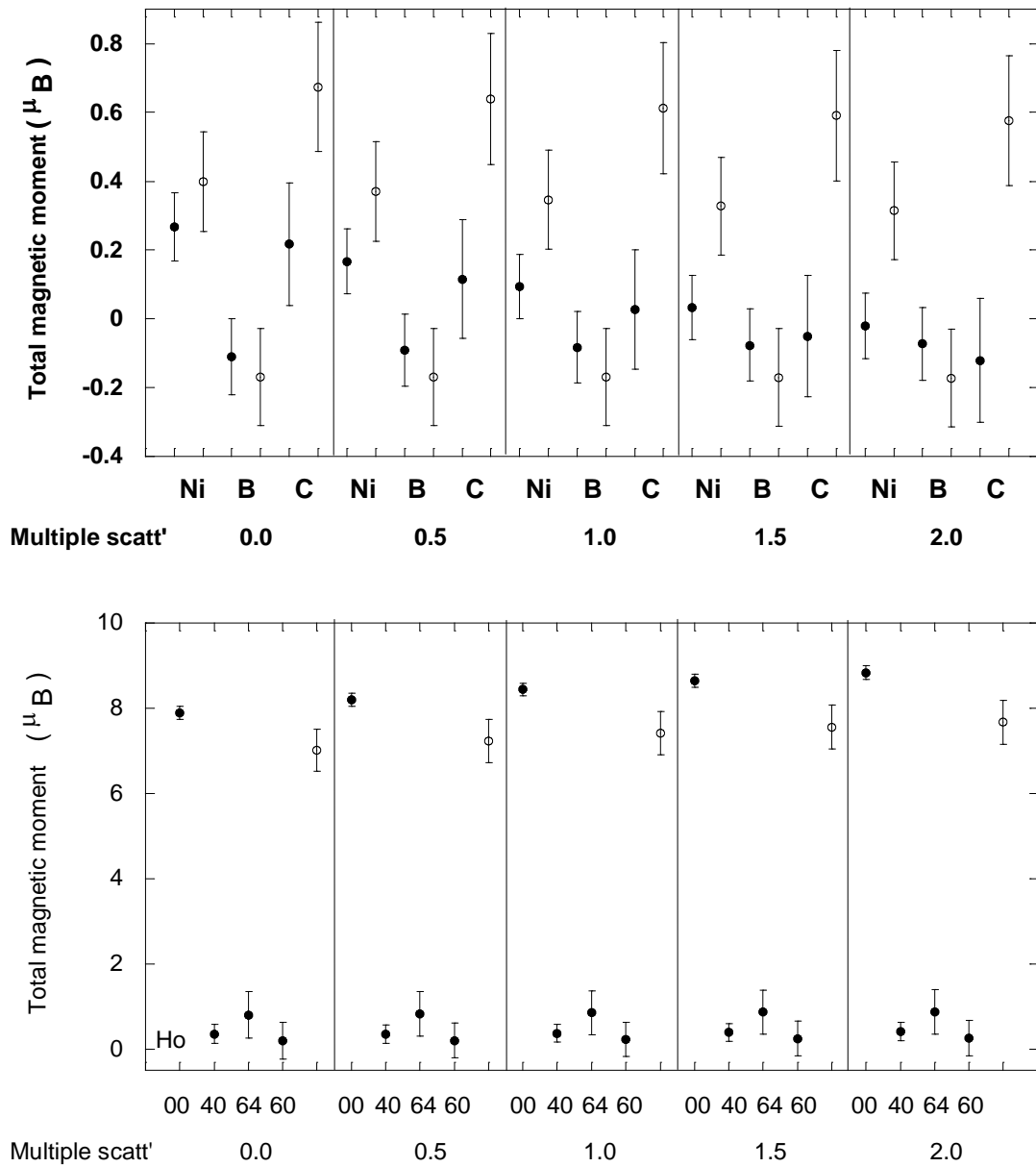


Fig 5.18 :

Total magnetic moments of the Ho, Ni, B and C sites of $\text{HoNi}_2\text{B}_2^{11}\text{C}$ at 20 K for multiple scattering corrections of 0.0, 0.5, 1.5 and 2.0 times the D9 correction. Closed (open) circles are data determined by least squares refinement (maximum entropy image construction). The F_{00} , F_{40} , F_{60} and F_{64} form factors are used for the Ho site least squares refinement and the F_{00} form factors are used for the Ni, B and C sites. The maximum entropy *a priori* parameters are $m_{mg} = 15.123 \mu_B$ and $\chi^2 = 145$ after maximisation has finished.

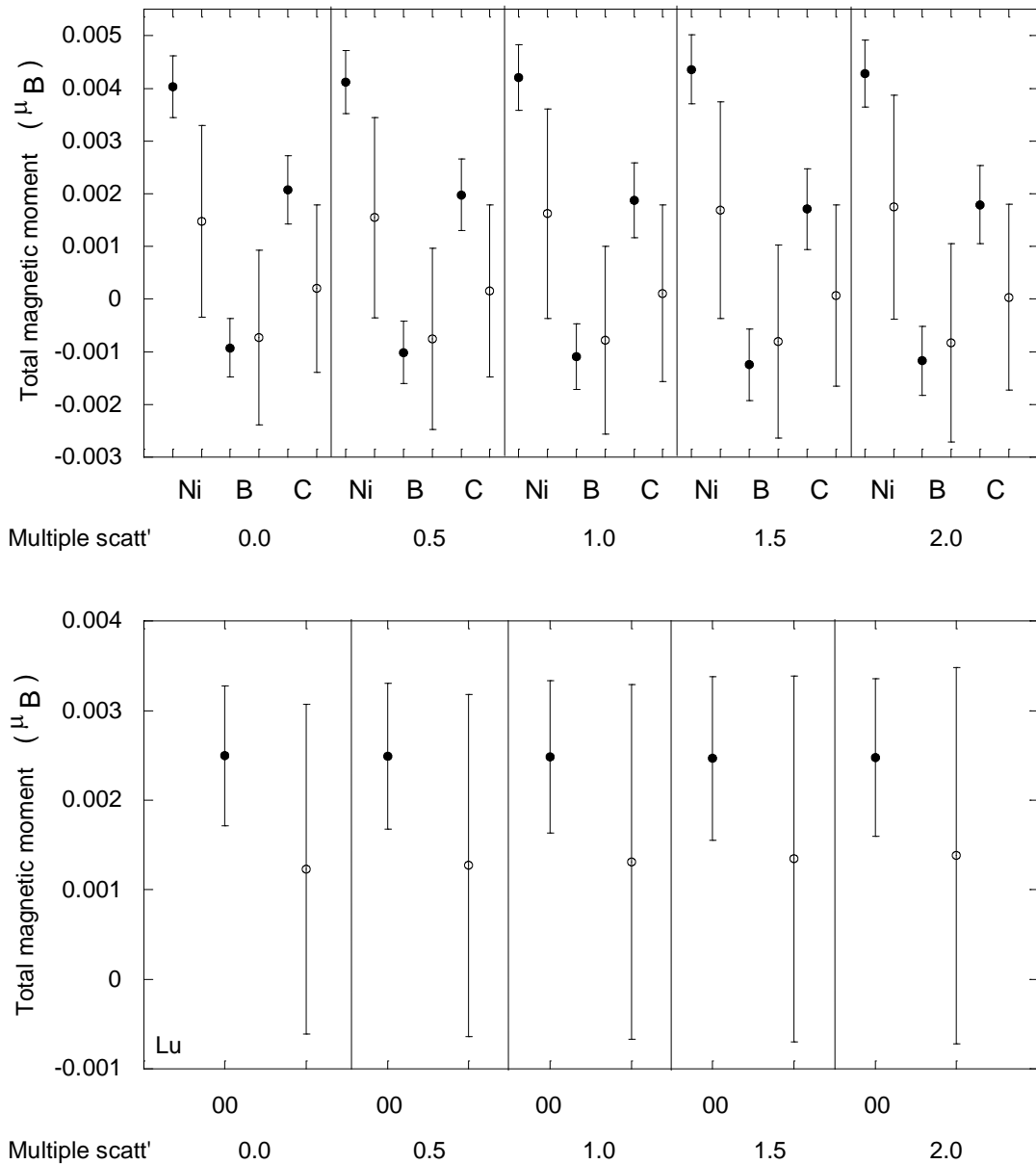


Fig 5.19 :

Total magnetic moments of the Lu, Ni, B and C sites of $\text{LuNi}_2\text{B}_2^{11}\text{C}$ at 1.5 K for multiple scattering corrections of 0.0, 0.5, 1.5 and 2.0 times the D9 correction. Closed (open) circles are data determined by least squares refinement (maximum entropy image construction). The F_{00} form factors are used for all sites in the least squares refinement. The maximum entropy *a priori* parameters are $m_{mg} = 0.0234 \mu_B$ and $\chi^2 = 17$ after maximisation has finished.

The above graphs show the values of the total magnetic moments on the rare earth, nickel, boron and carbon sites for the four compounds. In all compounds, the error bars are larger for the maximum entropy refinement. This is a reflection of the fact that the least squares refinement employs a larger amount of prior knowledge concerning the distribution of the magnetisation density. In general, there is fairly good agreement between the total magnetic moments determined from the least squares and the maximum entropy methods. The agreement is worst for the $\text{LuNi}_2\text{B}_2^{11}\text{C}$ compound, which is not surprising as only 17 independent structure factors were measured for this compound.

Fig 5.15 shows the magnetic moments of the sites in $\text{YbNi}_2\text{B}_2^{11}\text{C}$ at 2 K, which is below the reported value of T_K . One of the main aims of this experiment was to study the effect of heavy fermion behaviour on the magnetisation density of this compound, particularly to look for signs of hybridisation between the ytterbium sites and the nickel/ boron sublattice. Unfortunately, the multiple scattering correction has a large effect on the magnetisation density in this compound. The effects of this correction can be seen in fig 5.15; as the size of the correction increases, positive magnetisation density is transferred from the Ni, B and C sites to the Yb site. The signs of the Ni, B and C magnetic moments consequently change from positive to negative. As mentioned above, a determination of the exact multiple scattering correction to be used is extremely difficult with the information obtained in this experiment. However, the data presented in fig 5.15 does perhaps provide some clues as to the magnitude of the correction. Theoretically, the magnetic moment on the boron and carbon sites should be zero. Therefore, it would be sensible to assume the multiple scattering correction is 0.4 times the D9 correction as this value leads to a moment of zero on both of these sites. As the nickel moment, with all corrections, is close to the value of the boron and carbon moments, it follows that the nickel moment will also be zero with this multiple scattering correction. Further evidence that this is an appropriate correction to make comes from the fact that the value of χ^2 in the least squares refinement passes through a minimum at a value of 0.4 times the normalised D9 correction. This method of determining the correction (by comparing theoretical and experimental structure factors) is similar to the method employed in the D9

experiment (see § 5.1.5.1.2.1). Therefore, the data suggests that the Ni moment in this compound at 2 K is either zero or has a small finite positive or negative magnetic moment which has a magnitude below the resolution of this experiment.

Another aim of this experiment was to compare the magnetisation density of the $\text{YbNi}_2\text{B}_2^{11}\text{C}$ compound at temperatures of 2 K and 40 K. The higher temperature data are presented in fig 5.16. The magnitude of the ytterbium magnetic moment has reduced to ~ 0.6 of its 2 K value. The magnetic moments of the nickel, boron and carbon sites display very similar behaviour to the 2 K data with increasing multiple scattering correction. Their magnitudes are also broadly similar to the lower temperature data. Therefore, the same conclusion can be reached regarding this data as was reached for the 2 K data. It is most likely that the magnetic moments of the nickel, boron and carbon sites are very close or equal to zero. Therefore, there is no evidence of substantial changes in magnetic moment of the nickel site on moving to temperatures below T_K .

The data for the $\text{ErNi}_2\text{B}_2^{11}\text{C}$ and $\text{HoNi}_2\text{B}_2^{11}\text{C}$ compounds, are presented in figs 5.17 and 5.18. The magnetic moments of the nickel, boron and carbon sites, for both compounds, and for all the multiple scattering corrections shown, are indistinguishable (or close to indistinguishable) from zero within experimental error. The large errors associated with these moments are due to the proximity of the nickel, boron and carbon sites to the very much larger magnetic moments of the rare earth ions in these compounds.

The data for the $\text{LuNi}_2\text{B}_2^{11}\text{C}$ compound is presented in fig 5.19. The least squares refinement suggests the existence of small moments on the nickel, boron and carbon sites. The analogous data from the maximum entropy processing suggest that the errors are too large to distinguish all the moments from zero; also, the magnitudes of the moments are smaller by a factor of ~ 2 . As only 17 independent structure factors were measured for this compound, it is probably unwise to draw any firm conclusions from this data.

This experiment was also designed to look at the rare earth magnetisation density in the $\text{YbNi}_2\text{B}_2^{11}\text{C}$, $\text{ErNi}_2\text{B}_2^{11}\text{C}$ and $\text{HoNi}_2\text{B}_2^{11}\text{C}$ compounds. In the least squares refinement, the ytterbium and erbium magnetisation densities were modelled with their F_{00} and F_{44} form factors, as these gave the best agreement between experimental and theoretical structure factors. Likewise, the F_{00} , F_{40} , F_{60} and F_{64} form factors were used to model the magnetisation density of the holmium site.

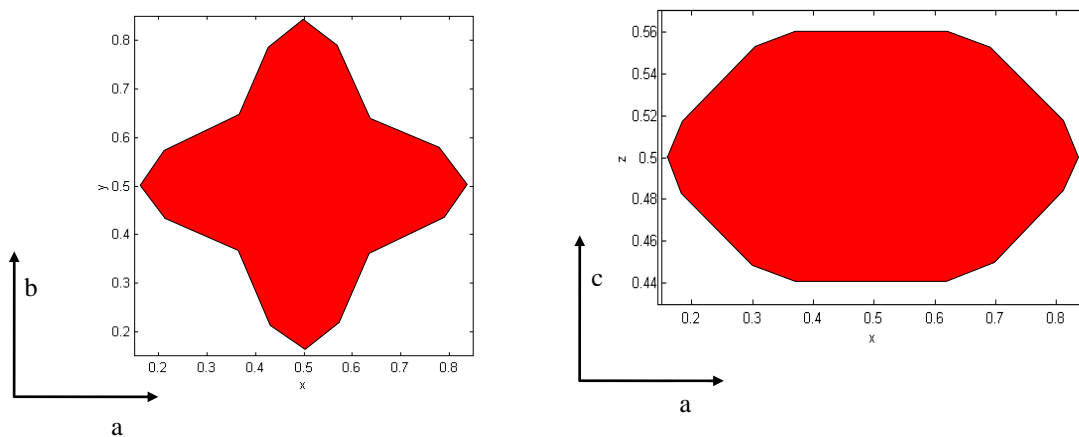


Fig 5.20 :

Magnetisation density contour at $0.007 \mu_B / (0.1 \text{ nm})^3$ of the Yb site in $\text{YbNi}_2\text{B}_2^{11}\text{C}$ at 2 K obtained using maximum entropy image construction (*a priori* parameters are $m_{mg} = 0.845 \mu_B$ and $\chi^2 = 135$ after maximisation has been completed).

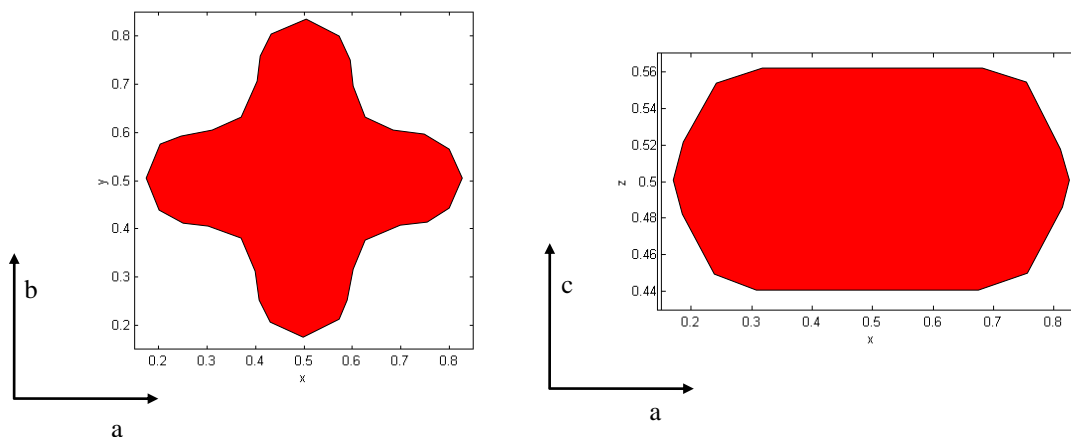


Fig 5.21 :

Magnetisation density contour at $0.004 \mu_B / (0.1 \text{ nm})^3$ of the Yb site in $\text{YbNi}_2\text{B}_{11}\text{C}$ at 40 K obtained using maximum entropy image construction (*a priori* parameters are $m_{mg} = 0.507 \mu_B$ and $\chi^2 = 136$ after maximisation has been completed).

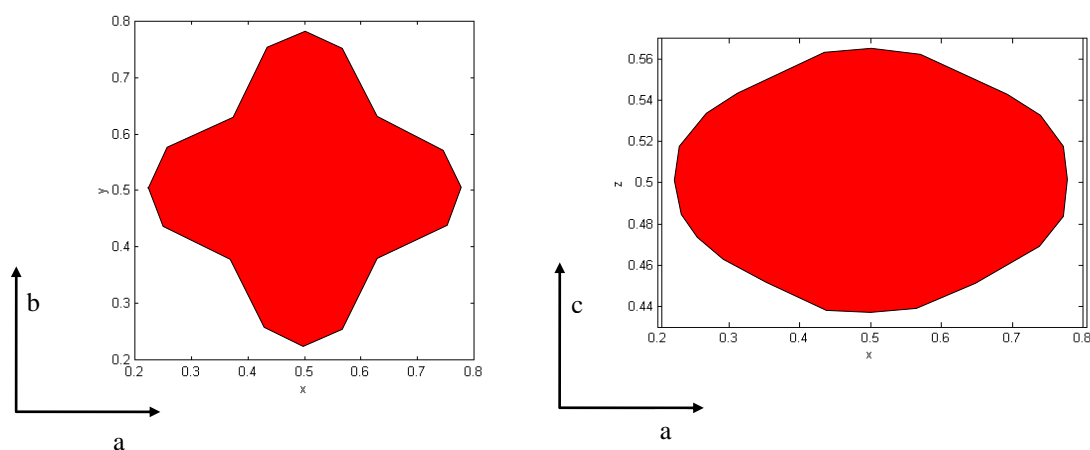


Fig 5.22 :

Magnetisation density contour at $0.084 \mu_B / (0.1 \text{ nm})^3$ of the Er site in $\text{ErNi}_2\text{B}_{11}\text{C}$ at 20 K obtained using maximum entropy image construction (*a priori* parameters are $m_{mg} = 12.468 \mu_B$ and $\chi^2 = 123$ after maximisation has been completed).

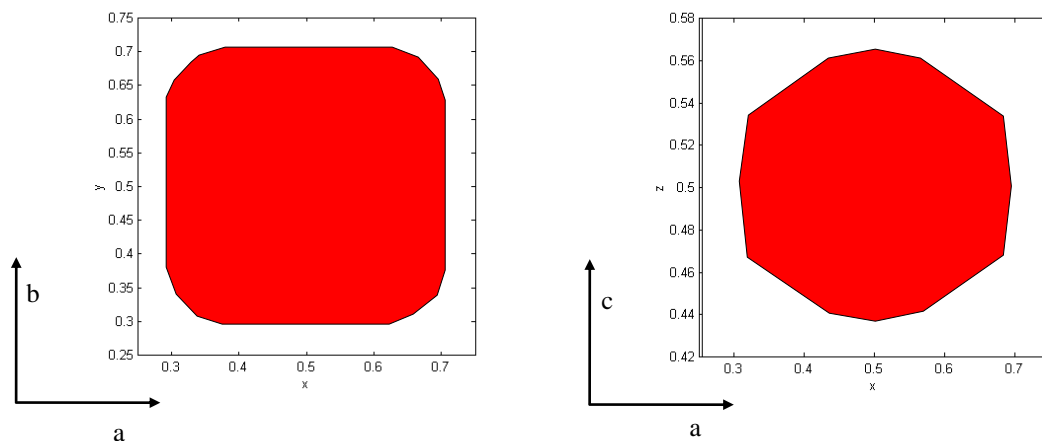


Fig 5.23 :

Magnetisation density contour at $0.105 \mu_B / (0.1 \text{ nm})^3$ of the Ho site in $\text{HoNi}_2\text{B}_2\text{C}$ at 20 K obtained using maximum entropy image construction (*a priori* parameters are $m_{mg} = 15.123 \mu_B$ and $\chi^2 = 145$ after maximisation has been completed).

It was thought that there might be a significant qualitative difference in the magnetisation density of the Yb site in $\text{YbNi}_2\text{B}_2\text{C}$ measured at 2 K and 40 K, perhaps as the result of hybridisation of the $4f$ electrons and those of the nickel/ boron sublattice in the heavy fermion state. However, as is shown in figs 5.20 and 5.21, the general shape and anisotropy of the magnetisation density is the same at both temperatures. It was also thought that there may be significant differences between the Yb magnetisation density and the magnetisation density of the rare earth ions in the compounds that display long range magnetic order and superconductivity ($R = [\text{Er}, \text{Ho}]$). There is a significant difference between the Yb magnetisation density and the Ho magnetisation density. Unfortunately, the Yb and Er magnetisation densities are very similar. This would suggest that the two forms of rare earth magnetisation density do not correspond to a particular type of correlated electron behaviour. These general conclusions concerning the anisotropy of the rare earth magnetisation density are not effected by the size of the multiple scattering correction chosen.

Before this experiment was performed, it was thought that the heavy fermion hybridisation in $\text{YbNi}_2\text{B}_2\text{C}$ might result in measurable magnetisation density in between the rare earth ions and the nickel/ boron sublattice; this was not observed. In

general, in all four compounds, there was no inter-site magnetisation density that had a value larger than its standard deviation.

These results will be discussed further in chapter 7. Some suggestions for further work to improve the measurement of the magnetisation density in these compounds will also be given.

5.3 Search for magnetic order in a single crystal sample of $\text{YbNi}_2\text{B}_2^{11}\text{C}$ using elastic neutron scattering and the D10 diffractometer at the I.L.L.

5.3.1 The D10 diffractometer.

The general operating principle of the D10 diffractometer, when used in the standard four-circle configuration, is similar to that described for the D9 diffractometer (see § 3.3.1). D10 operates with thermal neutrons, and the relatively high flux and low background make it ideal for searching for and studying weak diffuse scattering and incommensurate magnetic order with small magnetic moments. The Eulerian cradle on D10 may be fitted with a dilution fridge enabling the sample to be cooled to ~30 mK [21].

5.3.2 Aims of the experiment.

Measurements of specific heat capacity, resistivity and magnetic susceptibility in $\text{YbNi}_2\text{B}_2\text{C}$ have been made down to temperatures of 0.3 K. No indication of long range magnetic order has been found. Neutron powder diffraction measurements have also been made but no magnetic Bragg peaks were observed [22]. Other measurement techniques, such as NMR, that would be sensitive to ordering of the Yb moments have not been extended below 1.5 K [23]. Often, magnetic ordering is difficult to observe in heavy fermion compounds. This is because the $4/5f$ magnetic moments may be substantially reduced by the formation of antiferromagnetic correlations with the surrounding conduction electrons. Also, if the ordering is short range or two dimensional, then one would not expect to observe a sharp anomaly in the bulk properties. For example, in heavy fermion UPt_3 , antiferromagnetic order was

discovered by single crystal neutron diffraction and an unusually small ordered moment of $0.02 \mu_B$ was found that has not been observed by any other technique. The formation of a magnetically ordered state has been observed in other Yb heavy fermion compounds [24].

The aim of this experiment was to search for magnetic order in a single crystal sample of $\text{YbNi}_2\text{B}_2^{11}\text{C}$. The use of a single crystal and the D10 diffractometer meant that this experiment was much more sensitive to magnetic Bragg scattering than the previously performed polycrystalline neutron diffraction study.

5.3.3 Sample preparation.

The $\text{YbNi}_2\text{B}_2^{11}\text{C}$ single crystal used in this experiment was the same sample that was used in the D9 and D3 experiments described in § 5.1 and § 5.2.

5.3.4 Data collection.

q scans were performed in the ab plane to grid a box defined by the corners at positions in q of $(-0.7, 0.4, 0)$, $(0.7, 0.4, 0)$, $(0.7, 1.6, 0)$ and $(-0.7, 1.6, 0)$ with a step size of ~ 0.01 in both the a and b directions. A scan was also performed along the c axis from a position of c equal to 0.8 to 2.2.

5.3.5 Results.

In all the q scans performed there was no sign of any scattering in addition to the nuclear Bragg peaks. Therefore, no evidence of long or short range Yb-Yb correlations was found.

5.4 Determination of the concentration of Yb_2O_3 in the polycrystalline sample of $\text{YbNi}_2\text{B}_2^{11}\text{C}$ used in the H.E.T. experiment using the D1B diffractometer at the I.L.L.

5.4.1 Aims of the experiment.

The general principle of the D1B diffractometer is described in § 3.3.3. As outlined in § 6.1.3.2, the polycrystalline $\text{YbNi}_2\text{B}_2^{11}\text{C}$ sample used in the H.E.T. experiment contained a Yb_2O_3 impurity phase. Due to the cubic unit cell, large lattice parameters, and the large number of formula units per unit cell of Yb_2O_3 , the Bragg reflections are relatively few in number, located at low q values, and are weak in comparison with those of the $\text{YbNi}_2\text{B}_2^{11}\text{C}$ phase. This experiment was designed to determine the amount of Yb_2O_3 present, in order to perform a satisfactory background subtraction for the spectra obtained in the H.E.T. experiment. The D1B diffractometer was chosen for this study as it has very good spacial resolution at low q values.

5.4.2 Data collection.

The scattering from the $\text{YbNi}_2\text{B}_2^{11}\text{C}/\text{Yb}_2\text{O}_3$ sample was measured at room temperature using a neutron wavelength of 1.9 Å. The detector covered the angles $-16^\circ < 2\theta < 158^\circ$ with a step size of 0.05° .

5.4.3 Results.

The data collected was processed using the least squares refinement program FULLPROF, available at the I.L.L., dedicated to the analysis of polycrystalline neutron and X-ray data. The $\text{YbNi}_2\text{B}_2^{11}\text{C}$ and Yb_2O_3 compounds were assumed to be the only phases present in the sample. The Yb_2O_3 compound has a cubic structure, space group IA3, with a lattice parameter of 10.42 Å. The results of the refinement are shown in figure 5.24.

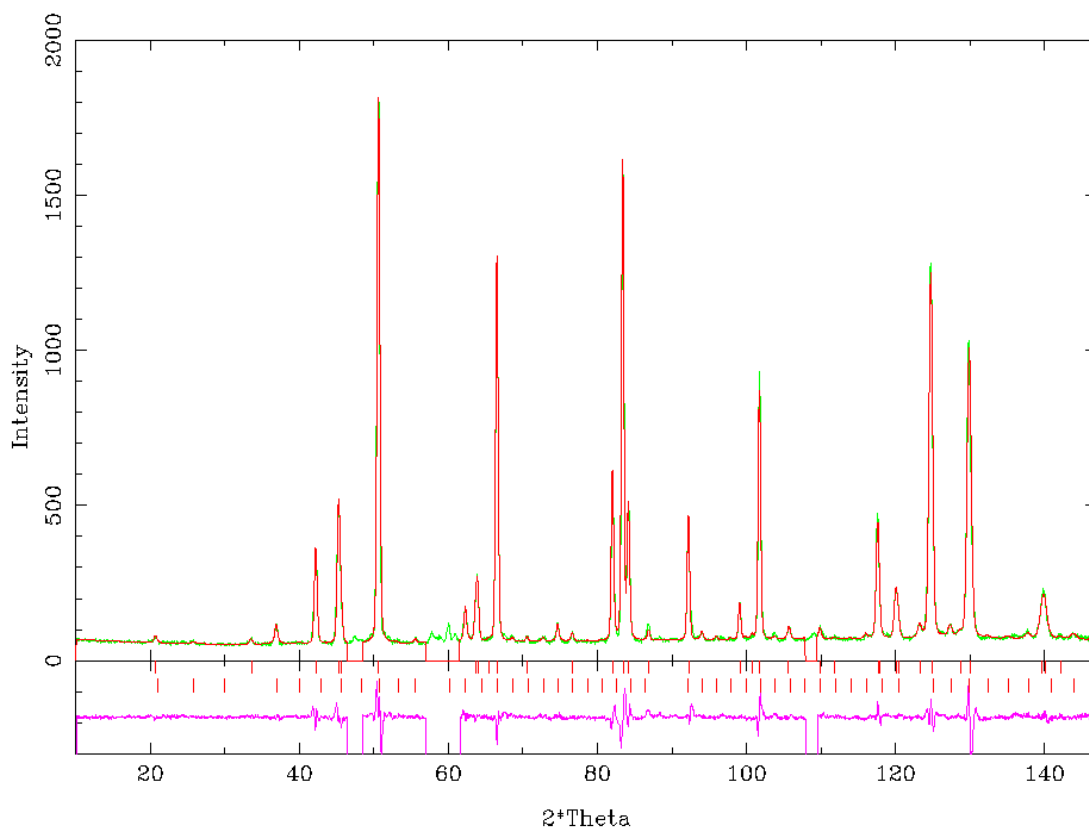


Fig 5.24 : Calculated (red) and observed (green) diffraction spectra for $\text{YbNi}_2\text{B}_2^{11}\text{C}$ and Yb_2O_3 samples. Observed spectrum measured on the D1B diffractometer using a neutron wavelength of 1.9 \AA . Magenta line is the subtraction of the observed spectrum from the calculated spectrum. Vertical red marks show calculated positions of the Bragg peaks for the $\text{YbNi}_2\text{B}_2^{11}\text{C}$ (lower) and Yb_2O_3 (upper) contributing phases.

By comparing the relative intensities of the Bragg reflections, it was determined that the Yb_2O_3 sample constituted $\sim 9\%$ of the total mass of the sample.

Reference.

- [1] B.K. Cho *et al.*, *Phys. Rev. B*, **52**, 3684 (1995).
- [2] G.J. McIntyre, *Neutron and Synchrotron Radiation for Condensed Matter Studies*, Vol. 1, Chap. VII, Springer-Verlag (1994).

- [3] G.L. Squires, *Introduction to the Theory of Thermal Neutron Scattering*, Dover (1996).
- [4] C.G. Darwin, *Phil. Mag.*, **43**, 800 (1922).
- [5] W.H. Zacharisen, *Acta Cryst.*, **23**, 558 (1967).
- [6] P.J. Becker and P. Coppens, *Acta Cryst.*, **A30**, 129 (1974).
- [7] Y. Le Page and E.J. Gabe, *Acta Cryst.*, **A35**, 73 (1979).
- [8] P.J. Brown and J.C. Matthewman, *The Cambridge Crystallography Subroutine Library Users' Manual.*, I.L.L. Publication (1998).
- [9] C. Wilkinson *et al.*, *J. Appl. Cryst.*, **21**, 471 (1988).
- [10] S.K. Sinha *et al.*, *Phys. Rev. B*, **51**, 681 (1995).
- [11] *critical field of Lu*
- [12] W.G. Williams, *Polarized Neutrons*, Oxford University Press, (1988).
- [13] F. Tassets, *Etude par Diffraction de Neutrons Polarises de la Densite d'Aimantation de Compose Intermetallique YCo₅ et des Composes Voisins*, Thesis submitted to the Universite Scientifique et Medicale de Grenoble (1975).
- [14] G.J. McIntyre, (Personal Communication).
- [15] B.E.F. Fender *et al.*, *Proc. R. Soc. Lond.*, **A404**, 127 (1986).
- [16] W. Cochran. *Acta Cryst.*, **1**, 138 (1948).
- [17] A.J. Markvardsen, *Polarised Neutron Studies*, Thesis submitted to the University of Oxford (2000).
- [18] S.F. Gull and J. Skilling, *IEEE Proceedings*, **131** (F), 646 (1984).
- [19] D.S. Sivia, *Data Analysis: A Bayesian Tutorial*, Oxford University Press (1998).
- [20] Theoretical data obtained using GETSFZ. Structure factor generating software available at the I.L.L.
- [21] *The Yellow Book: Guide to Neutron Research Facilities at the I.L.L.*, I.L.L. Publication (1997).
- [22] J.W.Lynn *et al.*, *Phys. Rev. B*, **55**, 6584 (1997).
- [23] R. Sala *et al.*, *Phys. Rev. B*, **56**, 6195 (1995).
- [24] M. Loewenhaupt and K.H. Fischer, *Handbook of Magnetic Materials*, Vol. 7, Elsevier (1993).

CHAPTER 6

INELASTIC NEUTRON SCATTERING EXPERIMENTS

This chapter contains the inelastic scattering experiments conducted on the $\text{YbNi}_2\text{B}_2^{11}\text{C}$ compound. Two experiments, performed using the H.E.T. spectrometer at ISIS and the IN20 spectrometer at the I.L.L., were designed to look for and study the Crystalline Electric Field (C.E.F.) transitions in the compound. Three experiments, performed using the IN5, IN14 and IN6 spectrometers at the I.L.L., were designed to study the low energy transfer scattering. The H.E.T. and IN5 experiments were performed on a polycrystalline sample of $\text{YbNi}_2\text{B}_2^{11}\text{C}$. The IN20, IN14 and IN6 experiments were performed on a single crystal mosaic sample.

6.1 Search for the crystal field transitions in a polycrystalline sample of $\text{YbNi}_2\text{B}_2^{11}\text{C}$ using inelastic neutron scattering and the H.E.T. direct geometry time of flight spectrometer at ISIS.

6.1.1 The High Energy Transfer (H.E.T.) spectrometer.

The general principle of a direct geometry time of flight spectrometer is outlined in § 3.3.4. The neutron beam emerging from the proton target at ISIS is pulsed, and H.E.T. uses a Fermi chopper to monochromate these incident pulses. A Fermi chopper is an aluminium drum with thin sheets of highly absorbing material such as boron, interleaved with neutronically transparent sheets of aluminium. The rotation of the drum is phased to the ISIS pulse, and is only in the transmitting position at the point at which it will transmit neutrons with the desired energy. The slits are curved in opposition to the direction of rotation to optimise transmission.

A large amount of γ -radiation is produced when the proton beam hits the target. The large background that this causes is reduced using a nimonic chopper placed before

the Fermi chopper. This chopper effectively closes the beam tube at the moment the proton beam hits the target.

A neutron monitor is installed after the Fermi chopper and before the sample position to allow the neutron counts measured in the detectors to be normalised to the integrated incident neutron flux.

There are several detector banks on H.E.T: a low angle bank at 4m from the sample position covers the angles 3° to 7° ; another low angle bank at 2.5m covers the angles 9° to 29° ; a 4m high angle bank covers the angles 110° to 125° , and the angles 130° to 140° are covered by a detector bank at 2.5m (see fig. 6.4) [1].

6.1.2 Aims of the experiment.

The spin-orbit $4f$ electronic ground state of the Yb $+3$ ion in $\text{YbNi}_2\text{B}_2^{11}\text{C}$ has $L = 3$, $S = 1/2$ and $J = 7/2$, and is eight fold degenerate (see § 2.1.1.2). The tetragonal symmetry of the rare earth site would imply that this ground state is split into four doublets $\Gamma_6 \text{CP1}$, $\Gamma_7 \text{CP2}$, $\Gamma_6 \text{CP3}$ and $\Gamma_7 \text{CP4}$ by the crystal field interaction (see § 2.1.2.1). Calculations based on the crystal field transitions that have been observed in the $\text{ErNi}_2\text{B}_2^{11}\text{C}$, $\text{HoNi}_2\text{B}_2^{11}\text{C}$ and $\text{TmNi}_2\text{B}_2^{11}\text{C}$ compounds indicate that the positions in energy of the excited doublets are as shown below [2].

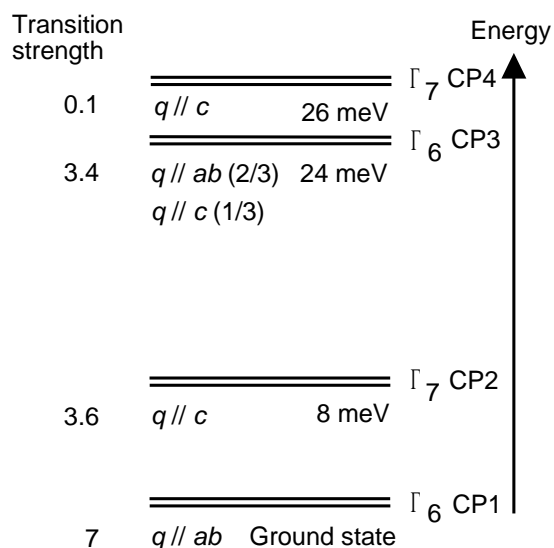


Fig 6.1 : Energy level diagram of the C.E.F. splitting of the $4f$ $J = 7/2$ spin-orbit ground state of the Yb^{+3} ion in $YbNi_2B_2^{11}C$. Transition strengths and selection rules are shown; q is the scattering vector and a, b and c are the crystallographic axes.

The aim of this experiment was to search for the C.E.F. transitions in a polycrystalline sample of $YbNi_2B_2^{11}C$ and compare them to the scheme presented above. In other heavy fermion and valence fluctuation compounds, there is significant movement and broadening of C.E.F. levels due to the hybridisation of the rare earth $4f$ and conduction electrons and the introduction of the associated relaxation pathways (see § 2.2.5). A non-magnetic $Y_{0.5}Lu_{0.5}Ni_2B_2^{11}C$ background sample was also measured to provide a method of subtraction of the nuclear scattering contribution to the measured $YbNi_2B_2^{11}C$ spectra. The 0.5/ 0.5 mixture of yttrium and lutetium was chosen so that the compound had the same total linear attenuation coefficient as the $YbNi_2B_2^{11}C$ compound.

6.1.3 Sample preparation.

The B^{11} isotope was used in the preparation of the following compounds as it has a considerably lower neutron absorption cross section as compared with naturally occurring boron (containing 20% by mass of B^{10}). The samples were prepared at the University of Warwick, U.K.

6.1.3.1 Polycrystalline $\text{Y}_{0.5}\text{Lu}_{0.5}\text{Ni}_2\text{B}_2^{11}\text{C}$.

This sample was produced using an argon arc furnace. An arc furnace is a copper chamber with a removable base or hearth into which the unreacted elements are placed. The chamber can be evacuated of air and filled with Argon. Two movable cathode electrodes with sharply pointed tungsten tips pass through the top of the chamber. The hearth acts as the anode. The electrodes are connected to a high current, low voltage power supply. If the two electrodes are brought into contact an arc is struck between them that may then be used to melt the elements together to form a compound.

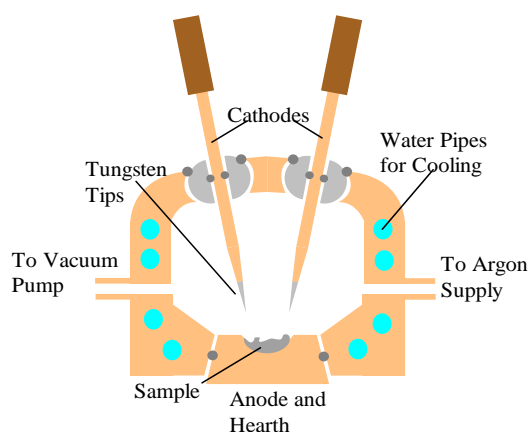


Fig 6.2 : A cross section through an argon arc furnace.

A nickel ball was first arc melted with the powdered boron. Then the carbon in powdered form and the yttrium and lutetium in ingot form were added. The elements were added one at a time and the compound weighed at each stage in order to make sure that there were no losses. After all the elements had been added, the resulting ingot was turned over and remelted. This was done several times in order to ensure that the elements were completely reacted. The final sample mass was 12.0g.

6.1.3.2 Polycrystalline $\text{YbNi}_2\text{B}_2^{11}\text{C}$.

Ytterbium has a high vapour pressure and $\text{YbNi}_2\text{B}_2^{11}\text{C}$ cannot be produced by the argon arc furnace method alone as the ytterbium would vaporise as soon as the arc struck the unreacted elements.

A nickel ball and powdered boron were first arc melted together in the standard way and then ground to a very fine powder. This powder was then mixed thoroughly with appropriate amounts of powdered ytterbium and carbon. The resulting mixture was pressed into pellets. These pellets were placed in molybdenum crucibles. The crucibles were welded shut under argon in an arc furnace. The crucibles were in turn sealed under vacuum in quartz tubes and slowly heated in a box furnace over a period of six days up to a temperature of 1200 °C. The temperature was then reduced to 1050 °C and kept there for a further four days to anneal the sample. The sample was then furnace cooled. The final sample mass was 13.25g.

An X-ray diffraction experiment was performed on the resulting compound which showed the presence of an Yb_2O_3 impurity phase. Due to the cubic unit cell, large lattice parameters, and large number of formula units per unit cell, only a few small impurity peaks, located at low q values, were visible in the X-ray spectra. It was therefore difficult to estimate the amount of impurity present. In order to achieve a better estimate, a neutron diffraction experiment was performed on D1B at the I.L.L. (see § 5.4). This experiment indicated that the $\text{YbNi}_2\text{B}_2^{11}\text{C}$ sample contained ~9 % by mass of Yb_2O_3 .

6.1.3.3 Polycrystalline Yb_2O_3 and Y_2O_3 .

A 14 g sample of Yb_2O_3 was obtained from Alpha Chemicals (99.9% pure). A 14.2 g sample of Y_2O_3 was obtained from Aldrich Chemicals (99.99% pure). The Y_2O_3 sample was used to subtract the lattice contribution to the measured Yb_2O_3 spectra. The vanadium sample used was a standard test sample available at ISIS.

6.1.4 Data collection.

The following spectra were taken:

Compound	Temp	Time	E_i (meV)	Energy range (ΔE , meV)	
	(K)			(μ Ahr)	Start
YbNi ₂ B ₂ ¹¹ C	5	1875.2	250	-150	200
		773.1	75	-40	70
		1295.5	35	-15	30
Y _{0.5} Lu _{0.5} Ni ₂ B ₂ ¹¹ C	2.7	986.7	250	-150	200
		500	75	-40	70
		487.1	35	-15	30
Yb ₂ O ₃	20	1500	250	-150	200
		1598.3	75	-40	70
Y ₂ O ₃	20	282.1	250	-150	200
		300.3	75	-40	70
Vanadium	300	40.3	250	-150	200
		40.4	75	-40	70
		40.1	35	-15	30

Fig 6.3 : The spectra measured on H.E.T.

Measurements of vanadium with a polychromatic beam are made regularly on H.E.T. These measurements are used to correct for detector efficiency fluctuations over long periods of time. They enable monochromatic vanadium scans to be used in the normalisation of sample data that were measured a significant time before the sample data were taken [1].

6.1.5 Analysis of the data.

6.1.5.1 Initial data processing.

The initial processing of the raw data was performed using the HOMER computer program available at ISIS [1]:

The number of neutrons scattered into an individual detector for a given time channel I_{sam} is divided by the integrated incident neutron flux F_{sam} using information from the monitor placed in between the Fermi chopper and the sample position. The number of neutrons scattered into the same detector and time channel from the vanadium sample I_{van} is also divided by the integrated incident flux for that measurement F_{van} . For the vanadium sample, if this process is repeated for all of the time channels of the detector, the integral across those representing the elastic peak E_{van} can be taken. For the sample, the value of $I_{\text{sam}} / (F_{\text{sam}} E_{\text{van}})$ gives the intensity normalised to incident flux and vanadium scattering. The polychromatic vanadium runs are used to correct this result for variations in detector efficiency. This value is corrected for the different absorptions of the sample and the vanadium by multiplying by $(T_{\text{van}} / T_{\text{sam}})$. The result is multiplied by $N_{\text{van}} \sigma_{\text{van}} / 4\pi$ (where N_{van} is the number of vanadium atoms in the sample) as this is the total incoherent scattering cross-section of the vanadium sample per unit solid angle. Finally, this is divided by the number of formula units in the sample N_{sam} . If the data is rebinned in terms of energy transfer instead of time of flight, the output is in the units ‘ $\text{mb sr}^{-1} \text{meV}^{-1} [\text{formula unit}]^{-1}$ ’. A masking file gives the detectors to be discarded because they are abnormally noisy, contain spurious Bragg scattering, or have an efficiency that has varied significantly between polychromatic vanadium measurements. The data from each detector are grouped according to the angle of the detector. The angles defining these groups are given in a mapping file. In this experiment the detector groupings were as follows:

Detector group	Average angle (°)	Detector bank
W1	4.9	4 m low angle
W2	4.9	4 m low angle
W3	11.5	2.5 m low angle
W4	16.5	2.5 m low angle
W5	21.5	2.5 m low angle
W6	26.5	2.5 m low angle
W7	114.9	4 m high angle
W8	133.4	2.5 m high angle

Fig 6.4 : H.E.T. detector groupings [1].

The above process is summarised in the following equation:

$$\frac{d^2 \sigma}{d\Omega dE [\text{form}]} = I_{\text{sam}} \times \frac{1}{F_{\text{sam}} E_{\text{van}}} \frac{T_{\text{van}}}{T_{\text{sam}}} \frac{N_{\text{van}} \sigma_{\text{van}}}{4\pi} \frac{1}{N_{\text{sam}}} \quad \text{Eq 6.1}$$

6.1.5.2 Non magnetic and Yb₂O₃ background subtraction.

The cross-section for the magnetic scattering of neutrons is a function of the square of the magnetic form factor. Magnetic form factors decrease rapidly with increasing q (the form factor for ytterbium decreases to a quarter of its zero- q value by $q \sim 7 \text{ \AA}^{-1}$). In contrast, the nuclear cross-section is proportional to q^2 . These different q dependencies provide a method for subtracting the phonon contribution from the spectra taken for the YbNi₂B₂¹¹C and Yb₂O₃ compounds:

The Y_{0.5}Lu_{0.5}Ni₂B₂¹¹C and Y₂O₃ samples have no magnetic scattering. The intensity of the nuclear scattering collected from the low and high angle detector banks will be different. The factors $\{x\}$ that are needed to scale the high angle Y_{0.5}Lu_{0.5}Ni₂B₂¹¹C and Y₂O₃ data to match their respective low angle data can be calculated. The high angle data for the YbNi₂B₂¹¹C and Yb₂O₃ compounds will contain almost no magnetic contribution. Therefore, these data, when multiplied by the corresponding value of x , give an estimate of the phonon contributions to the low angle YbNi₂B₂¹¹C and Yb₂O₃ data. This method is preferable to simply assuming that the Y_{0.5}Lu_{0.5}Ni₂B₂¹¹C and Y₂O₃ data represent the lattice contributions to the YbNi₂B₂¹¹C and Yb₂O₃ scattering as the two non-magnetic compounds will have slightly different phonon spectrums to the Yb compounds.

The high and low angle detector groups were chosen as follows for the different E_i spectra:

E_i (meV)	Low angle detector group	High angle detector group
250	W1 and W2	W7
75	W3 and W4	W8
35	W1 and W2	W7

Fig 6.5 : Detector groups chosen for the background subtraction procedure for different values of E_i .

After this procedure had been used to subtract the nuclear scattering from the $\text{YbNi}_2\text{B}_2^{11}\text{C}$ and Yb_2O_3 data, a proportion of the Yb_2O_3 data was subtracted from the $\text{YbNi}_2\text{B}_2^{11}\text{C}$ data consistent with a 9 % by mass impurity.

The three resulting $\text{YbNi}_2\text{B}_2^{11}\text{C}$ spectra were corrected for the energy dependent absorption of the neutrons by the sample. Finally, the spectra were divided by the square of the magnetic form factor $f^2(q)$ to correct for variations in the strength of the magnetic scattering with q .

The results of all the inelastic experiments performed in this thesis are described together in § 6.6.

6.2 Search for the crystal field transitions in a single crystal mosaic sample of $\text{YbNi}_2\text{B}_2^{11}\text{C}$ using inelastic neutron scattering and the IN20 triple axis spectrometer at the I.L.L.

6.2.1 The IN20 spectrometer.

The general principle of a triple axis spectrometer is outlined in § 3.3.5. IN20 operates with thermal neutrons, $2.66 \text{ \AA}^{-1} < k_i < 4.1 \text{ \AA}^{-1}$. In this experiment, a variable curvature pyrolytic-graphite (P.G.) monochromator [(002), d -spacing 3.355 \AA] and a horizontally focusing variable curvature P.G. analyser were used. A $60'$ collimator was placed just after the monochromator and a convergent collimator was placed before the entrance to the analyser. Two diaphragms were placed before and after the sample position to reduce the beam size to approximately that of the sample. A P.G.

filter was placed just before the convergent collimator to remove the $\lambda/2$ contamination of the beam. There are two monitors on IN20: monitor 1 is located before the sample position and is used to normalise the detector counts to the integrated incident flux; monitor 2 is inside the analyser and is used to detect increases in scattering that may be due to spurious Bragg scattering entering the analyser from the sample or cryostat [3].

6.2.2 Aims of the experiment.

The $\text{YbNi}_2\text{B}_2^{11}\text{C}$ data from the H.E.T. experiment showed three broad peaks centered at energies of 3 meV, 17 meV and 43 meV (see fig. 6.12). As mentioned in § 6.1.3.2, the polycrystalline sample used in the H.E.T. experiment contained a 9% by mass Yb_2O_3 impurity. This experiment was designed to re-examine the energy range covered by the H.E.T. experiment using a pure single crystal $\text{YbNi}_2\text{B}_2^{11}\text{C}$ sample. As a single crystal sample was used, the q dependence of the excitations could be studied, enabling comparisons to be made with the calculated selection rules of the crystal field transitions of the ytterbium ion shown in fig. 6.1. A non-magnetic $\text{LuNi}_2\text{B}_2^{11}\text{C}$ sample was used to give an estimate of the phonon contribution to the scattering measured from the $\text{YbNi}_2\text{B}_2^{11}\text{C}$ sample.

6.2.3 Sample preparation.

The $\text{YbNi}_2\text{B}_2^{11}\text{C}$ and $\text{LuNi}_2\text{B}_2^{11}\text{C}$ single crystals used in this experiment were prepared at the Ames laboratory using the Ni_2B^{11} flux growth technique [4]. In order to achieve a reasonable sample mass, mosaic samples were constructed by mutually aligning many crystals on a flat aluminium plate. The $\text{YbNi}_2\text{B}_2^{11}\text{C}$ sample consisted of forty single crystals with a total mass of 0.945g with a composite mosaic spread of $\sim 8^\circ$. The $\text{LuNi}_2\text{B}_2^{11}\text{C}$ sample consisted of six single crystals with a total mass of 0.486g with a composite mosaic spread of $\sim 7^\circ$.

6.2.4 Data collection.

IN20 was used in ‘constant- k_f ’ mode throughout this experiment. The following ω – scans were performed for the $\text{YbNi}_2\text{B}_2^{11}\text{C}$ and $\text{LuNi}_2\text{B}_2^{11}\text{C}$ samples:

k_f (\AA^{-1})	q position			q mag (\AA^{-1})	Temp (K)	energy (meV)	
	h	k	l			start	end
2.662	1.15	0	0.6	2.10	1.5	-5	30
2.662	1.2	0	0	2.15	1.5	-5	30
2.662	0	0	3.56	2.13	1.5	-5	30
4.1	1.9	0	0	3.41	5	-10	75
4.1	0.4	0	5.7	3.48	5	-8	75

Fig 6.6 : The spectra measured on IN20.

The results of all the inelastic experiments performed in this thesis are described together in § 6.6.

6.3 Low energy magnetic excitations in a single crystal mosaic sample of $\text{YbNi}_2\text{B}_2^{11}\text{C}$ using inelastic neutron scattering and the IN14 triple axis spectrometer at the I.L.L.

6.3.1 The IN14 spectrometer.

The general principle of a triple axis spectrometer is outlined in § 3.3.5. IN14 operates with thermal neutrons, $2 \text{\AA} < \lambda < 6 \text{\AA}$, and is capable of achieving energy resolutions of 1 meV to 0.02 meV. In this experiment, a variable vertically curved pyrolytic-graphite (P.G.) monochromator [(002), d -spacing 3.355 \AA] and a horizontally focusing variable curvature P.G. analyser were used. No collimation was used before or after the sample position. Two diaphragms were placed between the monochromator and the sample, and one diaphragm was placed between the sample and the analyser. The opening of all the diaphragms was adjusted so that they were just larger than the size of the sample. A beryllium filter was placed in between the last diaphragm and the

analyser to remove $\lambda / 2$ contamination of the beam. There are two monitors on IN14: monitor 1 is located before the sample position and is used to normalise the detector counts to the integrated incident flux; monitor 2 is inside the analyser and is used to detect increases in scattering that may be due to spurious Bragg scattering entering the analyser from the sample or cryostat. The base of the cryostat (level with the sample) was placed at the centre of a large evacuated cylinder. This reduced air scattering of the incident beam. This ‘vacuum box’ was needed so that positions in reciprocal space with low energy and q could be reached without the analyser receiving stray neutrons from the incident beam [3].

6.3.2 Aims of the experiment.

A study of the low energy magnetic excitations in a polycrystalline sample of $\text{YbNi}_2\text{B}_2^{11}\text{C}$ has been made by C. Sierks *et al* using the IN5 spectrometer [5]. They modelled their low temperature data ($T = 1.5$ K) data with two inelastic components. The first of these was a narrow Lorentzian, centred at ~ 0.34 meV, with a HWHM of ~ 0.33 meV. The energy scale of this peak corresponds well with a Kondo temperature of ~ 10 K that has been obtained from specific heat measurements [6]. The second component, centred at ~ 3.5 meV, had a much broader width, which they attributed to a transition to the first excited C.E.F. level.

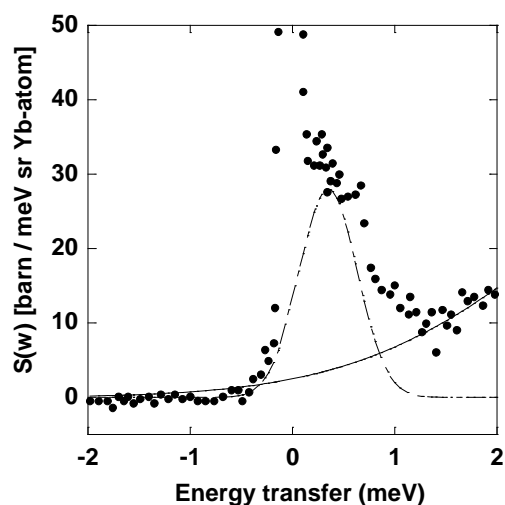


Fig 6.7 : Low energy transfer neutron spectrum of $\text{YbNi}_2\text{B}_2^{11}\text{C}$ at $T = 1.5$ K with incident energy of 3.15 meV. Measured on IN5 with a polycrystalline sample [5].

The aim of this experiment was to study the $\text{YbNi}_2\text{B}_2^{11}\text{C}$ compound over the same energy range and at the same temperature as C. Sierks *et al.* but using a single crystal sample. As a single crystal sample was used, the q dependence of the low energy scattering could be studied. This would provide more information as to the origin of the observed features. As with the IN20 experiment, a non-magnetic $\text{LuNi}_2\text{B}_2^{11}\text{C}$ sample was used to give a estimate of the phonon contribution to the scattering measured from the $\text{YbNi}_2\text{B}_2^{11}\text{C}$ sample.

6.3.3 Sample preparation.

The $\text{YbNi}_2\text{B}_2^{11}\text{C}$ and $\text{LuNi}_2\text{B}_2^{11}\text{C}$ single crystals used in this experiment were the same ones that were used in the IN20 experiment (see § 6.2.3).

6.3.4 Data collection.

The spectrometer was used in ‘constant- k_f ’ mode throughout this experiment. The following ω -scans and q -scans were performed at a temperature of 1.5 K for the $\text{YbNi}_2\text{B}_2^{11}\text{C}$ and $\text{LuNi}_2\text{B}_2^{11}\text{C}$ samples:

k_f (\AA^{-1})	q position			q magnitude (\AA^{-1})	energy range (meV)	
	h	k	l		start	end
1.5	0.55	0	0	0.99	-1.5	5.9
1.5	1.25	0	0	2.24	-1.1	5.9
1.5	0.4	0.4	0	1.02	-1.5	4.9
1.5	0	0	3.7	2.21	-1.4	5.9

k_f (\AA^{-1})	Energy (meV)	q start position			q end position		
		h	k	l	h	k	l
1.4	0.5	0.05	0	0	1.05	0	0
1.5	0.6	0.05	0.05	0	1.05	1.05	0

Fig 6.8 : The spectra measured on IN14.

The results of all the inelastic experiments performed in this thesis are described together in § 6.6.

6.4 Low energy magnetic excitations in a polycrystalline sample of $\text{YbNi}_2\text{B}_2^{11}\text{C}$ using inelastic neutron scattering and the IN5 direct geometry time of flight spectrometer at the I.L.L.

6.4.1 The IN5 spectrometer.

The general principle of a direct geometry time of flight spectrometer is outlined in § 3.3.4. The neutron beam emerging from the reactor at the I.L.L. is continuous and polychromatic. IN5 uses four disc choppers to pulse and monochromate the incident beam. A disc chopper is a rotating disc with an opening that allows neutrons to pass only when the disc is in a certain portion of its rotation cycle. The first chopper, situated furthest from the sample position, produces a pulse of polychromatic neutrons. The fourth chopper is synchronised to the first so that only neutrons with the desired wavelength pass through to the sample position. The second chopper is close to the midpoint between the first chopper and the fourth chopper. It eliminates the unwanted harmonics of the selected neutron wavelength. The third chopper can be rotated more slowly than the others to blank out some of the pulses generated by the first chopper. This facility is needed when fast neutrons from one pulse catch up slow moving neutrons from a previous pulse in their passage to the detector banks. This ‘frame overlap’ makes the time of flight measurement impossible and must be removed. IN5 has extremely good energy resolution which makes it ideal for studying very low energy excitations such as the quasielastic scattering of heavy fermion compounds [3].

6.4.2 Aims of the experiment.

This experiment was designed to study the low energy magnetic excitations in a polycrystalline sample of $\text{YbNi}_2\text{B}_2^{11}\text{C}$. The aim was to look for the excitations responsible for the heavy fermion behaviour exhibited by this compound. As mentioned in the description of the IN14 experiment, a study of the low energy

magnetic excitations in $\text{YbNi}_2\text{B}_2^{11}\text{C}$ has been made by C. Sierks *et al.* using IN5 (see § 6.3.2). When a proposal for this IN5 experiment was submitted, this data had not been published.

6.4.3 Sample preparation.

The $\text{YbNi}_2\text{B}_2^{11}\text{C}$ and $\text{Y}_{0.5}\text{Lu}_{0.5}\text{Ni}_2\text{B}_2^{11}\text{C}$ polycrystalline samples used in this experiment were the same ones that were used in the H.E.T. experiment described in § 6.1.3. A 10 g sample of Yb_2O_3 was obtained from Fluka Chemicals (99.9% pure). The vanadium sample used was a standard test sample available at the I.L.L.

6.4.4 Data collection.

The following spectra were taken using an incident wavelength of 5 \AA . The energy range covered was -30 meV to 2.5 meV.

Compound	Temp (K)	Time (s)
$\text{YbNi}_2\text{B}_2^{11}\text{C}$	1.5	42681
$\text{Y}_{0.5}\text{Lu}_{0.5}\text{Ni}_2\text{B}_2^{11}\text{C}$	1.5	43200
Yb_2O_3	1.5	41896
Empty can	1.5	21600
	100-250	30111
Vanadium	100-250	5807

Fig 6.9 : The spectra measured on IN5.

6.4.5 Analysis of the data.

The preliminary analysis of the data was performed using the LAMP (Large Array Manipulation Program) software available at the I.L.L. [7]. The procedure used to normalise the data to units of ‘ $\text{mb sr}^{-1} \text{ meV}^{-1} [\text{formula unit}]^{-1}$ ’ was similar to that performed by the HOMER software used to process the H.E.T. data (see § 6.1.5.1). The IN5 data shown in § 6.6 was produced by summing the energy scans measured by all the detectors at all positions in q .

The results of all the inelastic experiments performed in this thesis are described together in § 6.6.

6.5 Low energy magnetic excitations in a single crystal mosaic sample of $\text{YbNi}_2\text{B}_2^{11}\text{C}$ using inelastic neutron scattering and the IN6 direct geometry time of flight spectrometer at the I.L.L.

6.5.1 The IN6 spectrometer.

The general principle of a direct geometry time of flight spectrometer is outlined in § 3.3.4. The neutron beam emerging from the reactor at the I.L.L. is continuous and polychromatic. IN6 uses three composite pyrolytic graphite monochromator crystals to select the desired incident neutron wavelength and two choppers to pulse the beam. The monochromators can deliver four wavelengths: 4.1 Å, 4.6 Å, 5.1 Å and 5.9 Å. A Fermi chopper with a short slot length, to achieve good transmission, is situated 38 cm from the sample positions (see § 6.11). At Fermi chopper rotation velocities greater than 7500 rpm, a suppresser chopper is placed before the Fermi chopper to eliminate frame overlap. The higher order reflections from the graphite monochromators are removed by a beryllium-filter situated between the monochromators and the chopper assembly [3].

6.5.2 Aims of the experiment.

As mentioned in § 6.6, the quality of the IN5 data was spoiled by the presence of the Yb_2O_3 impurity in the $\text{YbNi}_2\text{B}_2^{11}\text{C}$ sample. This experiment was designed to study the low energy transfer magnetic scattering over a similar energy range to the IN5 experiment but with a pure single crystal sample. The experiment was conducted during a short period of test time on IN6. There was insufficient time to set up the instrument in the desired configuration. As a result, the energy loss data contained a region of large spurious scattering originating from the cryostat, in the energy transfer region of interest. However, the energy gain scattering was not effected.

6.5.3 Sample preparation.

The $\text{YbNi}_2\text{B}_2^{11}\text{C}$ single crystals used in this experiment were the same ones that were used in the IN20 experiment described in § 6.2.3. The vanadium sample used was a standard test sample available at the I.L.L.

6.5.4 Data collection.

The following spectra were taken using an incident wavelength of 4.1 Å. The energy range covered was -50 meV to 3.5 meV.

Compound	Temp (K)	Time (s)
$\text{YbNi}_2\text{B}_2^{11}\text{C}$	1.8	7200
	10	7200
Empty can	10	4620
	100	5979
Vanadium	100	6000

Fig 6.10 : The spectra measured on IN6.

6.5.5 Analysis of the data.

As for the IN5 experiment (see § 6.4.5).

The results of all the inelastic experiments performed in this thesis are described together in the following section

6.6 Results.

The scattering observed in all the inelastic experiments performed on $\text{YbNi}_2\text{B}_2^{11}\text{C}$ in this thesis is broad in energy or relatively weak in relation to the background scattering. These factors have made the identification of real features in the data difficult. The most reliable method of identifying the magnetic scattering of interest has been to compare measurements produced using different neutron spectrometers

and samples of $\text{YbNi}_2\text{B}_2^{11}\text{C}$. For this reason, the results from all the experiments are presented together in this section.

A description of the H.E.T. spectrometer and a list of the scans performed is given in § 6.1. This section also gives a detailed account of the preliminary data analysis.

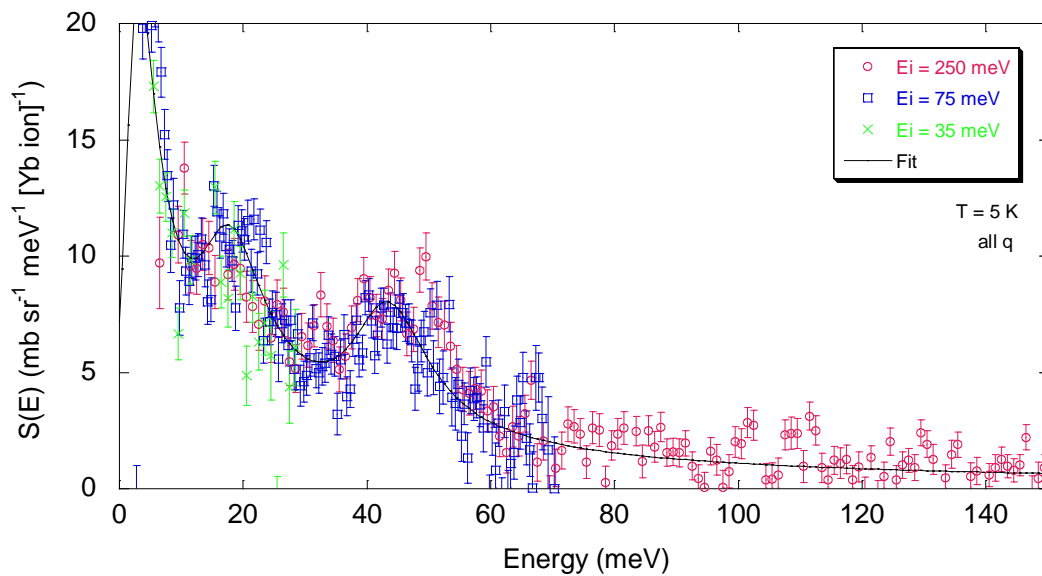


Fig 6.11 : The magnetic scattering from a polycrystalline sample of $\text{YbNi}_2\text{B}_2^{11}\text{C}$ at a temperature of 5 K obtained using the H.E.T. spectrometer. Data obtained using incident neutron energies of 35 meV, 75 meV and 250 meV are shown.

The above figure shows the fully processed H.E.T. data obtained with all the incident neutron energies overlaid. The features in this data are broad in energy and extend beyond 150 meV.

Each sample transition in the above data can be represented by two broadened Lorentzians [A (neutron energy loss scattering) and D (neutron energy gain scattering) in equation 6.2]. The fractional coefficient of the term in square brackets in equation 6.2 and the terms labelled by B , F , C and G ensure that the principle of detail balance is satisfied and that the spectral intensity for each peak remains constant as the temperature is changed.

$$S(E) = \sum_i \chi_i \frac{E}{1 - \exp\left(-\frac{E}{k_B T}\right)} [ABC + DFG], \quad \text{Eq 6.2}$$

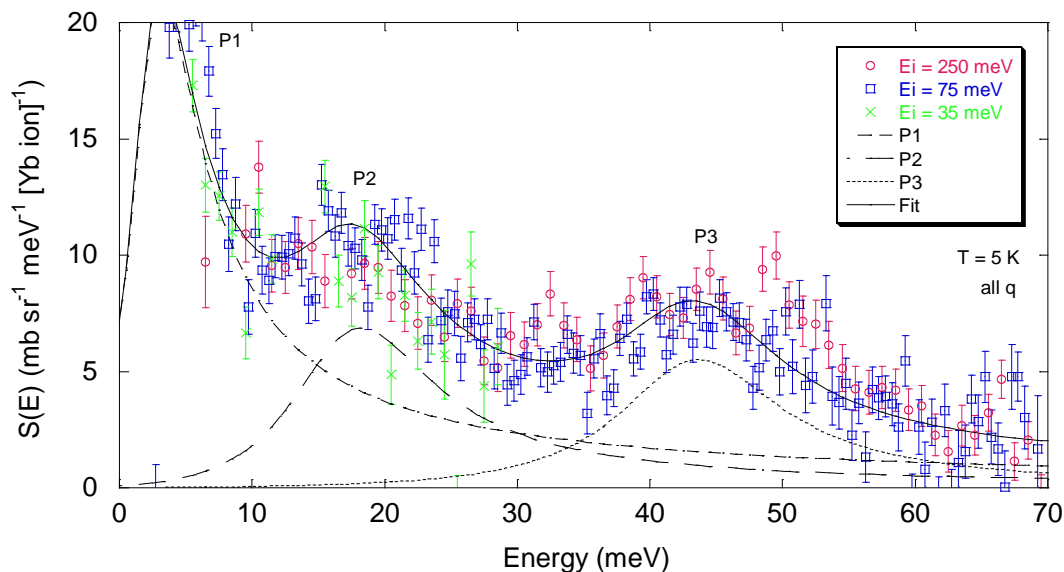
where

$$D = \frac{\Gamma_i/\pi}{(E \mp E_i)^2 + \Gamma_i^2}, \quad F = \frac{1 - \exp\left(\frac{\mp E_i}{k_B T}\right)}{\pm E_i},$$

$$C = \frac{1}{1 + \exp\left(-\frac{E_i}{k_B T}\right)} \quad \text{and} \quad G = \frac{\exp\left(-\frac{E_i}{k_B T}\right)}{1 + \exp\left(-\frac{E_i}{k_B T}\right)}.$$

In the above equations E is the neutron energy transfer and χ_i , E_i and Γ_i are the amplitude, centre and half width half maximum of the i^{th} peak.

Three inelastic peaks P1, P2 and P3 were identified in the neutron energy loss scattering shown in figure 6.11 (see fig. 6.12). The P1 peak was also treated as a quasielastic peak (centred on 0 meV). However, this provided a less good fit to the low energy scattering (i.e. P1 and P2) of the data. The data presented in figure 6.12 can be compared with the theoretically calculated C.E.F. transitions shown in figure 6.1. A preliminary comparison would suggest that P2 and P3 can be identified with the CP2 and CP3 transitions. It would seem unlikely that P3 would correspond to the CP4 transition as there is such a large mismatch in the transition strengths. If this assignment is made then P1 must correspond to the ground state (CP1) of the theoretically calculated C.E.F. scheme. The theoretical model gives the transition intensities for CP1, CP2 and CP3 as 497, 260 and 228 mb sr⁻¹ [Yb ion]⁻¹ respectively [2]. Making the identification as above, the relative intensities of P1, P2 and P3 are broadly consistent with this model although they are all less by a factor of ~0.7 than predicted. The most striking difference between the H.E.T. data and the theoretical model is that the positions of P1, P2 and P3 are roughly a factor of two greater than the predicted values.



Peak	Centre E_i (meV)	Width HWHM Γ_i (meV)	Intensity χ_i (meV ⁻¹)
P1	3	3	43
P2	17	6.5	8
P3	43	7.5	3

Fig 6.12 : Magnetic scattering, below 70 meV, from a polycrystalline sample of $\text{YbNi}_2\text{B}_2^{11}\text{C}$ at a temperature of 5 K obtained using the H.E.T. spectrometer. Data obtained using incident neutron energies of 35 meV, 75 meV and 250 meV are shown. The broken lines represent the three component peaks P1, P2 and P3 that make up the overall lineshape.

The IN20 experiment was designed to confirm the general features of the magnetic scattering seen in the H.E.T. experiment and also to gain information concerning the q dependence of the peaks. A description of the IN20 spectrometer and a list of the scans performed are given in § 6.2. Figures 6.13 and 6.14 show energy scans taken at a temperature of 5 K using a final neutron wavevector of 4.1 \AA^{-1} , at q positions of (1.9,0,0) and (0.4,0,5.7) respectively. A position in q of (0.4,0,5.7) was chosen, instead of a position with no ab plane component, as positions with a similar magnitude in q lying exactly on the c axis were found to have spurious contamination.

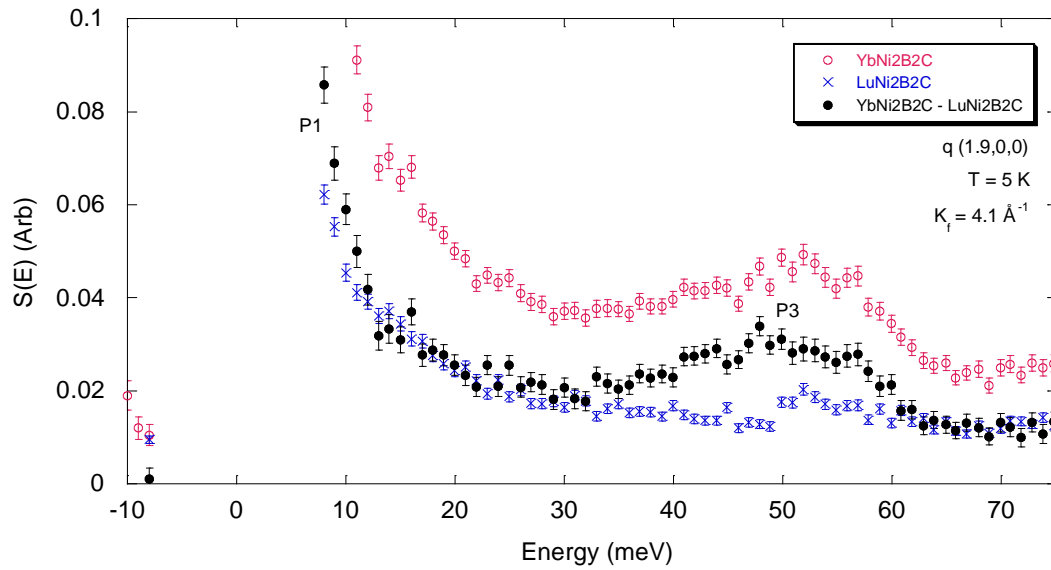


Fig 6.13 : Energy scans from single crystal mosaic samples of $\text{YbNi}_2\text{B}_2^{11}\text{C}$ and $\text{LuNi}_2\text{B}_2^{11}\text{C}$ at a q position of (1.9,0,0) and at a temperature of 5 K obtained using the IN20 spectrometer. The data was taken with a final neutron wavevector of 4.1 \AA^{-1} .

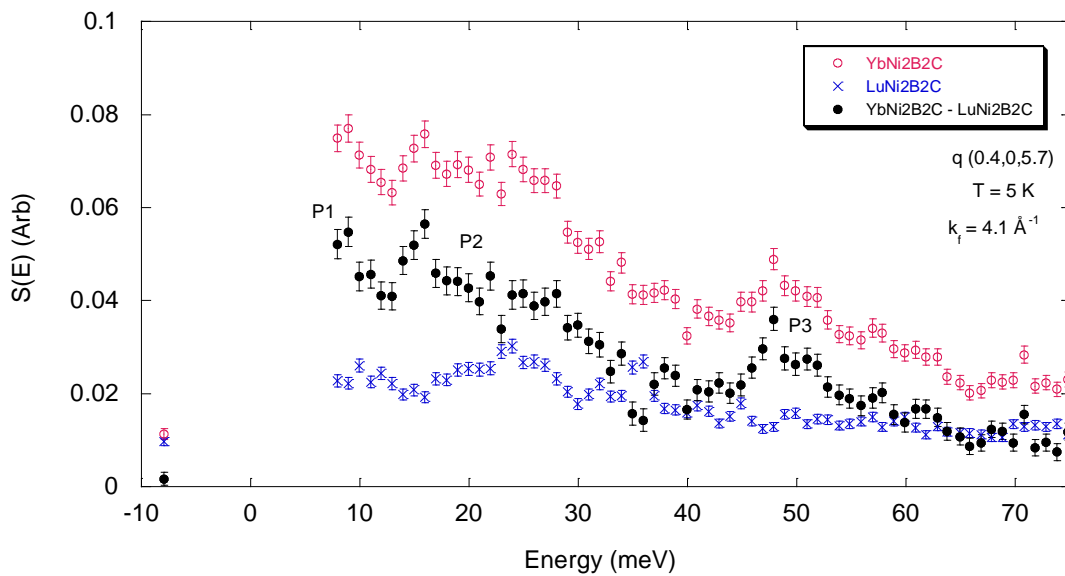


Fig 6.14 : Energy scans from single crystal mosaic samples of $\text{YbNi}_2\text{B}_2^{11}\text{C}$ and $\text{LuNi}_2\text{B}_2^{11}\text{C}$ at a q position of (0.4,0,5.7) and at a temperature of 5 K obtained using the IN20 spectrometer. The data was taken with a final neutron wavevector of 4.1 \AA^{-1} .

According to the calculated selection rules, the CP2 transition is seen when q is parallel to the c axis. Two thirds of the CP3 transitions is seen when q is in the ab scattering plane and the remaining third when q is parallel to the c axis. Transitions within the ground state doublet are visible when q is in the ab scattering plane.

It is clear from figures 6.13 and 6.14 that the scattering at the two q positions is very different. Perhaps the most easily identifiable feature in figure 6.13 is the broad peak centred at ~ 48 meV. This feature is also visible in figure 6.14, although it is less intense. This corresponds to the P3 peak seen in the H.E.T. data. The q dependence of this peak corresponds well with the selection rules for the CP3 transition.

The other feature present in figure 6.13 is the larger intensity scattering that starts from a maximum near the elastic line and falls off sharply with increasing energy transfer. It is also present, to a much lesser extent, in the (0.4,0,5.7) data. This scattering may be identified with the P1 peak seen in the H.E.T. data. The q dependence of this feature agrees well with that predicted by the selection rules for the CP1 transition.

In addition to the two features already mentioned in figure 6.14, there is broad scattering between energies of 15 meV and 25 meV, which is not present in figure 6.13. This scattering corresponds to the P2 peak seen in the H.E.T. data. Again, its q dependence agrees with the theoretical prediction that it should only be seen with q parallel to c .

Figure 6.15 shows the sum of two thirds the (1.9,0,0) scan and one third the (0.4,0,5.7) scan superimposed on the H.E.T. data and scaled to the correct intensity.

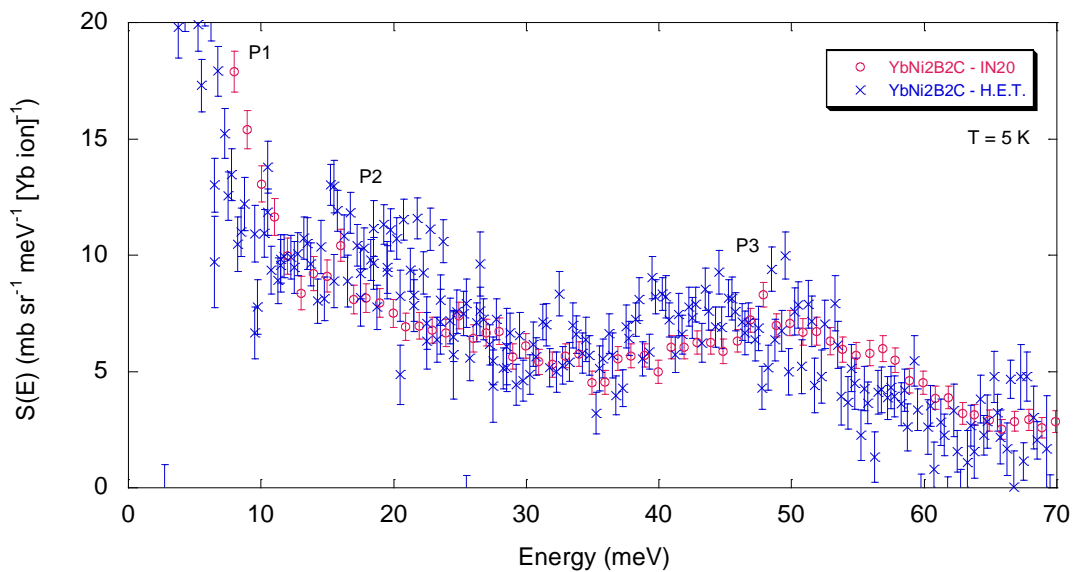
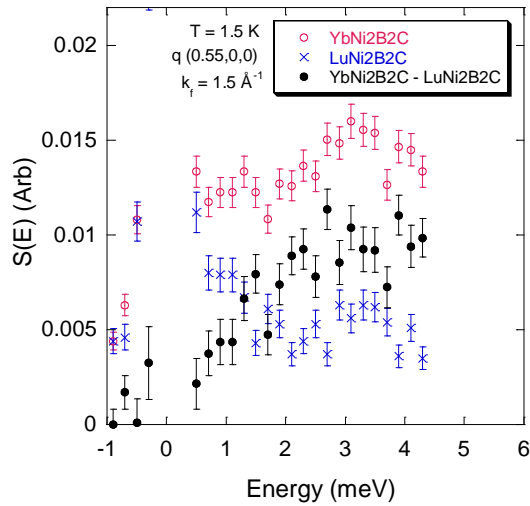
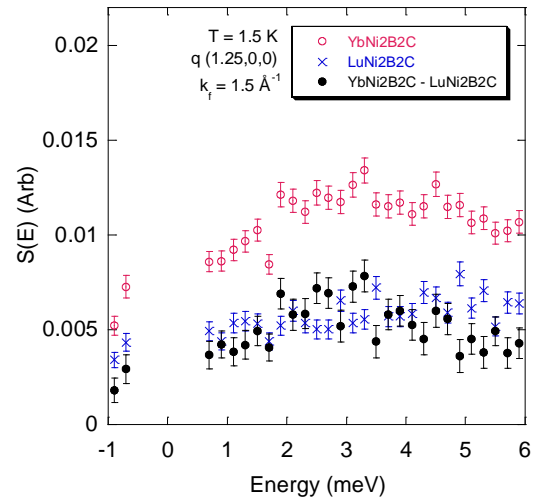
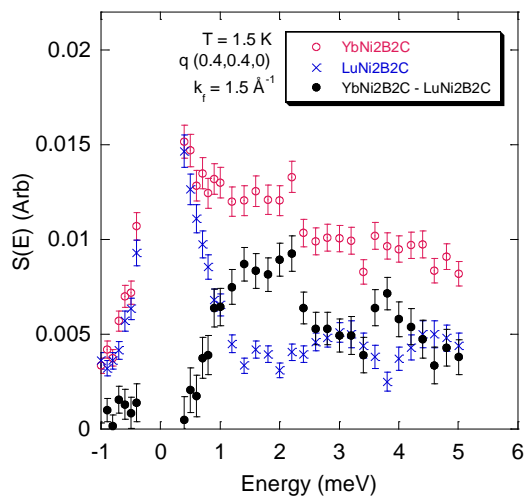
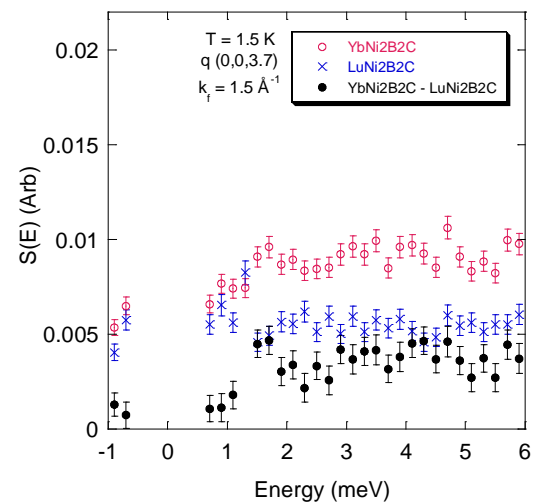


Fig 6.15 : Two thirds the $\text{YbNi}_2\text{B}_2^{11}\text{C}$ (1.9,0,0) energy scan added to one third of the (0.4,0,5.7) scan taken on IN20 superimposed on the H.E.T. data.

There is good agreement for the P1 and P3 scattering in the above figure. The P2 peak is more pronounced in the H.E.T. data, although it is certainly present in the data taken on IN20. Overall, the agreement provides evidence that the observed features are real and not from phonon or spurious scattering.

A description of the IN14 spectrometer and a list of the scans performed are given in § 6.3. The measurements performed on IN14 explored the low energy magnetic scattering in $\text{YbNi}_2\text{B}_2^{11}\text{C}$ in more detail. Figures 6.16 to 6.19 show energy scans performed, at a temperature of 5 K, at different positions in q with a final neutron wavevector of 1.5 \AA^{-1} .

Fig 6.16 : q (0.55,0,0)Fig 6.17 : q (1.25,0,0)Fig 6.18 : q (0.4,0,4.0)Fig 6.19 : q (0,0,3.7)

Figs 6.16 to 6.19 : Energy scans of $\text{YbNi}_2\text{B}_2^{11}\text{C}$ and $\text{LuNi}_2\text{B}_2^{11}\text{C}$ taken on IN14 at different positions in q . All data taken at a temperature of 1.5 K.

Figure 6.16 shows an energy scan performed at a q position of (0.55,0,0). The P1 peak seen in the H.E.T. and IN20 data is clearly visible in the subtracted data. This feature also appears in the others scans taken at q positions in the ab plane (figures 6.17 and 6.18). The position of the centre of this peak, at ~ 3 meV, corresponds very well to the

position of P1 determined in the fit to the H.E.T. data. The height of the peak maximum at the three q positions in the ab plane scales very well with the square of the ytterbium form factor. This suggests that the P1 scattering is isotropic in the ab plane. The P1 scattering is also visible in the scan taken at a q position of $(0,0,3.7)$. However, the magnitude of q at this position is similar to that at $(1.25,0,0)$, but the peak maximum is less by a factor of $\sim 2/3$.

Figures 6.20 and 6.21 show the IN14 data from figures 6.17 and 6.19 with two IN20 energy scans taken at a similar q superimposed. The IN20 data was measured with a final neutron wavevector of 2.66 \AA^{-1} .

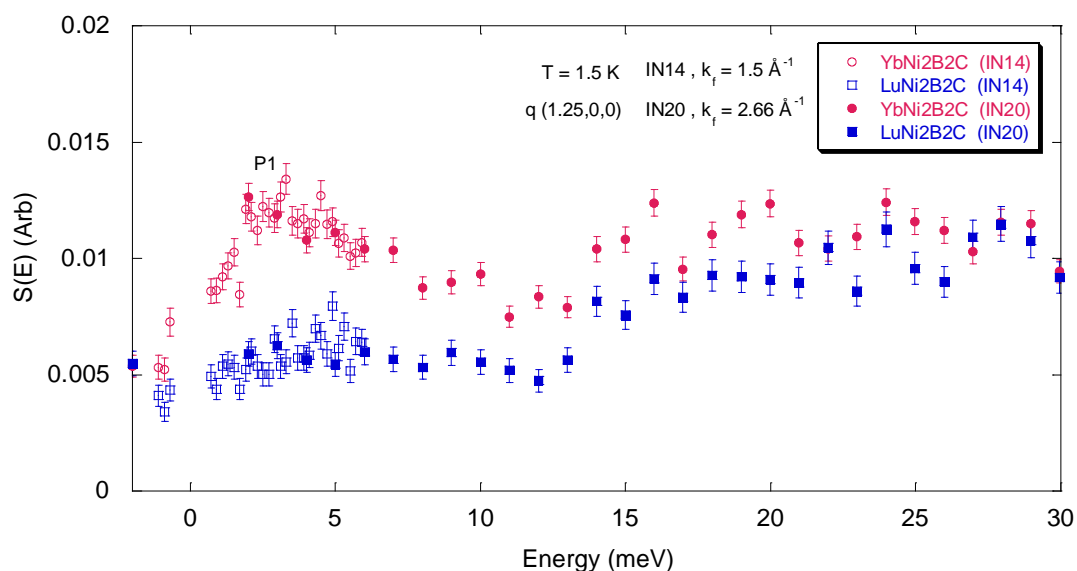


Fig 6.20 : Energy of $\text{YbNi}_2\text{B}_2^{11}\text{C}$ and $\text{LuNi}_2\text{B}_2^{11}\text{C}$ scans taken on IN14 and IN20 at a q position of $(1.25,0,0)$. The IN14 (IN20) data was taken with a final neutron wavevector of 1.5 (2.66) \AA^{-1} . All data taken at a temperature of 1.5 K.

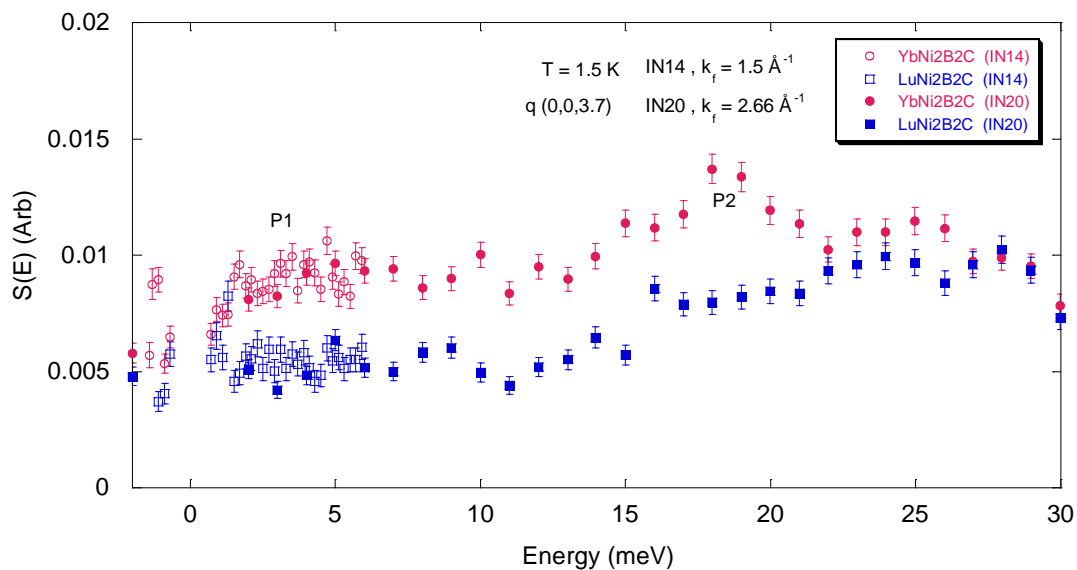


Fig 6.21 : Energy scans of $\text{YbNi}_2\text{B}_2^{11}\text{C}$ and $\text{LuNi}_2\text{B}_2^{11}\text{C}$ taken on IN14 and IN20 at a q position of $(0,0,3.7)$. The IN14 (IN20) data was taken with a final neutron wavevector of 1.5 (2.66) \AA^{-1} . All data taken at a temperature of 1.5 K.

Figure 6.20 again shows evidence for the P1 scattering in both the IN14 and the IN20 data. There is no evidence of the P2 peak in this figure. The magnitude of the P1 scattering is reduced in figure 6.21. There is some evidence of the presence of the P2 peak in this scan although it is not as clear as it is in the IN20 data taken with a final neutron wavevector of 4.1 meV or the H.E.T. data. Therefore, the data presented in the above two figures agrees broadly with the selection rules for the CP1 and the CP2 peaks.

In all the IN14 scans presented above, there is no evidence of the low energy peak, centred at ~ 0.34 meV, reported by C. Sierks *et al.* (see § 6.7). Figures 6.22 and 6.23 show q scans along the $[100]$ direction at an energy of 0.5 meV with a final neutron wavevector of 1.4 \AA^{-1} , and along the $[110]$ direction at an energy of 0.6 meV with a final neutron wavevector of 1.5 \AA^{-1} respectively. It could be that the low energy peak, should it exist, is localised in its position in q , and these scans were performed to explore this possibility.

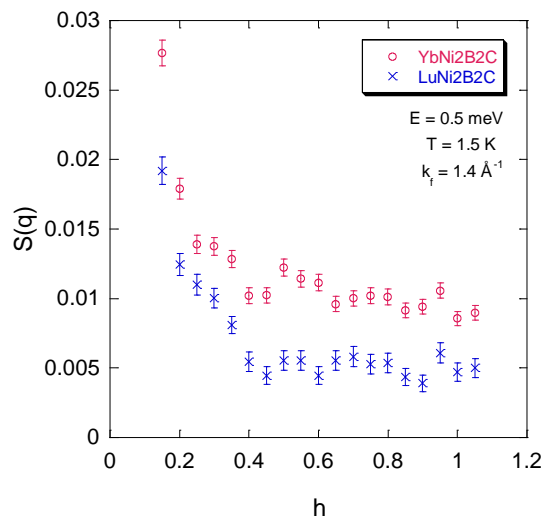


Fig 6.22 : E = 0.5 meV.

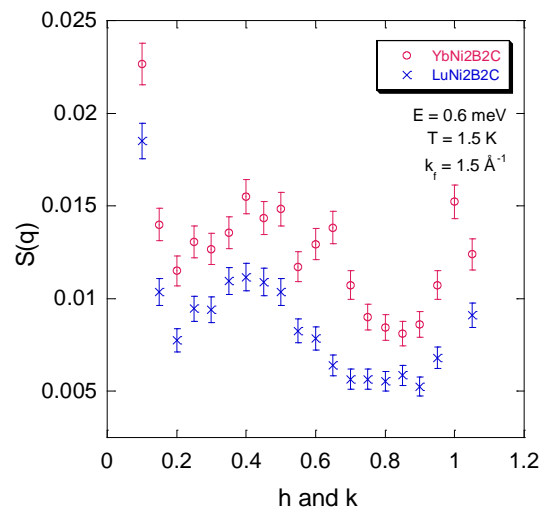


Fig 6.23 : E = 0.6 meV.

Two q scans of $\text{YbNi}_2\text{B}_2^{11}\text{C}$ and $\text{LuNi}_2\text{B}_2^{11}\text{C}$ measured using IN14 at a temperature of 1.5 K. Figure 6.22 extends from $(0.15,0,0)$ to $(1.05,0,0)$ and is measured at $E = 0.5$ meV using a final neutron wavevector of 1.4 \AA^{-1} . Figure 6.23 extends from $(0.1,0,1,0)$ to $(1.05,1.05,0)$ and is measured at $E = 0.6$ meV using a final neutron wavevector of 1.5 \AA^{-1} .

In both the above figures, the q dependent variation in the scattering from the $\text{YbNi}_2\text{B}_2^{11}\text{C}$ sample is qualitatively very similar to the variation of the scattering from the $\text{LuNi}_2\text{B}_2^{11}\text{C}$ non-magnetic blank sample. Therefore, there is no evidence of any q localised low energy magnetic scattering of the type seen by C. Sierks *et al.* in these scans.

Two further experiments were performed on IN5 and IN6 to search for signs of the low energy scattering mentioned above. As highlighted in the relevant experimental descriptions (IN5, § 6.4 and IN6, § 6.5), there were problems in the conduct of both these experiments (Yb_2O_3 contamination in the IN5 experiment, and large cryostat spurious and inadequate time in the IN6 experiment). However, some useful data was obtained.

Figure 6.24 demonstrates the problems caused by the Yb_2O_3 impurity phase in the IN5 experiment. It shows a $\text{YbNi}_2\text{B}_2^{11}\text{C}$ energy scan, taken at a temperature of 1.5 K,

using an incident neutron wavelength of 5 Å, with the $\text{LuNi}_2\text{B}_2^{11}\text{C}$ data subtracted. Superimposed on this figure is a Yb_2O_3 energy scan taken at the same temperature. The $\text{YbNi}_2\text{B}_2^{11}\text{C}$ data with both the $\text{LuNi}_2\text{B}_2^{11}\text{C}$ data and the Yb_2O_3 data subtracted is also shown.

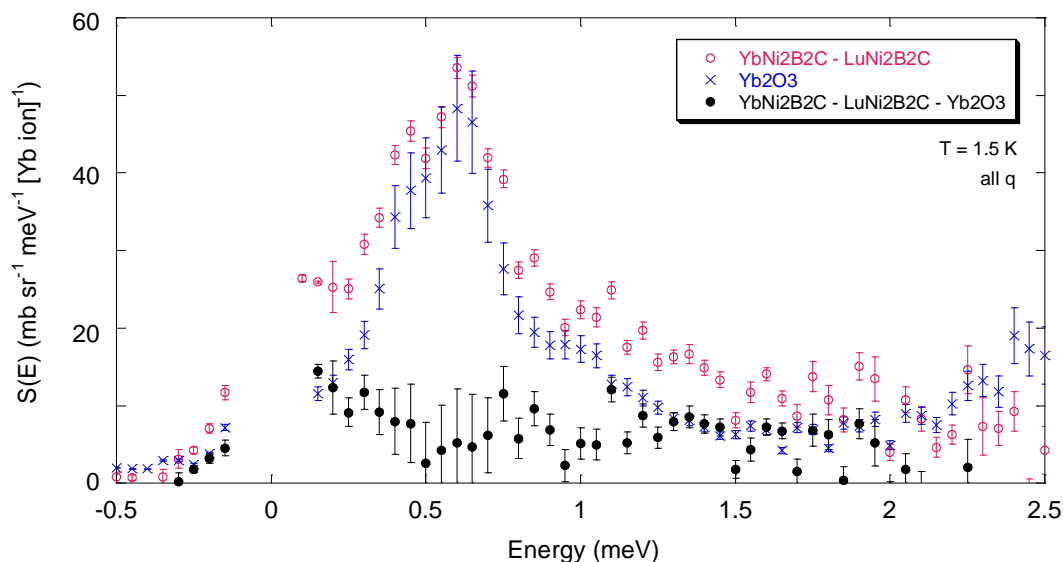


Fig 6.24 : Energy scan of $\text{YbNi}_2\text{B}_2^{11}\text{C}$ performed on IN5 at a temperature of 1.5 K with the non-magnetic and Yb_2O_3 impurity scattering subtracted. Initial neutron wavelength of 5 Å.

The antiferromagnetic ordering temperature of Yb_2O_3 is 2.7 K. Below this temperature, there will be low energy scattering due to magnon excitations. This scattering is clearly seen, centred at an energy of $\sim 0.6\text{meV}$, in both the Yb_2O_3 and the $\text{YbNi}_2\text{B}_2^{11}\text{C}$ magnetic scattering data of the above figure. Efforts to gain meaningful data by subtracting the Yb_2O_3 scan from the $\text{YbNi}_2\text{B}_2^{11}\text{C}$ scan proved very difficult due to the large relative size of this impurity scattering. The data shown in figure 6.24 is not reliable above $E \sim 1.5\text{meV}$ as this is the limit of the energy loss scattering that IN5 is capable of measuring with an initial neutron wavelength of 5 Å. Although the fully subtracted data is of bad quality, there does seem to be two components to the low energy scattering. There is a rise in scattering from 0.5 meV towards the elastic line. A gradual rise is also seen from 0.5 meV with increasing energy which is consistent with the P1 peak seen in all the data discussed so far. The overall

magnitude of the magnetic scattering from $\text{YbNi}_2\text{B}_2^{11}\text{C}$ measured in this experiment agrees well with an extrapolation of the higher energy data measured in the H.E.T. experiment.

A check on the above interpretations of the IN5 data was provided by the IN6 experiment using a single crystal sample with no impurity contamination. Figure 6.25 shows a subtraction of a $\text{YbNi}_2\text{B}_2^{11}\text{C}$ energy scan taken on IN6, at a temperature of 2 K, using an initial neutron wavelength of 4.1 \AA , from a $\text{YbNi}_2\text{B}_2^{11}\text{C}$ scan taken at 10 K. The neutron energy gain data is shown as the energy loss side of the energy scan was contaminated by cryostat spurion scattering. This particular method of background subtraction was performed as there was no time in this experiment to measure the non-magnetic $\text{LuNi}_2\text{B}_2^{11}\text{C}$ sample.

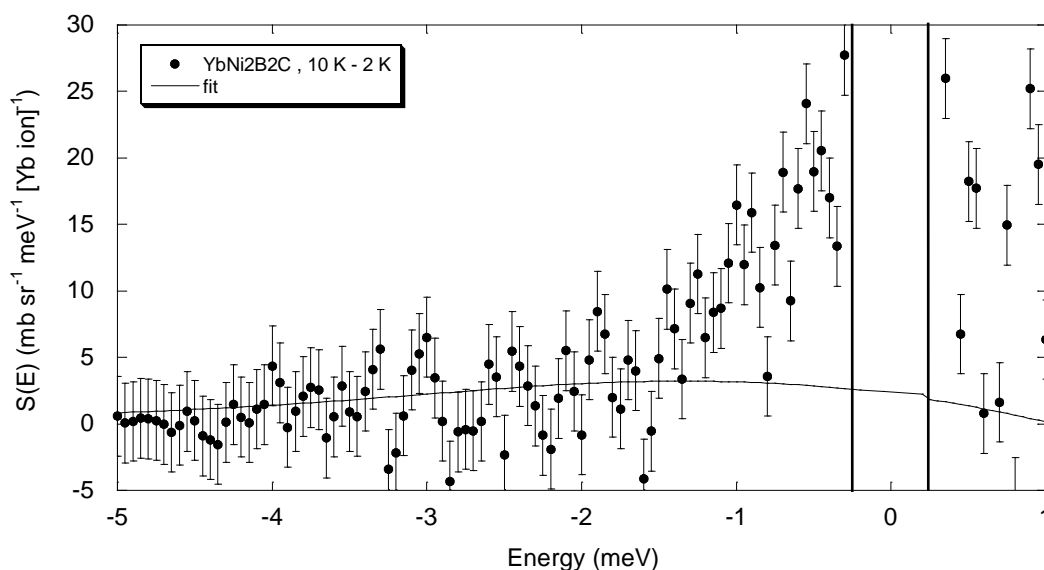


Fig 6.25 : Energy scan of $\text{YbNi}_2\text{B}_2^{11}\text{C}$ taken on IN6 at a temperature of 10 K. A similar scan of taken at a temperature of 2 K has been subtracted. The vertical lines indicate the region of elastic line contamination. Initial neutron wavelength of 5 \AA

The bold line shows the theoretical subtraction assuming the presence of just the P1 peak. There is some additional scattering close to the elastic line that is not described correctly with this theoretical curve. Perhaps this scattering is of the same origin as the

scattering below 0.5 meV in the IN5 data. The scattering in figure 6.25 extends to larger energy transfers than the IN5 data. This could be because the IN6 scan was performed at a higher temperature and the peak position and width have changed. As with the IN5 data, the data taken in this experiment is not conclusive. However, the same scattering has been seen in both experiments and this provides evidence that the very low energy signal is real.

The low energy scattering seen in the IN5 and the IN6 data could have the same physical origin as the ~0.34 meV scattering reported by C. Sierks *et al.* However, our IN5 data has significant differences to their published IN5 data:

In figure 6.7, the magnitude of the 0.34 meV scattering is substantially greater than the level of scattering at an energy transfer of 1.5 meV. The level of scattering at these two energies are closer in magnitude in the IN5 data obtained in this thesis. The data shown in figure 6.7 has a significant amount of scattering at an energy of 0.5 meV which is not present in the data in this thesis. It is obviously difficult to speculate as to the exact reasons for the differences mentioned above without access to the sample used by C. Sierks *et al.*, but several possibilities exist. Very pure polycrystalline samples of ytterbium compounds are difficult to produce for the reasons outlined in § 6.1.3.2. A 9% Yb₂O₃ impurity was present in the polycrystalline sample of YbNi₂B₂¹¹C used in this thesis. This amount of impurity had a huge effect on the observed scattering across the entire energy range studied. However, the impurity was difficult to detect for the reasons mentioned in § 6.1.3.2. Perhaps, the substantial scattering at 0.5 meV in figure 6.7 is because the sample used by C. Sierks *et al.* contained a small amount of Yb₂O₃. If their sample contained a percentage of contamination much smaller than the one affecting the sample used in this thesis, then it would have been extremely difficult to detect by laboratory based X-ray diffraction, but unless it was very small indeed, it would still have had a large effect on the observed scattering over the IN5 energy range that they studied. Also, to our knowledge, C. Sierks *et al.* did not measure a non-magnetic blank sample to enable an approximate phonon subtraction. The scattering observed from the LuNi₂B₂¹¹C sample on IN14 at several positions in q (e.g. figures 6.16 and 6.18) shows an increasing phonon contribution from ~2 meV moving towards the elastic line. This

behaviour was also seen in the IN5 $\text{LuNi}_2\text{B}_2^{11}\text{C}$ data. If this is not taken into account, one would be led to believe that the magnetic scattering from the $\text{YbNi}_2\text{B}_2^{11}\text{C}$ compound at low energies is much larger than it in fact is. This effect would be worse the lower the energy studied. This could be the reason C. Sierks *et al.* observed a very much larger amount of scattering close to the elastic line, at ~ 0.34 meV, than at an energy transfer of 1.5 meV. To test this hypothesis, the IN5 analysis was performed, but without removing the non-magnetic $\text{LuNi}_2\text{B}_2^{11}\text{C}$ scattering.

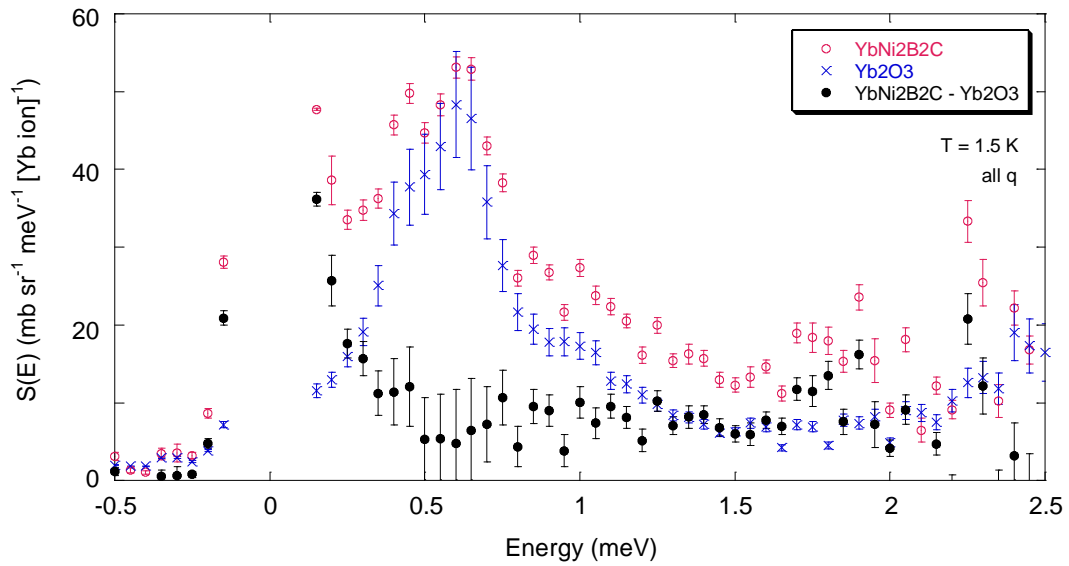


Fig 6.26 : Energy scan of $\text{YbNi}_2\text{B}_2^{11}\text{C}$ performed on IN5 at a temperature of 1.5 K with the Yb_2O_3 impurity scattering subtracted. The non-magnetic $\text{LuNi}_2\text{B}_2^{11}\text{C}$ scattering has not been subtracted.

The data presented in the above figure clearly has a larger amount of scattering close to the elastic line than figure 6.24 which has had the $\text{LuNi}_2\text{B}_2^{11}\text{C}$ scattering subtracted. The overall magnitude of the very low energy scattering is now much more consistent with the data obtained by C. Sierks *et al.*

In the following discussion and conclusion section, the low energy (< 0.5 meV) scattering seen in both the IN5 and IN6 experiments in this thesis will be referred to as P0. If the above reasoning concerning the C. Sierks *et al.* data is correct, it would explain why the P0 scattering was not seen in the IN14 experiment; at a temperature

of 1.5 K, the P0 peak does not extend above 0.5 meV, and the resolution of the energy scans performed on IN14 was too large to resolve scattering at this energy. Likewise, the q scans designed to search for the P0 scattering were performed at energies of 0.5 meV and 0.6 meV. They perhaps should have been performed at lower energies.

6.7 Discussion and conclusions.

In many ytterbium heavy electron compounds, the energy scales of the Yb/ conduction electron correlations and the C.E.F. interaction are similar. Therefore, the interpretation of magnetic inelastic neutron scattering experiments performed on these compounds can be controversial [8]. If the compounds also exhibit short or long range order of the Yb moments, or superconductivity, the difficulty in interpretation may be even more extreme.

The data presented in the previous section for $\text{YbNi}_2\text{B}_2^{11}\text{C}$ shows clear evidence of the C.E.F. transitions CP1, CP2 and CP3. In the data, these are denoted by P1, P2 and P3. The most conclusive evidence that these are C.E.F. transitions, or that they have a strong C.E.F. character, is that the q dependence of the IN20 (P1, P2 and P3) and IN14 (P1) data agree well with that predicted by theory. The magnitude of the P1 transition shows zero or fairly weak dispersion within the ab plane when corrected for the Yb form factor. This is evidence that the P1 scattering arises from a single site transition. The C.E.F. model predicts that the CP1 transition should only be visible when q has a component in the ab plane. The IN20 (figures 6.14 and 6.21) and IN14 (figure 6.19) data show that this transition is visible at a position in q of (0,0,3.7) although its magnitude is substantially reduced. Due to the difficulty in mounting the $\text{YbNi}_2\text{B}_2^{11}\text{C}$ and $\text{LuNi}_2\text{B}_2^{11}\text{C}$ single crystals in both the mosaic samples, there were large overall mosaic spreads of $\sim \pm 4^\circ$ and $\sim \pm 3.5^\circ$ respectively. This would mean that, although the spectrometer had been moved to collect neutrons scattered at a position in q with no ab component, some ab scattering may have been detected. Alternatively, perhaps the P1 peak could be observed at q positions with no ab component due to a ‘softening’ of the selection rules caused by heavy fermion correlations of the Yb +3 ion or some other coupling that would mean that the ground state is no longer described completely by the rare earth standard model.

The fact that reasonably strong C.E.F. transitions are observed in $\text{YbNi}_2\text{B}_2^{11}\text{C}$ implies that a good approximation of the state of the Yb +3 ion is provided by the rare earth standard model. This evidence is complimented by the fact that L_{III} edge X-ray absorption spectroscopy shows that the Yb ions are in a stable 3+ ionisation state [9]. However, the C.E.F. transitions are substantially broadened which indicates the presence of strong relaxation pathways (see § 2.2.5). The H.E.T. data indicates that the relative intensities of the P1, P2 and P3 peaks are broadly consistent with the C.E.F. model although they are all less by a factor of ~ 0.7 than predicted. This could be because of a reduction in the Yb moment due to spin compensation with the electrons of the surrounding ions. However, the problems associated with the Yb_2O_3 impurity subtraction in the H.E.T. experiment make an exact determination of the overall magnitude of the scattering from the $\text{YbNi}_2\text{B}_2^{11}\text{C}$ sample difficult. Perhaps the most striking difference between the data and the C.E.F. model is that the positions of P1, P2 and P3 are roughly a factor of two greater than the predicted values. This could be due to a movement in the positions of the ligands of the surrounding ions due to their hybridisation with the Yb 4f electrons. It could also be due to the coupling of the C.E.F. transitions to other excitations within the compound. At very low temperatures, the effects of detail balance make it extremely hard to distinguish between truly quasielastic and very low energy inelastic transitions. However, both the data obtained by C. Sierks *et al.* and the data collected in this thesis would suggest that P1 is a truly inelastic transition. This would imply that the doublet has been split or is now no longer the true ground state of the Yb ion. A splitting of the doublet can only be caused by a static exchange field at the Yb site [10]. However, no evidence of long range magnetic order has been observed in other types of experiment performed on $\text{YbNi}_2\text{B}_2^{11}\text{C}$. Another reason for the rejection of a low energy scattering model where the P1 peak exists as a unique quasielastic components concerns its width. The width of the P1 peak, at a HWHM of 3 meV, suggest a value for T_K that is too large when compared with the value of ~ 8 K obtained from the magnetic specific heat of $\text{YbNi}_2\text{B}_2^{11}\text{C}$ (see fig 1.2). This fact, and the observation of the very low energy peak by C. Sierks *et al.* was the motivation for the IN5 experiment and the search for the P0 peak in the IN14 experiment. The width of the peak mentioned by C. Sierks *et al.* is 0.33 meV. The width of the P0 peak in the IN5 data presented here is ~ 0.29 meV, although the quality of the IN5 data means that this is only an approximate value. This

agrees much better with the value for T_K determined from specific heat measurements.

As mentioned above, the inelastic nature of the P1 peak implies that the ground state degeneracy has been lifted, or that the doublet position has been moved to finite energies. As no signs of static magnetic order have been observed in $\text{YbNi}_2\text{B}_2^{11}\text{C}$, perhaps another mechanism can explain this observation.

In CeAl_2 , the C.E.F. transitions are substantially different from the rare earth standard model scheme [11]. Only one transition is predicted but two are observed in inelastic neutron scattering. The widths of the transitions are also substantially different to that proposed for the single transition by theory. In this compound, it is thought that there is a strong coupling between the lattice vibrations and the C.E.F. transitions. This ‘magneto-phonon’ coupling leads to a large modification of the entire inelastic response of the compound. Interestingly, the two peaks observed in CeAl_2 show negligible dispersion [12], as do the ‘C.E.F.’ peaks observed for $\text{YbNi}_2\text{B}_2^{11}\text{C}$ in this thesis. In CeAl_2 , the nuclear (high q) - phonon scattering was characterised and a low temperature softening was observed as the C.E.F./ lattice coupling was established [13]. The Yb monopnictides YbX ($X = \text{N}, \text{Sb}, \text{As}$ and P) also have anomalous C.E.F. excitation schemes [14]. The magnitude of the C.E.F. splittings in these compounds is also larger than those predicted by a simple point charge model. These compounds all order magnetically but at temperatures much lower than the RKKY exchange interactions would suggest. In YbN and YbSb , the experimental observation of more transitions than expected has been interpreted in terms of magneto-phonon coupling. These compounds have large phonon scattering coinciding with the positions of the magnetic peaks.

Perhaps a similar effect is responsible for the movement of the P1, P2 and P3 transitions in $\text{YbNi}_2\text{B}_2^{11}\text{C}$. If this was a correct interpretation, the P0 quasielastic peak, representing a local Yb/ conduction electron heavy fermion coupling, would constitute the ground state of the compound. The width of this peak would agree well with the position of the maximum in the magnetic specific heat. The three inelastic peaks P1, P2 and P3 would constitute excitations within the C.E.F. magneto-phonon

system. The position of P1, at ~ 3 meV, would explain why there is still a large contribution to the magnetic specific heat at temperatures (at ~ 30 K) above the Kondo peak position. The much larger widths of the P1, P2 and P3 transition, when compared to the P0 width, would also be less surprising due to the introduction of more complicated relaxation dynamics due to the coupling of the magnetic and lattice excitations. In support of this theory, strong phonon scattering was observed at similar energies to the P2 and P3 peaks in a high q IN20 energy scan performed in this thesis.

If the P1 peak is quasielastic, the P1, P2 and P3 excitations could be consistent with the standard C.E.F. model with a broadening of the P1 peak due to single site hybridisation of the Yb $4f$ and conduction electrons with a energy scale of ~ 3 meV. The P0 peak might then signify lower energy excitations, perhaps due to short range intersite Yb correlations with the correct energy to be responsible for the peak at ~ 8 K in the specific heat. If this was the case, this peak might have significant dispersion. Unfortunately, as the P0 peak was not observed in the IN14 experiment, its q dependence was not studied in this thesis. It should be noted, however, that no broad features were observed in the D10 experiment performed in this thesis which could have been interpreted as evidence of short range Yb-Yb correlations. This two component quasielastic excitation scheme has been proposed before, to explain the low energy inelastic response of CeRu_2Si_2 and CeCu_6 [15].

Further experimental and theoretical work is necessary to determine if either of the above excitation schemes is plausible for $\text{YbNi}_2\text{B}_2^{11}\text{C}$. Suggestions for this work will be given in the following chapter.

References

- [1] R.S. Eccleston and R. Osborn, *The HET Mini-Manual*, RAL-94-117 (1994).
- [2] U. Gasser *et al.*, *Z. Phys. B*, **101**, 345 (1996).
- [3] *The Yellow Book: Guide to Neutron Research Facilities at the I.L.L.*, I.L.L. Publication (1997).
- [4] B.K. Cho *et al.*, *Phys. Rev. B*, **52**, 3684 (1995).

-
- [5] C. Sierks *et al.*, *Physica B*, **259-261**, 592 (1999).
 - [6] A. Yatskat *et al.*, *Phys. Rev B*, **54**, 3772 (1996).
 - [7] *The L.A.M.P. Book*, I.L.L. Publication (2000).
 - [8] G. Polatsek and P. Bonville, *Z. Phys. B*, **88**, 189 (1992).
 - [9] S.K. Dhar. *et al.*, *Solid State Commun.* **98**, 985 (1996).
 - [10] ***Kramers doublet splitting ???***
 - [11] P. Thalmeier *et al.*, *Phys. Rev. Lett.*, **49**, 1588 (1982).
 - [12] P. Thalmeier, *J. Appl. Phys.*, **55**(6), 1916 (1984).
 - [13] P. Thalmeier. *J. Phys. C: Solid State Phys.*, **17**, 4153 (1984).
 - [14] M. Kohgi *et al.*, *Physica B*, **163**, 625 (1990).
 - [15] ***PhD thesis made in Grenoble, I think it was Jacquier (~1990/1995), and probably Rossat-Mignot was involved. ???***

CHAPTER 7

CONCLUSIONS AND SUGGESTIONS FOR FURTHER WORK

The magnetisation density experiment performed on $\text{YbNi}_2\text{B}_2^{11}\text{C}$ did not show any features that could be specifically identified with the formation of a heavy fermion state. Within the experimental resolution, there was no evidence of a magnetic moment on the Ni, B or C sites, above or below the Kondo temperature. No moment was observed on these sites in the $\text{ErNi}_2\text{B}_2^{11}\text{C}$, $\text{HoNi}_2\text{B}_2^{11}\text{C}$ and $\text{LuNi}_2\text{B}_2^{11}\text{C}$ compounds. The anisotropic magnetisation density on the Yb site did not change significantly on moving to temperatures below T_K . The anisotropy of the Yb density was qualitatively very similar to that on the Er site. As $\text{ErNi}_2\text{B}_2^{11}\text{C}$ is not a heavy fermion compound, this form of rare earth magnetisation density can not be linked with heavy fermion behaviour. Interestingly, the anisotropy of the Ho site was different to the Yb and Er sites. There are several possible explanations for these observations:

The features associated with the heavy fermion behaviour could be below the resolution of the experiment. The problems of multiple scattering in the $\text{YbNi}_2\text{B}_2^{11}\text{C}$ crystal make the measurements of very small magnetic moments difficult. The most important factor in causing the large amount of multiple scattering in the $\text{YbNi}_2\text{B}_2^{11}\text{C}$ crystal was the tight mosaic spread. In a future experiment, an effort should be made to obtain crystals with wider mosaic spreads. Before the advent of accurate models for correcting for extinction became available, single crystals were often subjected to thermal shock treatment in an attempt to increase their mosaic spreads and reduce their crystallite radii. Perhaps a similar process could be performed here, if the NiB^{11} flux technique was found to be incapable of growing crystals with wider mosaic spreads. The model used for correcting for extinction (see § 5.1.4.2) is most accurate for cubic crystals. Therefore, it would be sensible to use crystals with a more regular

shape instead of the ‘flat plate’ ones used in this thesis even if this meant that the overall sizes of the crystals were smaller. In a future experiment, it would be a good idea to make a greater effort to determine the exact multiple scattering correction to make in the D3 experiment. This could be done by measuring a set of Bragg intensities (instead of just the flipping ratios) as was done using the D9 diffractometer. This set of reflections could then be refined and plots such as that shown in fig. 5.5 could be produced. This would be preferable to determining the D3 correction from the D9 correction as was done in this thesis. It would also be a good idea to try using an applied magnetic field of ~ 10 T in the $\text{YbNi}_2\text{B}_2^{11}\text{C}$ D3 experiment as it has been shown that the heavy fermion state is not completely suppressed by such a field (γ is still two-thirds of its zero field value with a 10 T field) [1]. A field of this magnitude was not available on D3 when the first set of measurements in this thesis were performed. Alternatively, it could be that the effects of heavy electron behaviour are not visible in magnetisation density images. The modifications of the atomic electron shells could be too subtle or of an internal nature. In order to determine if this is the case, it would be useful to study the magnetisation density in other heavy fermion compounds; perhaps ones with higher γ values.

The inelastic experiments performed on $\text{YbNi}_2\text{B}_2^{11}\text{C}$ presented in this thesis were more successful than the magnetisation density experiments. All the data shown in chapter 6 would indicate the existence of a ‘C.E.F. like’ excitation scheme, consisting of three substantially broadened Lorentzians, situated at energies of 3, 17 and 43 meV. The selection rules for these transitions agree well with their theoretical predictions. However, the magnitudes of the 17 and 43 meV transitions are a factor of ~ 2 greater than predicted. Also, the simple C.E.F. model, assuming no Yb-Yb interactions or coupling of the C.E.F. transitions to other excitations, would imply that the 3 meV transition should be quasielastic and correspond to the ground state doublet of the Yb $+3$ ion. There is evidence in this thesis, and from other authors, that there is also a quasielastic component with a HWHM of ~ 0.33 meV which corresponds well to the published Kondo temperature for $\text{YbNi}_2\text{B}_2^{11}\text{C}$. A mechanism has been suggested to account for the differences between the calculated and measured excitation schemes based on a coupling of the C.E.F. and lattice excitations. A large amount of further

work is needed to verify the results presented in chapter 6 and explore the possibility of a C.E.F./ phonon coupling. One of the problems with the inelastic scattering experiments was the low sample masses that were used. In future experiments, it would be useful to have larger samples of both $\text{YbNi}_2\text{B}_2^{11}\text{C}$ and $\text{LuNi}_2\text{B}_2^{11}\text{C}$.

Inelastic

sum up results briefly

polarised neutron time with bigger xtals better alignment and holder

in14, tighter elastic line lower energy q scans.

mag field to pull p0 out

Explore temerature dependence of peaks.

theory should be done

measures phonons in material

this thing about q depence at 0.5, Ni spins perhaps ???

A similar experiment on $\text{YbNi}_2\text{B}_2^{11}\text{C}$ would provide useful information concerning the nature of the excitation scheme

[1] W.P. Beyermann, *Physica B*, **259-261**, 584 (1999).